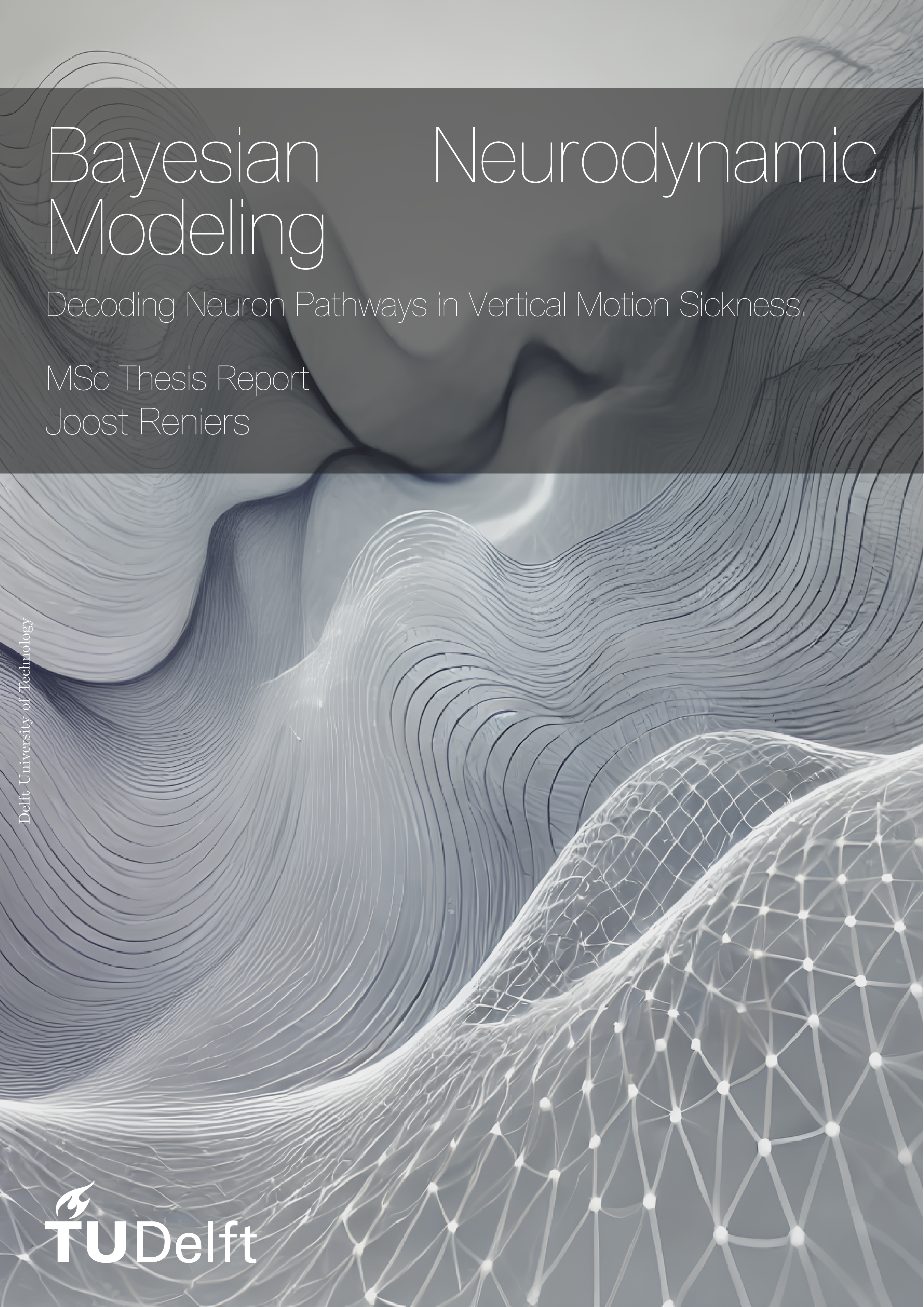

Bayesian Neurodynamic Modeling

Decoding Neuron Pathways in Vertical Motion Sickness.

MSc Thesis Report
Joost Reniers

Delft University of Technology

Bayesian Neurodynamic Modeling

Decoding Neuron Pathways in Vertical Motion Sickness.

by

Joost Reniers

to obtain the degree of Master of Science
at the Delft University of Technology.

Daily supervisor:	Tuğrul Irmak, Ph.D.
Supervisor:	Professor Riender Happee
Advisor:	Varun Kotian
Faculty:	Faculty of Mechanical, Maritime and Materials Engineering, Delft

Preface

Acknowledgements

I would like to thank everyone who supported me during the course of this research.

First, I extend my gratitude to my supervisor, Professor Riender Happee, for his guidance and insightful feedback.

I also thank Dr. Tugrul Irmak, my former daily supervisor, for his support at the beginning of this project and for inspiring its direction.

I would also like to extend my thanks to Varun Kotian, whose advice and suggestions significantly contributed to the refinement of my work.

Finally, I am thankful for the constant support from my family and my girlfriend. Their understanding and encouragement kept me going.

I could not have completed this thesis without the help of everyone mentioned, so thank you!

Joost Reniers

Abstract

The primary objective of this thesis is to develop a new model that accurately predicts vertical motion sickness by closely mirroring the neural dynamics and statistical properties of the otolith pathway. Unlike existing models, our approach incorporates elements such as noise, nonlinearities, and realistic sensory data, enhancing the accuracy and biological relevance of motion sickness predictions. This research aims to create a biologically plausible approach that derives a proxy metric for Motion Sickness Incidence (MSI). This metric will naturally emerge from sensory conflict, providing a more accurate prediction of vertical motion sickness and contributing to the development of systems designed to mitigate its effects. This has become increasingly critical with the growing prevalence of self-driving cars and virtual reality systems, where effectively addressing motion sickness is of great value.

To achieve this goal, we developed a novel model from the ground up, incorporating detailed dynamics and statistical properties of otolith hair cells and afferents in the inner ear. Three spiking models were developed based on Leaky-Integrate-and-Fire, Hodgkin-Huxley, and Generalized Linear Model frameworks. Each model presents unique advantages in capturing neural behavior. Our findings indicate that while all models offer valuable insights, the Leaky-Integrate-and-Fire model most effectively captures the dynamics, statistics, and temporal characteristics of otolith afferents.

The spiking models were used in a scheme that improves upon existing models in three ways. Firstly, and most fundamentally, we added noise and probability elements to our modeling. This makes the models more realistic by reflecting the natural randomness and variations in human behavior and perception. By more closely mimicking real-world conditions, our models better represent how humans perceive and respond to stimuli, making the simulations more accurate overall.

Additionally, we incorporate nonlinearities to accurately represent sensory saturation and have implemented a realistic organ definition, including hair cell tuning. The model relies on actual sensory data rather than simply aligning with subjective experimental results, allowing for a more accurate and biologically relevant simulation of sensory processing.

Lastly, the spiking models are integrated within a framework that utilizes Bayesian inference to estimate vertical acceleration, taking into account the inherent noise in the brain and aligning with modern neuroscience theories. By bridging the Free Energy Principle with the Sensory Conflict Theory, our model provides a more robust framework for understanding and predicting motion sickness.

The model gives results that are representative in terms of human motion perception sensitivity, while also being in line with current knowledge about frequency and amplitude dependence of Motion Sickness Incidence.

The resulting model gives us insights into how otolith dynamics influence motion sickness and is a proposal on how the brain resolves estimating vertical motion perception. Using different model configurations we were able to create a model that estimates motion accurately and propose a proxy metric for motion sickness incidence. This model is created in a modular way and can be extended on the basis of new objectives or new research findings. Additionally, with further enhancements, it holds potential applications in validating otolith theories on statistics and information transmission characteristics and even in the development of prostheses.

Contents

1

Introduction

Motion sickness is a pervasive and debilitating condition experienced by many individuals across a variety of environments, including land, air, sea, and virtual reality settings. It is characterized by a range of unpleasant symptoms, such as nausea, dizziness, and fatigue, which can severely impact an individual's well-being and performance [41]. Despite its widespread occurrence, the precise mechanisms underlying motion sickness are complex and are not fully understood. Consequently, predicting the onset and severity of motion sickness in response to specific motion stimuli remains a challenging but critical area of research.

The growing prevalence of technologies, such as virtual reality (VR) and self-driving cars, has heightened the importance of understanding and mitigating motion sickness. As these technologies become more prevalent the need to predict and prevent motion sickness becomes increasingly urgent. This is especially true in fields where prolonged exposure to motion stimuli is common, such as in aviation, maritime operations, and space exploration, where motion sickness can compromise safety and operational efficiency.

The dominant theory currently, is that motion sickness arises from a sensory conflict between the visual, vestibular, and proprioceptive systems [73]. When the brain receives mismatched sensory information about the body's position and movement, it triggers the symptoms associated with motion sickness. This conflict theory, while broadly accepted, does not fully account for the variability in individual susceptibility to motion sickness. Factors such as genetic predisposition, prior experiences, and even psychological state play a significant role, making the prediction of motion sickness a multi-faceted problem.

In recent years, advances in brain measurements and computational modeling have provided new ways to understand and predict motion sickness. By analyzing patterns in motion stimuli - such as acceleration, frequency, and duration - it is possible to develop predictive models that can anticipate the onset and severity of motion sickness. These models can help to minimize the risk of motion sickness.

Neural modeling plays a pivotal role in this research. Understanding how different types of vestibular neurons, such as otolith afferents, respond to motion stimuli allows for more accurate predictions of motion sickness. The complex anatomical differentiation of these afferents and their varied physiological responses to motion stimuli provide critical data for refining predictive models. By integrating these neural responses into computational frameworks, we can better understand the underlying mechanisms of motion sickness and develop more effective interventions.

This thesis explores the relationship between motion stimuli and motion sickness, with the goal of developing a predictive model that can accurately forecast the likelihood of experiencing motion sickness based on specific motion characteristics.

In this thesis we will not explore further the current state of research on motion perception and motion sickness, we refer the reader to my comprehensive literature review. In that document, we delve into the foundational theories and recent advancements in our understanding of these phenomena. This includes an examination of the sensory conflict theory, which remains the dominant explanation for motion sickness, as well as the latest insights into how individual variability in motion perception influences susceptibility to motion sickness. The literature review also covers the role of modeling in predicting motion sickness, highlighting how different models approach predict motion perception and motion sickness. By building this thesis on the existing body of knowledge, we aim to expand on previous findings and address gaps in current research.

The structure of this thesis is as follows:
Chapter 2 will summarise the current motion sickness models and their limitations.
Chapter 3 will outlay our objective, the approach and the reasoning behind it.
Chapter 4 will go into the characteristics of the spiking of otolith afferents.
Chapter 5 will explain the spiking models that are used to model these afferents.
Chapter 6 describes the Bayesian inference implementation to capture motion perception and predict motion sickness.
Chapter 7 presents the results of the predictive models and their validation across different motion environments.
Finally, Chapter 8 discusses explanations for the results, possible improvements to the model and directions for future research.

2

Motion Perception and Sickness Models

In this chapter, we explore various self-motion perception models and their ability to predict motion sickness. We begin with a brief overview of the models, including specific examples such as the Subjective Vertical Conflict (SVC) model, the Multisensory Observer Model (MSOM), and Lauren's Particle Filter.

2.1. Perception and Sickness Models

The SVC model, developed by Bos and Bles[7], is designed to explain motion sickness through the concept of a conflict between the subjective vertical, how the brain perceives gravity, and the actual gravitational vertical. The model is particularly effective in scenarios where there is a rotational movement or low-frequency oscillations, as it captures the motion sickness response by relying on simplified assumptions about otolith dynamics and low-pass filtering. However, its limitation lies in its accuracy, especially in cases involving pure vertical motion or complex multi-sensory conflicts. Despite its strengths, the SVC model is not well-suited for predicting motion sickness in scenarios involving pure vertical motion.

The MSOM[71], on the other hand, is a more sophisticated model that integrates multiple sensory inputs, such as visual, vestibular, and proprioceptive information, to predict motion perception. Based on the optimal observer theory, MSOM models the brain as an optimal estimator that minimizes sensory conflicts. While it excels in predicting motion perception across a variety of conditions, it struggles to predict motion sickness, particularly in scenarios involving pure vertical motion stimuli.

Lauren's Particle Filter model[59] is another approach to modeling self-motion perception, characterized by its use of distributed, parallel computations that resemble neural processing in the brain. This model provides a critical link for understanding the gap between behavior and distributed neural computation, offering valuable insights into the dynamic processing in the brain. It implements similar dynamics as the MSOM. However, the particle filter approach, while powerful, may face challenges in real-time application and in modeling complex motion scenarios. More critically, the model lacks the necessary mechanisms to handle conflicts arising in the vertical direction, making it unsuitable for predicting motion sickness.

These models, though varied in their approaches, each contribute to our understanding of motion perception and motion sickness. However, they all have their limitations, especially when it comes to generalizing across different contexts or accurately predicting motion sickness in specific scenarios like pure vertical motion. Further research and model refinement are needed to address these gaps and enhance the predictive capabilities of these models.

Kotian[56] researched various sensory integration models to predict motion perception and motion sickness. The authors focus on two primary models: the Multi-Sensory Observer Model (MSOM) and the Subjective Vertical Conflict models (SVC_{I} and SVC_{NI}). These models are evaluated against experimental data to determine their effectiveness in accurately predicting motion perception and motion sickness, particularly in response to vertical motion stimuli.

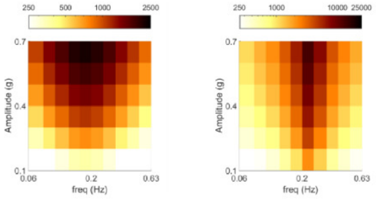

(a) SVC_I model

(c) SVC_{NI} model

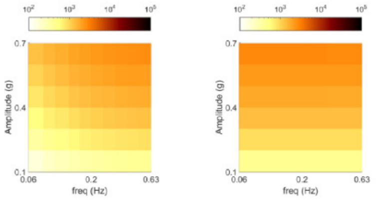

(b) MSOM (horizontal)

(d) MSOM (vertical)

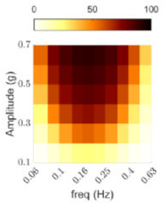

(e) Experimental vertical MSI(%) (McCauley et al, 1976)

Figure 2.1: Vertical Motion Sickness Incidence (MSI) as function of frequency and amplitude of vertical sinusoidal accelerations, figure from [56].

The MSOM, which has been widely used for predicting motion perception, shows effectiveness across different paradigms, but it falls short when it comes to predicting motion sickness. One of the main limitations of the MSOM is its inability to accurately capture frequency sensitivity, especially in the context of vertical accelerations. The model relies heavily on an otolith conflict term to represent vestibular input, but this approach fails to account for the unique frequency sensitivities associated with vertical motion. Consequently, the MSOM does not predict motion sickness effectively when vertical motion is involved, leading to significant discrepancies between the model's predictions and experimental observations.

On the other hand, the $\mathrm{SVC_I}$and $\mathrm{SVC_{NI}}$ models are specifically designed to account for conflicts between vestibular and visual inputs, which are critical in the development of motion sickness. The $\mathrm{SVC_I}$model, in particular, accurately reflects motion sickness responses to vertical accelerations, showing a peak in conflict at around 0.16 Hz, which is consistent with experimental data. However, these models are not without their limitations. The $\mathrm{SVC_I}$model, for example, struggles to predict roll-tilt perception in centrifugation scenarios, a type of motion where the subject experiences rotational movement while being translated along an off-vertical axis. The $\mathrm{SVC_{NI}}$ model, while slightly better in some perception tests, does not generalize well across all motion sickness scenarios, especially when visual inputs are introduced.

Despite the $\mathrm{SVC_I}$and $\mathrm{SVC_{NI}}$ models performing better than the MSOM in vertical motion scenarios, they still fall short in capturing the full complexity of vertical motion perception, particularly when visual cues or non-vertical rotational movements are involved. The paper highlights that current models, including MSOM and the $\mathrm{SVC_I}/\mathrm{SVC_{NI}}$, lack the necessary robustness to fully predict motion sickness in real-world scenarios where vertical motion plays a significant role.

The limitations observed in these models, especially with respect to vertical motion, suggest the need for a more comprehensive approach. A unified model that integrates the strengths of both the MSOM and $\mathrm{SVC_I}/\mathrm{SVC_{NI}}$ could potentially provide a more accurate prediction of motion sickness, particularly in scenarios involving vertical accelerations. Such a model would need to account for the unique frequency sensitivities of vertical motion, as well as the complex interactions between vestibular and visual inputs. Furthermore, the paper underscores the importance of further experimental validation, especially in contexts involving vertical motion, to refine these models and enhance their predictive accuracy.

In conclusion, while the $\mathrm{SVC_I}$and $\mathrm{SVC_{NI}}$ models offer improvements over the MSOM for predicting motion sickness in vertical motion contexts, there remains a significant gap in accurately modeling these phenomena. Addressing these gaps will require the development of a more sophisticated model that can handle the complexities of vertical motion perception and the onset of motion sickness.

2.2. Previous work based on existing models

In earlier work, the author of this thesis implemented both the Subjective Vertical Conflict (SVC) model and the Multisensory Observer Model (MSOM), validating them against the original studies by Bos et al.[7] and Newman et al.[71]. Among these models, the MSOM showed the most promise in replicating motion perception data, accurately reflecting how humans perceive motion under various conditions. However, the MSOM fell short when it came to aligning with observed motion sickness data. To address these limitations, the development of a distributed and probabilistic observer model was proposed. This new probabilistic version of the MSOM was successfully implemented and showed improved capabilities in accounting for changes in gravity. Despite these advancements, the model still struggled to explain frequency-dependent motion sickness phenomena, especially in the vertical direction. Given the current lack of a well-founded explanation for motion sickness induced by pure vertical motion, this research shifted focus towards developing a model specifically aimed at predicting vertical motion sickness.

3

Problem Statement, Objective & Approach

3.1. Problem statement

The MSOM and SVC model fall short in accurately predicting motion sickness during pure vertical motion stimuli [56].

The Subjective Vertical Conflict (SVC) model incorporates the otolith organs' dynamics using a unity gain function, meaning that the output is directly proportional to the input, without amplification or attenuation. Additionally, the model employs a low-pass filter to simulate how the signal from otoliths is processed further. This simplification, while effective in certain scenarios, may not fully capture the complexity of otolith dynamics, especially in situations involving pure vertical motion or stimuli with differing frequency characteristics. Consequently, the model may struggle to accurately predict motion sickness in such conditions. MSOM does not overly simplify the otolith dynamics with a unity gain function. Instead, it considers the otoliths' contributions within a complex, multisensory context, allowing for more accurate predictions of motion perception in scenarios involving complex or multisensory inputs. However, MSOM has limitations in predicting motion sickness, especially in pure vertical motion scenarios, where the model's integration of multiple sensory inputs may not fully account for the specific dynamics of the otolith organs.

Both models seem to lack robust scientific validation, particularly when it comes to addressing vertical motion, which is a critical aspect that should be more thoroughly explored. The goal of this thesis is to enhance the accuracy and applicability of motion sickness prediction and self-motion perception models.

3.2. Scope: Vertical motion

This research focuses on pure vertical motion and the processing of otolith signals to better understand the mechanisms behind vertical motion sickness. Due to the nature of sensory conflict theory, vertical motion sickness can be predicted by simulating otoliths only. The semicircular canals are not designed to provide sensory information on pure vertical motion, so the brain does not use this data for inferring vertical motion. Therefore, no conflict arises from the semicircular canals during vertical motion. Instead, the conflict originates within the otolith apparatus, which means we can focus on these organs only.

Current models try to match behavioral experiments, while the actual neuron spiking data is not always taken into account. In order to gain more insight into the mechanisms of self-motion perception and motion sickness in the otolith specifically, we should try to increase the resolution to the neuronal level. By analyzing neuronal spiking patterns, we can better understand how motion signals are processed and integrated within the brain, potentially leading to more accurate models and predictions.

The traditional view of the otolith organs as uniform structures primarily signaling the direction of gravity or low-frequency linear acceleration is now recognized as inadequate [20]. Research shows that there is a complex anatomical diversification of receptors and afferents within each otolith organ. This anatomical diversity is mirrored by the afferents' varied physiological responses, with some neurons signaling sustained aspects of stimuli, while others focus on transient changes. This is not reflected in any of the perception or sickness models today.

When measuring neural activity, we observe significant levels of stochasticity and noise. This randomness arises from the fundamental properties of ion channels and synaptic transmission, where thermal noise and probabilistic opening and closing of channels play a key role [23]. The nervous system effectively harnesses this stochasticity using distributed networks to reduce variance and verify sensory information. These networks enable the brain to make accurate inferences despite inherent noise, ensuring reliable processing of motion signals, and, as hypothesized, minimizing conflicts that could lead to motion sickness. Since it is such a fundamental part of the brain's workings, inherent randomness should be taken into account when modeling self-motion perception and motion sickness.

The distributed nature of the brain is closely related to the function of hair cells in the vestibular system. Hair cells are specialized to respond to different frequency ranges and 3D directions of motion [48], providing a broad spectrum of sensory inputs. A distributed approach is needed to capture the 3D workings of the brain's motion inference. This also relates to non-linearity and saturation where neurons with opposite directional sensitivity will provide complimentary information.

3.3. Objective

By modeling the perception of vertical acceleration to closely mirror the neural dynamics and statistical properties of the otolith pathway, we aim to derive a proxy metric for Motion Sickness Incidence (MSI). This metric is expected to naturally emerge from the resulting sensory conflict, providing a more accurate and biologically plausible prediction of vertical motion sickness.

3.4. Approach

In this thesis we will explore three different methods to describe the signaling in the neural system. One method is firing rate coding, which represents information as the average number of spikes per unit of time, offering a general measure of neuronal activity. This approach results in signals with the dimension "spikes per second" but these signals do not contain noise and will lead to computationally efficient models. Another method is temporal coding, which focuses on the precise timing of individual spikes to carry information about the stimulus and includes noise. In addition, population coding considers the activity of groups of neurons, where the pattern and combination of spikes throughout the population convey complex information. Temporal coding and population coding lead to more complex models with higher computational demand.

We propose a novel approach to modeling vertical motion perception by adopting a distributed processing framework that leverages actual measured neuronal firing data as a reference. By integrating this data into a Bayesian inference model, we aim to develop a more accurate prediction system for motion sickness incidence that accounts for both frequency and amplitude of motion stimuli. This method not only provides a more realistic simulation of the underlying physiological processes but also enables a finer-grained analysis of how different motion characteristics influence the onset and severity of motion sickness.

An implementation involving otolith signals holds promise for improving our understanding and prediction of motion sickness, particularly in vertical motion scenarios where existing models fall short. Otolith afferents, which include both regular and irregular neurons, exhibit distinct frequency ranges where they excel in discriminating motion. Regular neurons are more effective at higher frequencies, while irregular neurons become more discriminating around lower frequencies, particularly below 0.1 Hz [48][20]. This crossover at 0.1 Hz is critical, as it marks the point where irregular neurons surpass regular neurons in their sensitivity to motion. This is particularly relevant since low-frequency motion, such as vertical oscillations, currently lacks a robust explanation for its high incidence of motion sickness. Despite their inherent limitations, regular otolith neurons have been shown to perform slightly better than chance in discrimination tasks below 0.1 Hz, as demonstrated by Jamali et al. [48] in Figure 4.10. In contrast, irregular afferents exhibit superior performance above 0.1 Hz. This distinction suggests that incorporating otolith dynamics, particularly the complementary roles of regular and irregular afferents, could significantly enhance our models and offer a more comprehensive explanation for motion sickness, especially in low-frequency environments.

The results that emerge from our model should resemble the experimental results from O'Hanlon and McCauley [49], see Figure 2.1e. The results indicated that motion sickness incidence increases with certain combinations of frequency and acceleration, particularly highlighting a peak incidence at specific low-range frequencies and higher acceleration levels.

3.5. Method outline

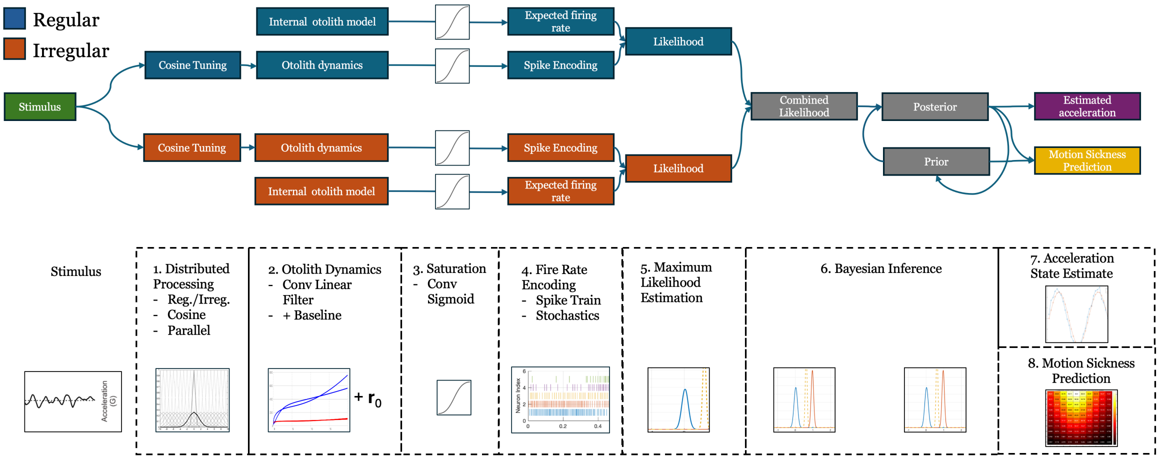

Figure 3.1: Otolith dynamics and spike encoding overview: The process begins with the introduction of a stimulus, which in this model represents vertical accelerations. Each hair cell in the vestibular system is tuned to a specific direction, requiring that the stimulus be defined according to the preferred direction of each hair cell. The stimulus is simultaneously presented to both regular (blue-coded) and irregular (red-coded) afferents. The distinct characteristics of regular and irregular otolith afferents are then applied to the stimulus, transforming the signal accordingly. This transformed signal is finally encoded into a spike train, reflecting the neural response of the afferents to the vertical acceleration.

This section outlines the methodologies used to achieve the research objectives, providing references to where each component of the process is detailed. We will explain the steps taken and highlight where specific information and data can be found throughout the thesis. A visual representation is shown in Figure 3.1.

Step 1 - Distributed Processing

Step 1 relates to the distributed nature of neurons in terms of directional sensitivity and being regular or irregular. We will simulate pools of neurons as described in chapter 6. However, first steps 2-4 will be described in chapter 4.

Step 2 - Frequency Dependency

Step 2 relates to the frequency-dependent characteristics of both regular and irregular afferents. The definition is based on research in chapter 5, but the implementation is done in chapter 4.

Step 3 - Saturation

Step 3 relates to the nonlinear behaviour of otolith afferents, where they saturate and thus become less responsive to additional increases in stimulus intensity. This is described in section 5.3.4.

Step 4 - Fire Rate Encoding

Step 4 relates to the encoding of the stochastic characteristics of the regular and irregular afferents. This is the major part of the model and is described throughout chapter 4.

Step 5 - Maximum Likelihood Estimation
Step 5 relates to the maximum likelihood estimation that is performed to predict the likelihood resulting from sensory data incoming from the otoliths and is described in section 6.3.1.

Step 6 - Bayesian Inference
Step 6 relates to the process of Bayesian inference, which combines a prior distribution with the sensory data to form a posterior distribution and is described in chapter 6.3.2.

Step 7 - Acceleration State Estimation
Step 7 involves estimating the acceleration by applying the Maximum A Posteriori (MAP) method to the posterior distribution and is described in section 6.3.3.

Step 8 - Motion Sickness Incidence Estimation
In this final step, the likelihoods obtained from the Bayesian inference model are used to estimate Motion Sickness Incidence (MSI). By analyzing the divergence between expected and observed sensory data, the model quantifies the probability of motion sickness occurring under specific motion conditions. This step provides a predictive metric that correlates directly with the likelihood of experiencing motion sickness, based on the physiological response of the modeled system.

4

Otolith Neuron Spiking Characteristics

4.1. Introduction

To create a model that resembles the mechanisms in the brain used for vertical motion perception, we have researched the characteristics of the otoliths and their neural pathway. In this chapter we will introduce the neural pathway and describe properties that are of importance when modelling it.

Neurons, the fundamental units of the brain and peripheral nervous system, are specialized cells responsible for transmitting information through electrical and chemical signals. Each neuron consists of a cell body (soma), dendrites, and an axon. The dendrites receive incoming signals, which are then processed in the soma, and transmitted along the axon to other neurons or target tissues via synapses. The process of transmitting signals involves changes in membrane potential, known as action potentials or spikes. These spikes are the carrier of neural information within the nervous system [13].

In the vestibular system, neurons play a crucial role in maintaining balance and spatial orientation by propagating and integrating information about head movements and gravitational forces. Vestibular neurons, located in the vestibular nuclei and the vestibular ganglion, process input from the inner ear's semicircular canals and otolith organs. This input is crucial for correct functioning of reflexive eye movements, posture control, and spatial navigation [31].

Understanding the spiking behavior of vestibular neurons is essential for developing accurate models that can predict their responses to various motion stimuli. Such models are instrumental in explaining the mechanisms of sensory processing and the integration of vestibular information with other sensory modalities. As computational neuroscience evolves and more data becomes available on the spiking of single neurons and populations of neurons, it becomes feasible to develop models that accurately represent brain behavior. This knowledge has important implications for developing treatments for balance disorders, motion sickness and improving vestibular prostheses.

Understanding how the brain infers motion and orientation is crucial for providing insights into motion sickness. Models focusing on these aspects have provided useful predictions that aid in anticipating motion sickness, though they are not yet comprehensive enough to explain all aspects of the phenomenon. This chapter focuses on the role of spiking in the brain, particularly within the otolith peripheral neural pathway. We will analyze otolith spiking data from Jamali et al. [48] to illustrate neural encoding strategies. It is important to note that the spiking data used throughout this thesis were obtained primarily from experiments conducted on macaque monkeys. Although their neural structures closely resemble those of humans[92], some differences in the precise values of observed variables may exist.

4.2. Otolith anatomy

Mammals have five vestibular sensory organs on each side of the head. The vestibular organs consist of three semicircular canals and two otolith organs (utricle and saccule). The semicircular canals detect rotational movements of the head through the movement of fluid within the canals, which stimulates hair cells. The otolith organs detect linear accelerations and head tilt relative to gravity by responding to the movement of tiny crystals, stimulating hair cells. Together, these organs provide critical information to the brain about head position and movement. Since we won't simulate rotational movements, we shall focus on the otoliths. However, there are parallels to be drawn between the neural processing of the semicircular canals and the otoliths.

Another important consideration is that the otoliths detect both linear accelerations and head tilts, which can create ambiguity in sensory perception. This occurs because the same sensory signals can be generated by different types of physical movements, making it challenging for the brain to distinguish between them accurately. However, this specific ambiguity is beyond the scope of our model and will not be further addressed in this work.

4.2.1. Otolith organs: Saccule & Utricule

To understand the role of the otolith organs in vestibular function, it is important to first examine their anatomy and how they contribute to balance and spatial orientation. This section will focus on the structure and function of the otolith organs, particularly in the context of linear acceleration, which are central to our simulation.

The otolith organs consist of two main structures: the saccule and the utricle. These organs are integral in detecting linear accelerations and head tilts, thereby contributing to our sense of balance and spatial orientation. The saccule is primarily responsible for sensing vertical movements, such as when moving up or down in an elevator, while the utricle is more sensitive to horizontal accelerations, like those experienced when accelerating in a car or during side-to-side head movements.

Both the saccule and utricle contain hair cells embedded in a gelatinous layer, which is topped with tiny calcium carbonate crystals known as otoconia. When the head moves, the inertia of the otoconia causes them to shift, which in turn bends the hair cells. This bending generates nerve impulses that are transmitted to the brain via the otolith afferents.

The otolith afferents are the nerve fibers that carry the signals generated by the bending of the hair cells in the saccule and utricle to the brain. The signals from the otolith afferents are transmitted to the vestibular nuclei in the brainstem.

From the vestibular nuclei, the information is processed and relayed to various parts of the brain, including the cerebellum, which plays a key role in coordinating balance and posture, and the cerebral cortex, where conscious perception of spatial orientation occurs. Additionally, these signals are sent to the oculomotor nuclei to help stabilize vision during head movements through the vestibulo-ocular reflex (VOR).

The integration of these signals ensures that the body can maintain equilibrium, adjust posture, and perceive motion accurately. This complex processing allows individuals to perform everyday activities smoothly, such as walking, running, or simply standing still, without losing balance. Any disruption in the function of the otolith afferents can lead to significant balance disorders, vertigo, and impaired spatial orientation, highlighting their critical role in maintaining vestibular function.

The otolith's structure from the inner ear to the axon can be seen in Figure 4.1. This figure can be used throughout this section as a reference.

4.2.2. Hair cells

Hair cells in the vestibular system are sensory receptors located within the inner ear. These cells have hair-like structures called stereocilia on their surface. When the head moves, the stereocilia bend, causing the ion channels to open and generate an electrical signal. This signal is then transmitted to vestibular neurons, which relay the information to the brain for processing and integration [40, 21].

There are two types of hair cells in the vestibular system. Type 1 hair cells in the saccule feature flask-shaped bodies and a large afferent nerve ending that forms a calyx structure around the cell body,

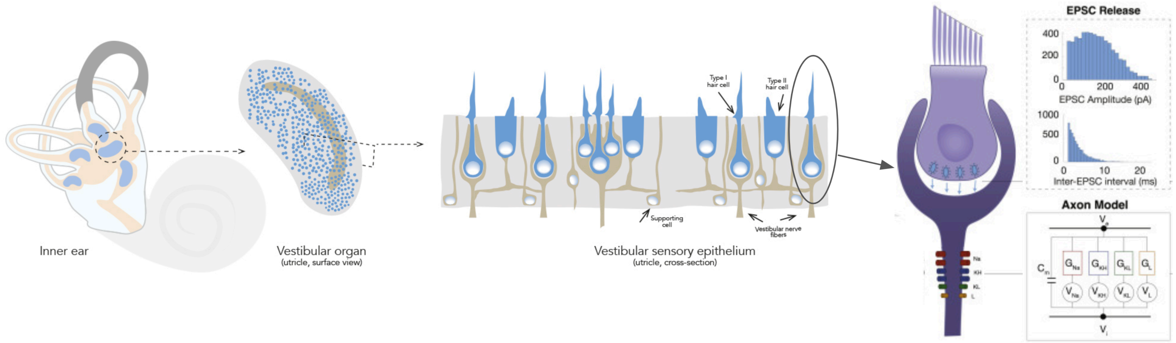

Figure 4.1: Overview of the otolith neuron structure, composition from 'Research Features' and [89].

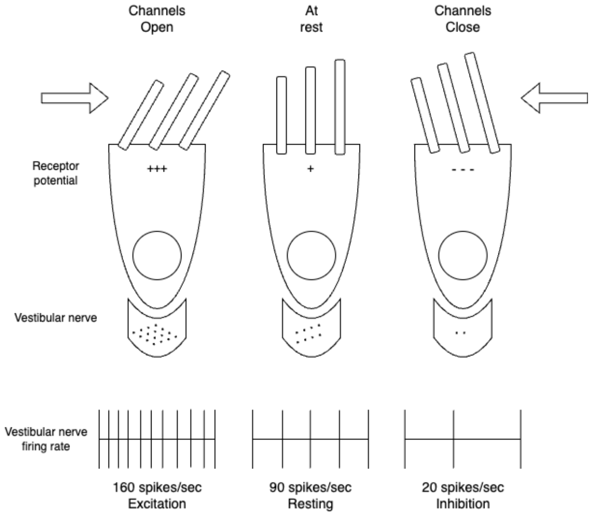

Figure 4.2: Relation between the stereo-cilia bending and neural firing rate. Replicated from [1]

providing a large synaptic area for rapid neurotransmission. This specialized synaptic organization allows type 1 cells to encode high-frequency stimuli. The calyx synapse, unique to Type 1 cells, is adapted for high rates of neurotransmitter release, crucial for the fast transmission of vestibular information. This hair cell is mostly associated with axons with an irregular firing pattern.

In contrast, type 2 hair cells have cylindrical shapes and multiple bouton-type synaptic connections with afferent fibers. These cells are more diffusely innervated compared to type 1 cells, with several smaller afferent terminals forming synapses along the surface of the cell. This hair cell is mostly associated with axons with an regular firing pattern and are believed to be involved in encoding lower frequency stimuli [48]. Their synaptic architecture supports a more gradual and sustained neurotransmitter release.

4.2.3. Synaptic membrane and excitatory postsynaptic currents (EPSCs)

The synaptic membrane is the interface between the hair cell and the vestibular nerve. It consists of two parts, the presynaptic membrane and the postsynaptic membrane. The presynaptic membrane is found at the end of the haircell that transmits vesicles with neurotransmitters, as can be seen on the right side in Figure 4.1. The postsynaptic membrane is located on the receiving neuron's cell body and houses receptor proteins that bind to the neurotransmitters.

Excitatory postsynaptic currents (EPSCs) are the electrical currents that result from the activation of excitatory neurotransmitter receptors at the postsynaptic membrane. When an excitatory neurotransmitter, such as glutamate, binds to its receptor on the postsynaptic neuron, it triggers the opening of ion channels, typically allowing sodium (Na+) ions to flow into the cell. This influx of positive ions depolarizes the postsynaptic membrane, generating an EPSC and potentially leading to an action potential if the depolarization is sufficient [88].

In order to model the neurons, we should take into account the characteristics of these EPSCs.

The characteristics of EPSCs include their amplitude, rise time, and decay time. The amplitude of an EPSC reflects the amount of neurotransmitter released and the number of receptors activated. Rise time is the time taken for the EPSC to reach its peak after the neurotransmitter release, typically on the order of milliseconds. The decay time, the period during which the EPSC returns to baseline, can vary depending on the types of receptors and the synaptic environment, ranging from milliseconds to several tens of milliseconds [88].

The shape of excitatory postsynaptic currents (EPSCs) reflects the dynamics of synaptic transmission and receptor activation. In vestibular neurons, EPSCs typically exhibit rapid rise times and a slower, exponential decay. The rise time is usually on the order of a few milliseconds, indicating fast synaptic transmission, while the decay time can vary more widely, often ranging from a few milliseconds to tens of milliseconds [38].

The specific shape of EPSCs in vestibular neurons is influenced by the types of receptors involved and the synaptic environment. For example, AMPA receptors, which mediate most of the fast excitatory transmission, contribute to the rapid rise and initial decay phase of the EPSC. NMDA receptors, which have slower kinetics, can prolong the decay phase, adding a slower component to the EPSC shape. The interplay between these receptor types and their kinetics results in the characteristic EPSC shape observed in vestibular neurons [37].

In this thesis we will use one of the EPSC shapes that was defined by Hight and Kalluri [36]. They modeled EPSCs using three different shapes, see Figure 5.17. The modeling of three different shapes was based on several factors that could cause variations in EPSC shapes, including differences in AMPA receptor subunits [64], NMDA receptors [42], and glutamate accumulation in the synaptic cleft [74]. In addition, multiphasic EPSCs [34], attenuation, and slowing of synaptic events due to propagation along dendritic arbors were considered.

The shape of the first excitatory postsynaptic current (EPSC) can be described by the alpha function:

$$s_1(t) = \frac{t}{\alpha^2} e^{-t/\alpha}, \alpha = 0.4.$$

The value 0.4 for α was determined by fitting the alpha function to recordings of EPSCs from inner hair cell terminals [30]. This value specifies the length of time for a single EPSC. It should match the majority of synaptic events [83]. Other shapes were modelled as well, but they seem to be less prevalent in vestibular synaptic transmission. The recordings where the shape is based on are from vestibular calyx endings. Our understanding of synaptic events at vestibular bouton (typical for regular afferents) terminals is limited. Since regular afferents seem to measure more tonically (sustained), we could argue that a shape like s_3 , where the event is slower and more sustained, might characterize the bouton's EPSC transmission.

There are some limitations to using EPSC shapes only, since the Kalluri et. al did not model more complex synaptic mechanisms, such as proton-based signaling [35] and other non-quantal transmission modes observed in calyx terminals [86, 96]. These mechanisms run in parallel to the neurotransmitter mechanism and are argued to be more metabolically efficient in evoking depolarizations of the postsynaptic neuron. These mechanisms are believed to exist in calyx terminals only.

Motion sickness during and after changing gravity environments, like in spaceflight, is quite prevalent. The NMDA receptors are believed to play an important role in the vestibular system's ability to adapt to changes in gravitational forces [54]. In rats, the body regulates the neuron's firing homeostasis by adjusting the number of NMDA receptors. This reduces the rate of action potential (AP) and thus creates unusual responses and possibly inaccurate motion perception. We won't model sustained hypergravity, but this research does confirm the importance of modelling the receptors to fully explain the vestibular spike rate behaviour and the onset of motion sickness.

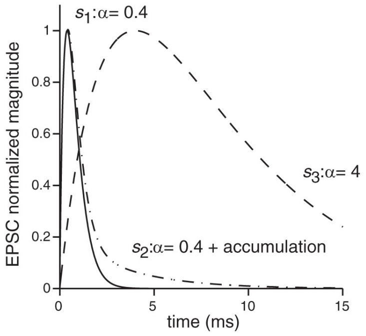

Figure 4.3: Variety of EPSC shapes relevant for the otolith afferents. Figure from [36]

4.2.4. Axons: regular and irregular afferents

Vestibular afferents are the sensory nerve fibers that transmit information from the vestibular hair cells in the inner ear to the central nervous system. Axons from the vestibular ganglion join with axons from the auditory neurons to form the eighth nerve (CN VIII). The vestibular axons split from the auditory axons and project to the vestibular nuclei and cerebellar regions [53]. Afferent nerve fibers exhibit a wide range of axon diameters, corresponding to diverse response properties. Thin afferent fibers typically show regular firing characteristics, while thicker afferents seem to be more irregular in their firing activity [22]. This applies both to the semicircular canals as the otoliths.

Vestibular afferents can be categorized into two main types based on their firing patterns and physiological properties: regular and irregular afferents.
Regular afferents exhibit relatively constant inter-spike intervals and are thought to be more involved in encoding the magnitude and direction of head movements. These afferents are mainly connected to type 2 hair cells.
In contrast, irregular afferents have more variable inter-spike intervals and are believed to be more sensitive to high-frequency head movements and transient stimuli [26]. These afferents are primarily connected to type 1 hair cells.

Studies in frogs and fish, which only have type II hair cells, show that despite the absence of type I hair cells, some afferents exhibit irregular resting discharge while others display regular resting discharge [43]. This clearly demonstrates that hair cell type does not determine the regularity of resting discharge, but axon characteristics do. As Eatock et al.[22] have pointed out, the firing patterns of isolated vestibular ganglion somata are influenced by intrinsic ion channel properties, which, when combined with hair cell synaptic drive in vivo, result in either regular or irregular firing patterns.

In total, a human has about 40,000 vestibular afferents [95]. In humans, each utricular macula contains approximately 33,000 receptors, which synapse onto around 6,000 afferent neurons. Similarly, each saccular macula has about 18,000 receptors, synapsing onto roughly 4,000 saccular afferent neurons [6]. As sampled by Fernández et al. in monkeys [26], less than 20% of the afferents are irregular.

These afferents connect to the vestibular nuclei (VN), where the signals get processed and integrated with other sensory and motor stimuli. Since the vestibular nuclei have a structure that is not fully understood yet and we only model vertical accelerations, we will limited our model to the otolith afferents.

For models that include multi-sensory integration in the higher sections of the brain I refer to the models defined by Angelaki et al. [2].

4.2.5. Otolith distribution and location (saccule vs. utricle)

The amplitude and frequency of spike responses can vary depending on the direction and magnitude of the stimulus. Typically, larger accelerations or more significant tilts result in higher amplitude and frequency of spikes. The exact nature of these responses can differ among the different otolith directions due to the anatomical orientation and distribution of hair cells in the otolith organs.

The temporal dynamics of spike responses, including the speed of adaptation, can vary. For instance, fore/aft otoliths may adapt more quickly or slowly to sustained stimuli compared to lateral or vertical otoliths, depending on the specific physiological properties and functional demands of the organism's environment. Since there is limited data available and Schneider et al. [85] stated that they couldn't discriminate between signalling from saccular and utricular afferents, we may assume research from utricular afferents is applicable for saccular afferents as well.

4.3. Regular and irregular otolith response characteristics

The characteristics of regular and irregular otolith afferents, including their distinct firing patterns, phase locking capabilities, and varying sensitivities, are crucial for defining parameters in our neural response simulations. By understanding these attributes, we can accurately model the spiking behavior of otolith neurons in response to different motion stimuli. In this section, we will present a comprehensive overview, systematically detailing all relevant characteristics to ensure our model reflects the behavior of these neural pathways.

The classification of vestibular afferents into "regular" and "irregular" was first proposed by John I. Goldberg and Charles Fernández in their research during the 1970s [26][24]. Their work focused on the firing patterns of these afferents in the vestibular system, leading to the widely recognized distinction between regular and irregular afferents based on their variability in firing rates.
This classification helps understanding how different afferent contribute to self-motion perception. However, it's important to note that the characteristics or behaviors being described don't fit neatly into just two categories. Instead, there is a range or continuum of variations between the extremes. While some afferents clearly fall into "regular" or "irregular" categories, other might exhibit characteristics that lie somewhere in between. For now, focusing on these two categories simplifies modeling, but future work can incorporate the full range of variations to capture the complexity of vestibular afferent behavior more accurately. The distinction also aligns with Cullen's statement "Current evidence therefore supports the idea that there are two parallel and distinct peripheral sensory channels representing vestibular information in mammals" [15]. She states that there are two channels; one (regular) that encodes small amplitude stimuli through firing rate and another (irregular) that is optimized for the natural range of head motion, using a nonlinear code based on precise spike timing. What this exactly entails will be explained in the following sections.

4.3.1. Variability:

Regular otolith afferents, as the name says, typically exhibit a more consistent and steady firing rate, resulting in lower variability. In contrast, irregular otolith afferents display higher variability in their firing patterns.

The coefficient of variation (CV) is a statistical measure used to quantify the variability of a set of data relative to its mean. In the context of vestibular neurons, the CV is often used to assess the variability in the mean spike interval (ISI) of these neurons.

The CV is calculated as the ratio of the standard deviation of the firing rate to the mean firing rate:

$$\mathrm{CV} = \frac{\text{Standard Deviation of ISIs}}{\text{Mean of ISIs}}$$

In vestibular neurons, the CV provides insight into how consistent or variable the firing rate is over time.

A low CV (close to 0) indicates that the neuron's firing rate is relatively consistent and stable, with low variability around the mean. This is typically seen in regular vestibular afferents, where the firing is more uniform and predictable. In contrast, a high CV (>0.15): Suggests a high degree of variability in the neuron's firing rate, meaning that the firing rate fluctuates significantly over time. This is characteristic of irregular vestibular afferents, which exhibit more random firing patterns.

Neural variability is a widespread phenomenon across the central nervous system (CNS), observed as fluctuations in the activity of neurons even under consistent conditions. This variability raises questions about its role in neural coding. Some researchers argue that it represents noise, potentially disrupting the accurate transmission of information. Others suggest that variability might play a functional role, contributing to processes like sensory adaptation, decision-making, or enhancing the brain's flexibility in response to a dynamic environment. Despite extensive study, the exact contribution of neural variability to neural coding remains a topic of active debate and research within neuroscience [23]. In our model we will assume the variability as noise. This aligns with the view that variability can obscure or distort the signal, thereby affecting the precision of neural coding. By treating variability as noise, we can focus on the core aspects of information processing without the added complexity of modeling potential functional roles for variability.

As mentioned by Schneider et. al [85], the increased variability observed in irregular afferents may simply be a byproduct of their heightened gain. The negative impact of this increased variability on coding and feature detection could be mitigated by averaging the signal across a large populations of afferents. There is a strong correlation between increased variability and sensitivity in the vestibular system [45]. This can be explained by the intrinsic properties, i.e. an increase in the density of low-voltage-activated potassium currents [51]. This supports the proposition that variability is a byproduct of their heightened gain.

Note that most data on variability in otolith afferents is typically recorded under static conditions, where the head or body is not undergoing significant movement. This approach enables researchers to focus on the intrinsic properties of these afferents without the interference of movement-related stimuli, such as acceleration or changes in head position. Recording under static conditions helps in understanding the baseline firing rates and variability of irregular afferents, providing insights into how these neurons function in a resting state. However, the variability observed under static conditions might not fully capture their behavior during real-world dynamic situations. While static recordings are valuable for understanding fundamental properties, they may not reflect the full range of variability that these afferents exhibit during active motion. Therefore, while static data is important, it represents only a part of the overall picture, and complementary studies involving dynamic conditions are necessary to fully understand the functional implications of variability in irregular otolith afferents.

What we do know, is that the standard deviation decreases when the interspike interval decreases. However, this doesn't seem to be linearly related. Correia and Landolt [14] observed that the coefficient of variation (CV) scales with the square root of the mean interval length (t) in their data, a relationship also evident in the earlier data by Goldberg and Fernandez [25]. This is indicated by the fitted lines in Figure 4.4. Note this is based on semicircular canal data, but we assume that it is similar for the otolith afferents.

The relationship can be expressed as:

$$\mathrm{CV} \propto t^{1/2}$$

This square-root relationship suggests a simple stochastic process underlying the spike generation in all afferents. However, while this scaling is characteristic of an inverse Gaussian process, Correia and Landolt rejected this model as it did not adequately fit their data.

The logarithmic scaling, particularly for regular neurons, may also involve large relative errors due to digitization artifacts from the original publication. However, since the power law is consistent with the data for irregular and intermediate afferents it is fitted to the regular neurons as well.

The trial-to-trial variability of the afferents is important as well. It refers to the fluctuations in the response of a neuron or neural circuit across multiple presentations of the same stimulus. Even when the exact same conditions are maintained, the neuronal response can vary from one trial to the next. This measure is more concerned with how consistent a neuron's response is when exposed to the same stimulus multiple times. It gives insight into the reliability of neural coding and how external or internal factors might affect neuronal activity on a trial-by-trial basis. The standard deviation of ISI shown previously, is a measure that is more focused on the temporal precision and regularity of a neuron's firing pattern. It provides insight into the regularity of neuronal firing and can distinguish between regular (more consistent ISI) and irregular (less consistent ISI) firing patterns.

Schneider [85] observed that irregular afferents exhibited greater firing rate variances compared to regular afferents, which was anticipated. However, a key finding was that the firing rate variance sig-

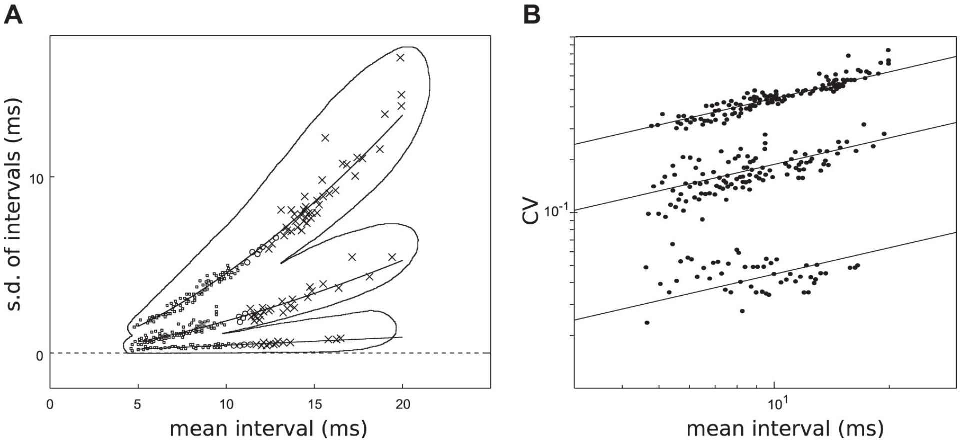

Figure 4.4: Relationship between A: standard deviation and mean interspike interval, and B: Coefficient of Variation and mean interspike interval.
Bottom: a regular, middle: an intermediate, and top: an irregular semicircular canal afferent neuron.
From [78] using data from [32].

nificantly decreased for stimulus intensities that caused saturation, with this effect being particularly pronounced in irregular afferents. This suggests that when neurons operate within a nonlinear range, their variance diminishes sharply. This observation is consistent with what we see in Figure 4.5A for irregular otolith afferents.

As can be seen in figure 4.5, in the experiment done by Schneider et. al [85] regular afferents (top) displayed less firing rate variance than irregular afferents (bottom). Including the measured firing rate variance only slightly alters the shape of the optimal stimulus distribution. This can be observed by comparing the dashed curves (which account for variability) to the solid black curves (which do not account for variability) for both regular (top) and irregular (bottom) afferents. The concept of an “optimal stimulus distribution” refers to the distribution of sensory inputs that maximizes the amount of information transmitted by a neuron or a population of neurons. In other words, it represents the range and frequency of stimuli that the nervous system is best tuned to detect and encode efficiently. An optimal stimulus distribution centered around 0G indicates that the afferents theoretically encode information most efficiently around low frequencies.

As Schneider et al. conclude: ”While previous studies have found that variability plays an important role in vestibular coding [32][84][45], our results show that sensitivity largely determines the corresponding optimal stimulus distribution.

An alternative theory, stochastic resonance, is that the presence of noise in a system actually enhances the detection or transmission of weak signals, rather than merely adding interference. In the context of otolith afferents stochastic resonance (SR) can play a significant role in improving the sensitivity and responsiveness of these neurons to weak stimuli. This counterintuitive effect has been studied in various biological systems, including isolated hair cells and the bullfrog sacculus. However, the presence of SR in the developing vestibular system has not been thoroughly explored.

It is plausible, and perhaps even likely, that the noise observed in otolith afferents originates from various sources and serves functions that are not yet fully understood. However, for the purposes of this thesis, we assume that the variance in afferent activity reflects uncertainty in the sensory input. This assumption allows us to model and analyze the system under the premise that greater variance corresponds to greater ambiguity in the detected stimulus.

4.3.2. Sensitivity:

According to research [45, 1] regular and irregular afferents have a similar average resting rate, which is about 79 spikes/s +- 5 spikes/s. However, when stimulating the afferent along its preferred direction with linear acceleration at different frequencies, irregular afferents show higher sensitivity for the whole frequency range. Otolith irregular afferents also show a higher increase in sensitivity as frequency in-

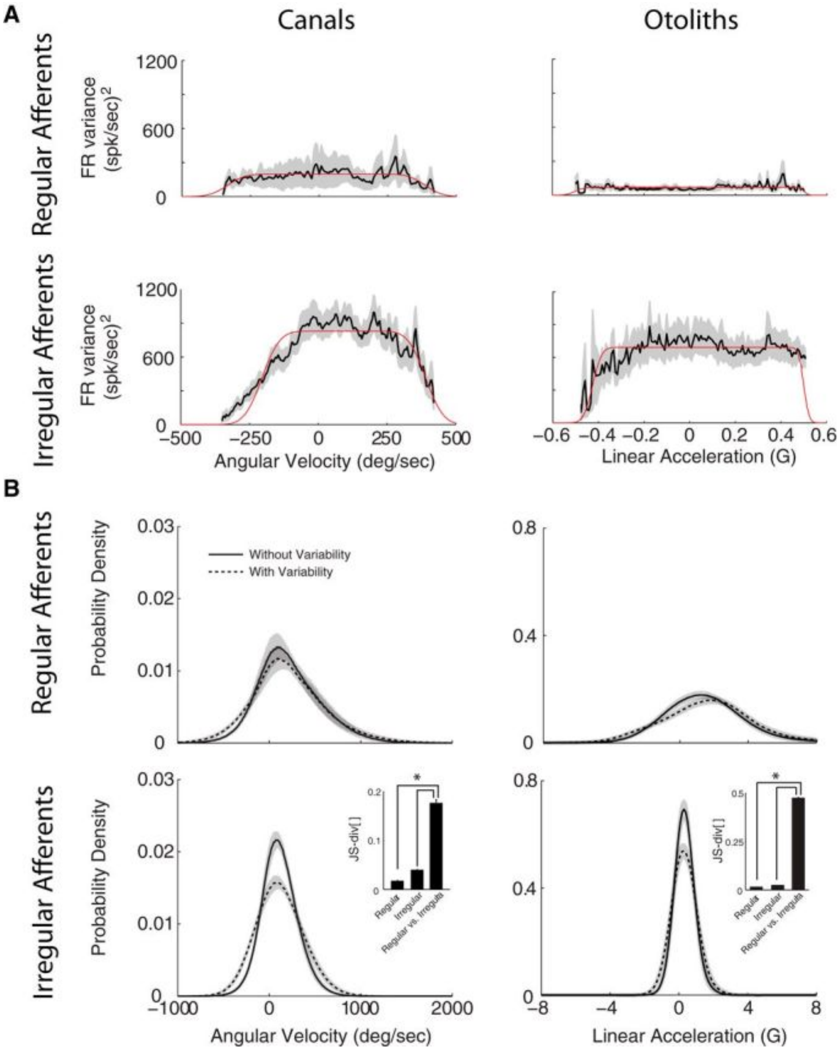

Figure 4.5: As shown in the figures in the second row, the trial-to-trial Firing Rate variance decreases for both canals and otoliths as the linear acceleration becomes more negative or more positive. The inclusion of variance/noise (dashed lines), however, doesn't have a great effect on the resulting probability densities that have been defined by Schneider et. al. [85].

creases, see figure 4.6. This indicates that otolith afferents exhibit high-pass tuning, with their response magnitude becoming increasingly pronounced as the frequency of the stimuli rises.

Regular afferents have a consistent, regular firing rate at rest, and their response to stimuli is usually proportional to the intensity of the input. These afferents tend to have a lower sensitivity to sudden changes in head position but are more reliable in signaling sustained, steady stimuli over time.

Irregular afferents have a more variable firing rate at rest. They are typically more sensitive to rapid changes in acceleration and head movements. This higher sensitivity makes them particularly effective at detecting transient or sudden movements. Irregular afferents provide the brain with more immediate, but less consistent, information about the direction and magnitude of head movement.

The sensitivity difference between these two types of afferents plays a crucial role in how the vestibular system processes various types of motion. Regular afferents are better suited for detecting slower, prolonged changes in head position, such as those experienced during steady linear acceleration or head tilt. Irregular afferents, with their high sensitivity, are more attuned to detecting quick, sharp movements, such as those experienced during sudden head turns or jolts.

Irregular afferents are believed to be tuned to high frequencies as an adaptation to natural vestibular stimuli, allowing for a more balanced distribution of encoding capabilities across different frequencies. This tuning is particularly beneficial for detecting faint high-frequency signals that could be masked by environmental noise, which is essential for quick reflexive responses to sudden, high-frequency events. On the other hand, regular afferents, with their broader frequency tuning, are thought to be better suited for tasks like the vestibulo-ocular reflex, where precise encoding of lower-frequency head movements is necessary [10].

Cullen [15] states that irregular otolith and canal afferents are better optimized to process natural stimuli than regular afferents because their optimal stimulus distributions more closely match the natural stimulus distribution. These findings raise an important question: if irregular afferents are more sensitive to head motion and better suited for encoding natural vestibular stimuli, why do regular vestibular afferents exist? Recent research provides some insight. It has been shown that regular canal afferents are more effective at rate coding, transmitting twice as much information across the range of normal head movements compared to irregular afferents, and they also have significantly lower detection thresholds. On the other hand, irregular afferents excel at discriminating between different stimulus patterns by producing distinct spike timing patterns within a very short timeframe (around 6 ms). Preliminary studies suggest that irregular otolith afferents may also exhibit this precise spike timing capability.

However, it is important to recognize that the response graphs were generated based on linear modeling assumptions. The observed characteristics were identified when neurons were subjected to relatively low-intensity stimuli, such as linear head accelerations of 0.2G. Under these conditions, neurons are largely operating within their linear range, which may not fully capture their behavior under more intense stimuli.

Additionally, the graph does not depict frequencies outside the 0.1 to 15 Hz range. While there is data available for static gain, modeling motion sickness primarily requires understanding responses at lower frequencies, as the onset of motion sickness typically occurs within this lower frequency range, making data beyond 15 Hz less critical for this purpose.

4.3.3. Phase:

Irregular afferents show a larger sensitivity, but also a higher phase lead compared to regular afferents. This suggests that irregular afferents are more responsive to changes in stimuli, especially at higher frequencies. A “higher phase lead” means that these afferents respond more quickly to the stimulus, with their output leading the input signal by a greater amount of time compared to regular afferents. This can indicate that irregular afferents are better suited for detecting and processing rapid, transient movements, which is crucial for initiating quick reflexive responses.

4.3.4. Non-linearity:

Highly sensitive irregular otolith afferents, which are responsible for detecting linear accelerations such as those caused by gravity and head movements, exhibit a strong non-linearity known as “inhibitory cutoff.” This means that during intense stimulation, such as the forces experienced during running,

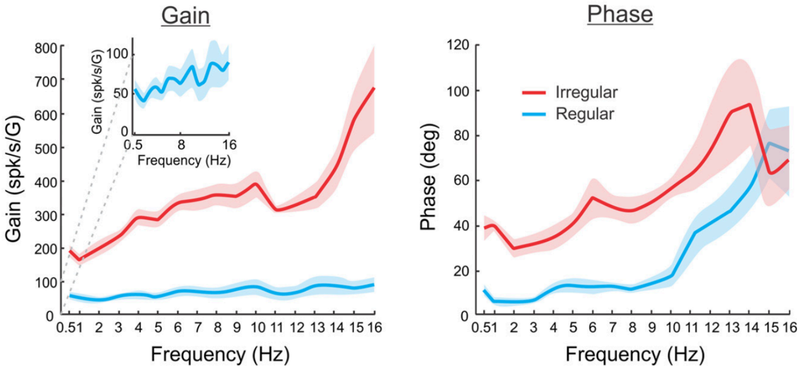

Figure 4.6: Gain and phase lead relative to the motion frequency, from [45].

these afferents reach a point where further increases in stimulus intensity do not lead to a proportional increase in their response. Instead, their firing rate may plateau or even decrease. This non-linear behavior helps to prevent overstimulation and ensures that the sensory signals remain within a range that the nervous system can effectively process.

The inhibitory cutoff acts as a protective mechanism, preventing the afferents from being overwhelmed by excessively strong stimuli, while still allowing them to be highly sensitive to smaller, more relevant changes in motion.

In everyday life, the representation of self-motion by early vestibular pathways is non-linear, unlike the linear encoding observed when tested within a very narrow range of amplitudes and frequencies under passive conditions. Due to the high amplitude accelerations during daily activities, this non-linear processing is crucial for handling the diverse stimuli. Both vestibular afferents and their target neurons in central pathways utilizing precise spike timing and other advanced coding strategies. However, when the vestibular system is activated during voluntary movements rather than passive self-motion there are other mechanisms in play that might cancel out the signaling from the vestibular neurons [16]. The cancelling of active self-motion is out of scope of this thesis, which means we will focus on the afferent signalling only and not the central processing in the vestibular nuclei.

4.3.5. Human relevant accelerations

In our model we will take into account human relevant accelerations. As you can see in table 4.1 from [11], during self-generated active movements the accelerations are higher then during passive motion like riding the bus. So, we would expect the sensory system to be better adapted to those active kind of accelerations. Vertical accelerations when being upright and static you should consider as 0G in this table. This table can be used as a reference by the reader to get an idea about the magnitude of accelerations we discuss.

4.3.6. Distributed and parallel processing

In our model we will include a distributed approach to mimic the brain's strategy. The strategy of parallel processing for sensory information is extensively used across different modalities, including auditory [90, 72, 29], visual [63, 61, 66], and electrosensory [9, 4, 52] systems. This approach enables the encoding of various stimulus attributes. Additional studies are required to explore the hypothesis that the vestibular system employs separate channels of peripheral input to represent different aspects of natural vestibular stimuli. The study by Jamali et. al [48] does argue that the regular and irregular neurons are better in encoding different attributes of acceleration stimuli.

4.3.7. Phase Locking, Spike Timing, Frequency Propagation

Neurons have a limit to their firing range due to several biological constraints. These include the refractory period, which is the brief time after a spike during which a neuron is unable to fire again, and the energy demands associated with maintaining ion gradients across the cell membrane. These constraints ensure that neurons do not overheat or deplete their energy resources, allowing them to

Table 4.1: Subject-averaged peak head accelerations across tasks[a]

Task	Interaural (G)	Fore-aft (G)	Vertical (G)
Active:			
Walking	0.9 ± 0.1	1 ± 0.1	1 ± 0.1
Running: woods	2.1 ± 0.6	2.4 ± 0.7	4.1 ± 1
Jump up	0.9 ± 0.1	2.2 ± 0.2	2.9 ± 0.2
Hopping	1.1 ± 0.2	2.1 ± 0.3	2.8 ± 0.2
Jump forward	1.2 ± 0.2	3.7 ± 0.6	3.3 ± 0.6
Running: pavement	1.1 ± 0.1	1.8 ± 0.1	2.4 ± 0.1
Going up the stairs	0.8 ± 0.1	1.3 ± 0.3	1.8 ± 0.2
Sprinting	2 ± 0.3	2.2 ± 0.2	3.9 ± 0.4
Soccer	3.1 ± 0.6	3.8 ± 0.6	3.3 ± 0.3
Passive:			
Metro ride	0.4 ± 0.1	0.6 ± 0.1	0.4 ± 0.0
Bus ride	0.5 ± 0.1	0.7 ± 0.1	0.4 ± 0.1

[a] Data are mean ± SEM.

function efficiently and maintain their role in information processing over time.

Spikes in the membrane potential of neurons are fundamental to how the brain processes information. For neurons to effectively translate information from their various inputs into meaningful changes in their spike patterns, the rate at which they emit spikes is crucial. If a neuron's mean firing rate is either close to its maximum or near zero, alterations in inputs have minimal influence on its firing rate. Hence, neurons must regulate their mean firing rate to ensure effective information processing [67]. For the irregular neurons this means that at high frequencies, when their gain is high [48], they might not be able to fire at every cycle. However, the spikes are phase-locked, which means that they occur in the same phase of the cycle when they occur.

The auditory afferents, which evolutionarily originate from the vestibular afferents, are capable of transmitting sound information that is higher then the maximum firing rate of a single neuron. The volley principle explains that because individual neurons cannot fire more than a certain number of spikes per second, groups of neurons work together by alternating their firing. These neurons fire in quick succession, creating a combined frequency that exceeds the spiking rate limit of an individual neuron.

Place theory suggests that we perceive sound based on where each frequency causes vibrations along the basilar membrane. Rate–place schemes describe auditory perception based on neural firing rates at different places. The main alternative is the temporal theory, also called the timing theory, which involves the volley principle. Here, groups of neurons work together to encode the timing of sound waveforms. Place–volley theory combines both approaches, using timing patterns for low pitches and rate–place patterns for high pitches. There is strong evidence supporting both mechanisms for auditory neurons [75]. For vestibular neurons the place theory hasn't been proposed, but temporal precise spiking is measured.

Phase lock occurs only in irregular neurons and can be activated by bone-conducted vibration (BCV) and air-conducted sound (ACS). Both sound and vibration possibly generate fluid pressure waves in the inner ear [18]. These pressure waves displace the hair bundles on vestibular receptor hair cells, leading to the activation of type I receptor hair cells and the phase locking of action potentials in the irregular vestibular afferents, which synapse on type I receptor. Using BCV and ACS stimulation we can trigger responses from the irregular otolith afferents only, making them a good tool to investigate the influence of afferent types on motion sickness. An example of phase locking to BCV can be seen in Figure 4.7.

4.3.8. Detection thresholds

Human perception of self-motion relies on the integration of information from multiple sensory systems, including visual, vestibular, and proprioceptive inputs. A critical aspect of this integration is the ability to discriminate between different types of motion, particularly translational accelerations. Research in this area has primarily focused on determining the absolute and difference thresholds for various motion

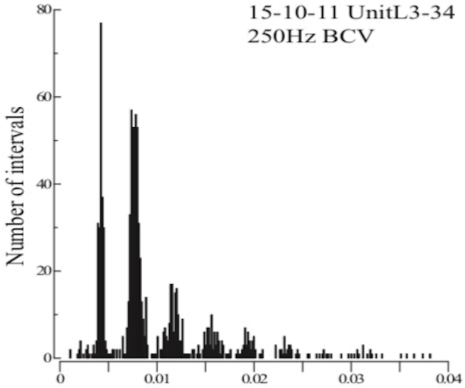

Figure 4.7: Phase-locking to bone conducted vibration (BCV) with a frequency of 250vHz, the figure shows that the otoliths afferent phase-lock. Spiking happens in harmonics of 250 Hz. From [18].

Table 4.2: Perception thresholds for different linear accelerations, from [68].

	Task	Stimuli	Threshold (m/s2)		
			Surge	Sway	Heave
Benson et al. (1986)	Discrimination	0.33-Hz sinusoidal acc	0.06	0.06	0.15a
Zaichik et al. (1999)	Detection	0.95-Hz sinusoidal acc	0.03	0.05	0.08
MacNeilage et al. (2010)	Discrimination	1-Hz sinusoidal acc	–	0.06	0.10
Roditi and Crane (2012)	Discrimination	1-Hz sinusoidal acc	0.03	0.03	0.08
Valko et al. (2012)	Discrimination	1-Hz sinusoidal acc	–	0.02	0.05
Soyka et al. (2011) (model)	Discrimination	1-Hz sinusoidal acc	0.02b	0.02b	–

types.

A study [68] on human discrimination of translational accelerations employed psychophysical methods to assess how well individuals could distinguish between different sinusoidal accelerations in the horizontal plane. The study measured difference thresholds across a range of acceleration amplitudes (0.5 – 2.0 m/s^2) and frequencies (0.25–0.6 Hz). The results revealed that difference thresholds varied from 0.05 m/s^2 at lower amplitudes to 0.13 m/s^2 at higher amplitudes, demonstrating a pattern consistent with Weber's law, which describes the proportional relationship between stimulus intensity and perception thresholds in other sensory modalities.

Weber's Law is a principle in psychology that explains how we perceive differences between stimuli. It posits that the smallest noticeable difference between two stimuli is not a fixed amount, but rather a constant proportion of the original stimulus intensity. In other words, the ability to detect a difference between two stimuli depends on their relative, rather than absolute, difference in intensity.

Naseri et al.[68] mention that within studies, thresholds are consistently higher for vertical movements. They formulated table 4.2.

Research has demonstrated that the coding strategies employed by otolith afferents to encode linear motion differ significantly from those used by semicircular canal afferents to encode rotational motion. Studies by Sadeghi et al.[84] and Jamali et al.[45] have been important in highlighting these differences. One of the key findings is the observation of a strong correlation between trial-to-trial variability and sensitivity in otolith afferents. This relationship is particularly noteworthy because it ensures that the ratio of variability to sensitivity remains constant across different conditions. As a result of this constant ratio, the neural detection thresholds for otolith afferents, defined as the minimum stimulus intensity required to elicit a detectable change in neural activity, are independent of both resting discharge variability and frequency as can be seen in Figure 4.8. There does seem to be a lower threshold for very low frequencies, however. This characteristic sets otolith afferents apart from semicircular canal afferents, which have different coding dynamics. The independence of neural detection thresholds from variability and frequency in otolith afferents suggests that they are finely tuned to consistently detect linear accelerations, regardless of inherent variability or stimulus frequency.

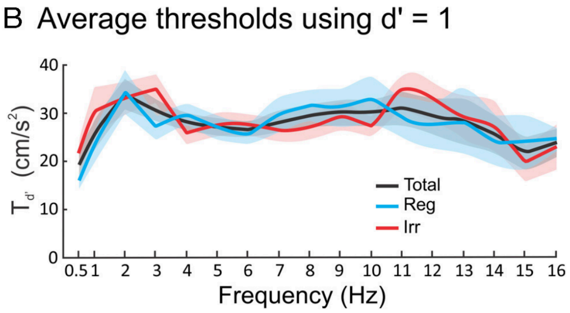

Figure 4.8: Detection thresholds for regular and irregular otolith afferents. Figure 3B from [45].

Findings by Kovel et. al [55] reveal significant differences in motion perception thresholds across different axes. Specifically, the threshold for y-translation (horizontal motion) was approximately half that of z-translation (vertical motion). This result aligns with the work of MacNeilage et al. [62], who suggested that the utricles, which are primarily responsible for detecting horizontal motion, may be more sensitive than the saccules, which detect vertical motion. This hypothesis is further supported by the greater density of hair cells found in the utricles compared to the saccules [65]. However, the authors note it is important to consider additional factors, such as the potential complexity in perceiving changes in gravitational force during vertical movements and the availability of supplementary sensory information, like tactile feedback, during horizontal translations.

4.3.9. Sensitivity symmetries at the afferent level

The authors also observed a significant influence of gravity on vestibular bias at 2-Hz thresholds, manifesting as a positive bias that indicates a heightened sensitivity to downward motion compared to upward motion. It has been argued that the importance of downward motion is greater in detecting falls, or that the assymetry is due to assymetry in somatosensory cues[70]. Jamali [47] found that at the level of vestibular afferents, there is no difference in sensitivity for up and down translations. We will thus not consider this assymetry.

The research by Jamali (2009) [47] included recordings from 48 otolith afferents during active and passive translations. They revealed that the afferents showed comparable sensitivity to head acceleration across both saccular and utricular innervation. The study found no significant differences in sensitivity between regular and irregular afferents, nor between afferents innervating the saccule versus the utricle. Additionally, the findings indicated that primary otolith afferents were not differentially influenced by the efferent pathway during active versus passive head translations.

The study also highlighted that saccular receptors, unlike utricular receptors, are biased at rest due to the constant gravitational force, but their response remained within the linear range during the stimuli used. Lastly, the study found no significant difference in the sensitivity and phase of saccular versus utricular afferents, although irregular afferents exhibited greater maximal sensitivity than regular ones. This means that we can use the horizontal/utricular spiking data characteristics when modelling vertical motion.

Especially this last finding is important for our model, since it indicates we can use the data from Jamali (2019) [48] to describe the otolith response accurately.

4.4. Summary using Jamali et al. (2019)

The study by Jamali et al. [48] highlights that irregular and regular otolith afferents utilize different strategies to encode gravito-inertial forces. Irregular afferents show stronger response nonlinearities and transmit more information about dynamic translational self-motion through both firing rate changes and precise spike timing, as can be seen in Figures 4.9 and 4.10, respectively. Regular afferents, on the other hand, are more effective at encoding static head orientation relative to gravity due to their low variance as can be seen by the narrow blue distribution in Figure 4.9B.

Irregular afferents display a greater tendency for precise spike timing and phase locking in response to sinusoidal stimuli [18]. This precision in spike timing is strongly linked to their ability to phase lock, which is a key mechanism for encoding high-frequency components of naturalistic translational motion. The study found that irregular afferents, despite having higher resting discharge variability, exhibit lower trial-to-trial variability during naturalistic translational self-motion stimuli. According to Jamali et al., this lower variability in irregular afferents is due to their nonlinear response characteristics, which contribute to their higher information transmission rates.

By integrating these findings into our model, we can enhance its accuracy and reliability in predicting motion sickness, particularly in scenarios involving vertical motion, where the distinction between regular and irregular afferents plays a crucial role. Aligning our model with neurophysiological data will ensure that it closely reflects real biological processes, which enhances its accuracy and usefulness.

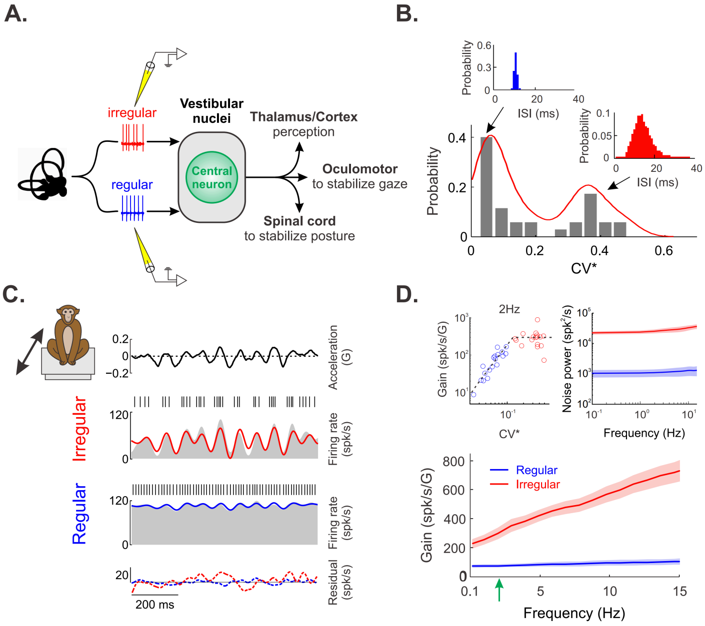

Figure 4.9: Experimental data showing the response of regular and irregular afferents to translational motion stimuli. From [48].

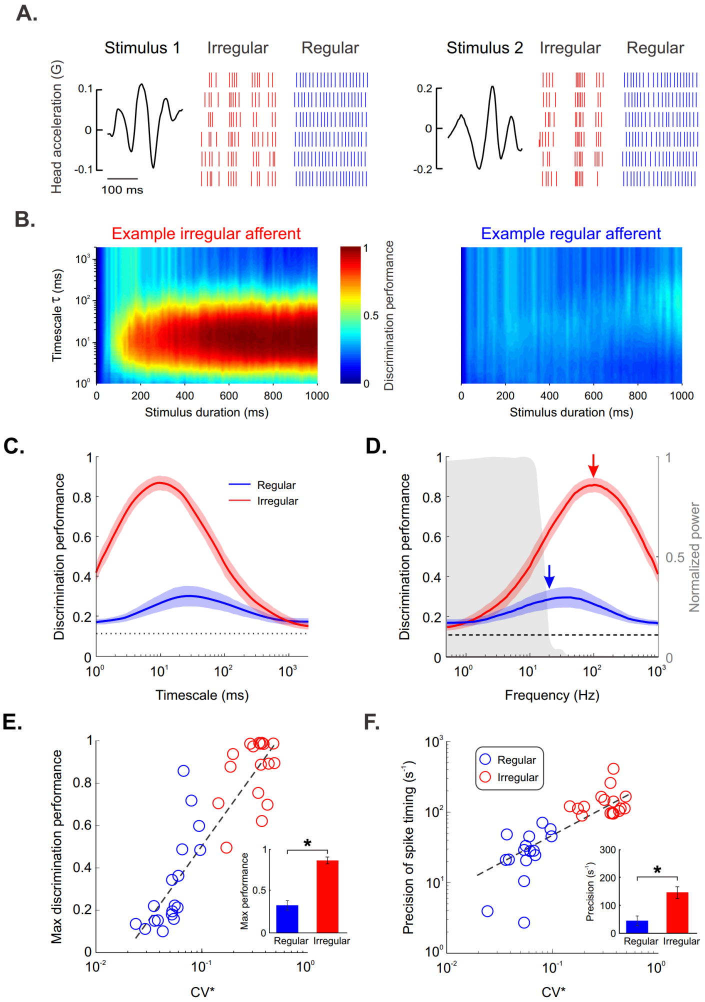

Figure 4.10: Irregular but not regular otolith afferents reliably discriminate between different stimulus waveforms through precise spike timing. From [48].

5

Spiking Neuron Models

5.1. Introduction

It is proposed the brain regions responsible for processing signals from otolith afferents (such as the vestibulocerebellar pathways) operate as a dynamic filter to perform Bayesian estimation of head movements, as proposed by researchers like Paulin [77] and Kuo [58]. If this is the case then to model perception and subsequent motion sickness, it is important to model how the brain decodes spike train data from the vestibular nerve to infer the Bayesian posterior distribution of head motion.

Developing such a model requires first constructing a generative model of the data, which can simulate neural responses based on different head kinematic states. As we identified the spiking characteristics in the previous chapter, we know that the model should be able to simulate both the responses from regular and irregular afferents, including their stochastic distributions.

We will begin by selecting appropriate types of spiking neuron models, followed by defining the input dynamics for these models. Finally, we will implement three different spiking models to explore their behavior. Figure 5.1 provides an overview of the entire model, highlighting the specific modules we will focus on in this chapter.

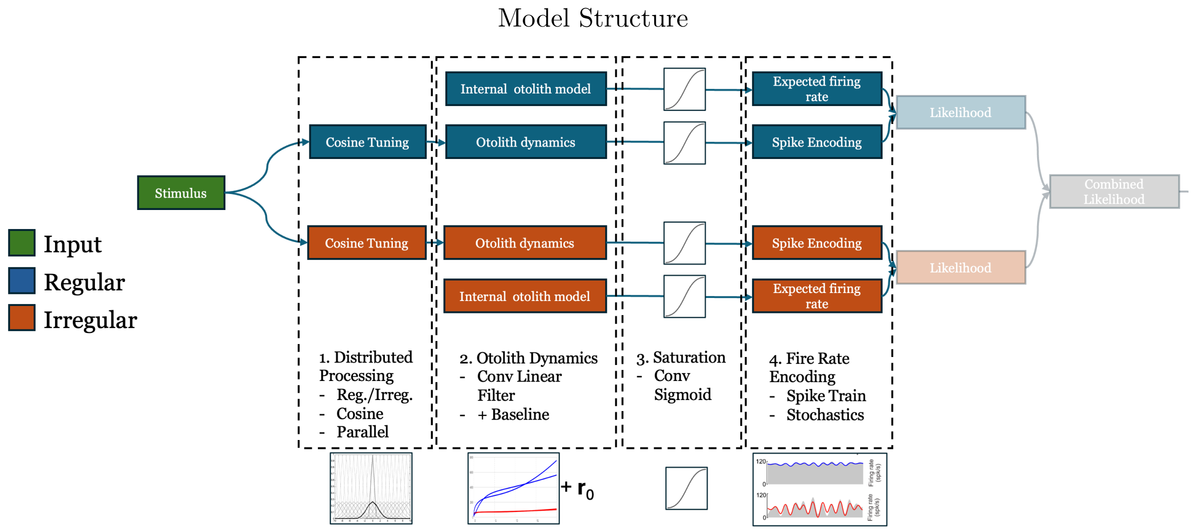

Figure 5.1: This chapter we will go through the highlighted modules.

5.2. Spiking Models

To simulate the spiking behavior of otolith afferents, we require models that can accurately predict how neurons respond to various stimuli. While neurons are biologically complex, spiking models allow us to abstract and capture the essential features of neuronal firing. The objective is to utilize a single foundational model capable of simulating both regular and irregular spiking behavior. This approach not only simplifies the modeling process but also enhances the consistency and comparability of the results.

Drawing on literature where vestibular neurons have been modeled [44][78][48][36], we considered the following types of models:

1. Integrate-and-Fire (I&F) Model
2. Generalized Linear Model (GLM)
3. Hodgkin-Huxley (HH) Model
4. Izhikevich Model
5. FitzHugh-Nagumo (FHN) Model

The Integrate-and-Fire model is one of the simplest and includes variations like the Leaky Integrate-and-Fire model. It effectively captures the basic spike generation mechanism based on the dynamics of membrane potential. The Generalized Linear Models are able to capture the probalistic properties of spiking data, but don't take bio-physicality into account. The Hodgkin-Huxley model, is the most detailed and biologically accurate model that exist currently. It describes the initiation and propagation of action potentials based on ion channel kinetics. Because it's so detailed, it is also computationally heavy. The Izhikevich model is more efficient and still versatile, capturing various neuronal firing patterns with fewer parameters than the Hodgkin-Huxley model. Finally, the FitzHugh-Nagumo model, a simplified version of the Hodgkin-Huxley model, focuses on the essential features of neuronal excitability and spike generation while being computationally efficient.

These models provide a ”single compartment”, meaning they can be used to simulate a single neuron. To extend the models to simulate multiple neurons we simply run them in parallel (or in series in different applications).

We will now go into the details of each model and evaluate their effectiveness in simulating the spiking behavior of otolith afferents.

The Integrate-and-Fire model, the Generalized Linear Model and the Hodgkin-Huxley model have been fit to vestibular neuron data before:

Integrate and Fire Model

Integrate-and-Fire (I&F) models have a low complexity. These models abstract away many of the detailed biophysical processes that occur in real neurons. Instead of modeling the intricate dynamics of ion channels and other cellular mechanisms, I&F models reduce the problem to the essentials: how the membrane potential changes in response to inputs, and when a spike (action potential) is generated. These can incorporate various mechanisms, such as spike initiation, adaptive excitability, or distinct compartments. These features enable I&F models to generate diverse spiking behaviors and simulate multiple neuron types. I&F models can replicate and predict neuronal activity with high accuracy, often matching the performance of more complex biophysical models with numerous parameters.

This model was used by Jamali et al. [48] to replicate their results. They were able to match their empirical findings for both regular and irregular neurons by adding a noise term to a leaky I&F model. This model should therefore be suited for simulating the otolith spiking data.

Generalized Linear Model

Generalized linear models (GLMs) can be used to map the relationship between sensory inputs and neuronal spiking activity. These methods are valuable for quantifying patterns in the data and benefit from statistically parameter estimation and model selection techniques. GLMs can incorporate noise or uncertainty in afferent data, providing a probabilistic framework that reflects real-world variability.

However, GLMs are inherently statistical models that do not directly incorporate the underlying biophysical mechanisms of neuronal activity. They model the relationship between inputs and outputs using a probabilistic framework but do not account for the ion channel dynamics, membrane potentials, or other cellular processes that drive neuronal firing. Also, GLMs can model the average firing rate over time, but they often struggle to accurately predict precise spike timing, especially in the presence of rapid fluctuations or irregular spiking patterns. The temporal precision of vestibular neurons, may not be well captured by a GLM.
Despite these limitations, the flexibility of GLMs in accommodating different data distributions makes them potentially useful for statistically modeling both regular and irregular responses. This approach could offer valuable high-level insights into the relationship between stimuli and afferent responses.

Hodgkin-Huxley Model

Mechanistic models of neurons, which utilize biophysically interpretable variables and parameters, help in understanding the dynamics of neural circuits. The most detailed of these models are based on the Hodgkin–Huxley (HH) framework. The HH model is computationally intensive due to its detailed representation of ion channel dynamics. Each simulation involves solving multiple coupled differential equations that describe the conductance of sodium, potassium, and leak channels.

The original model was developed to describe the squid giant axon, but it can be adapter to other neurons by adjusting the parameters and adding ion channels. Hight and Kalluri [36] have created a model that emulates the vestibular afferents. This model can produce both regular and irregular firing patterns. However, originally the model is deterministic and therefore might not seem like a good fit for our purpose. However, by sampling from an ESPC distribution as input the model gets stochastic properties. There are more stochastic methods that can be used [33][8][3], but to not add more complexity we will not consider them for now.

Studies comparing these detailed models with actual spike train recordings have shown that various sets of biophysical parameters can produce identical firing patterns. This can make it quite difficult to infer which parameters to change to create the right behaviour. Creating one model to cover the different firing patterns of both regular and irregular neurons is therefore challenging. Also, while the detailed mechanistic focus of the HH model is valuable for understanding specific ionic processes, it can be overly detailed for some applications, such as studying the overall functional properties of vestibular neurons in a broader network context. As this model has been used by other to replicate vestibular spiking data, we shall explore if this is also applicable to the otoliths specifically.

For the following models reliable replications did not exist, however they are still considered on the ground that they should be less computationally expensive, while still providing extensive spiking patterns:

Izhikevich Model

The Izhikevich model [44] is a mathematical framework introduced by Eugene Izhikevich as a simpler alternative to more complex models like the Hodgkin-Huxley model, while still being able to capture a wide variety of spiking and bursting patterns observed in real neurons. The Izhikevich model is based on two differential equations and five parameters, making it computationally efficient and easier to implement than models with many variables, such as the Hodgkin-Huxley model.

The model is defined by the following two differential equations [44]:

$$\frac{dv}{dt} = 0.04v^2 + 5v + 140 - u + I_{\text{ext}}, \tag{5.1}$$

$$\frac{du}{dt} = a(bv - u), \tag{5.2}$$

where:

- v represents the membrane potential of the neuron.
- u is the recovery variable, which accounts for the activation of K^+ ion channels and the inactivation of Na^+ ion channels.

- I_{ext} is the external input current.
- a, b, c, and d are parameters that can be adjusted to simulate different types of neuronal behavior.

The model also includes a reset mechanism to handle the spiking behavior:

$$\text{if } v \geq 30 \text{ mV, then } \begin{cases} v \leftarrow c, \\ u \leftarrow u + d. \end{cases}$$

The parameters a, b, c, and d have specific roles:

- a determines the time scale of the recovery variable u. Typical values range around 0.02.
- b controls the sensitivity of the recovery variable u to the membrane potential v. Typical values are around 0.2.
- c is the reset value of the membrane potential v after a spike. It usually takes a value of about -65 mV.
- d describes the reset increment of the recovery variable u after a spike, typically around 8.

The range of spiking patterns that can be simulated is extensive; however, initial investigations suggest that replicating the distinct irregular firing patterns of otolith afferents may be challenging. As can be seen in Figure 5.2 the firing patterns that emerge from the model are ”bursting phasic” patterns which are repeating in a regular pattern. Different combinations of parameters couldn’t simulate irregular behaviour either. Therefore, the conclusion has been made that the Izhikevich model is suitable for regular otolith afferents, but in its standard form not for irregular ones.

FitzHugh-Nagumo Model

The FitzHugh-Nagumo (FHN) model is a simplified mathematical model, specifically designed to capture the essential features of excitability and spike generation. It is a reduction of the more complex Hodgkin-Huxley model and focuses on the core dynamics of action potentials. It is useful for studying general principles of neuronal behavior without delving into the full biophysical complexity. The FitzHugh-Nagumo model reduces the four-dimensional Hodgkin-Huxley model to a two-dimensional system of differential equations. This makes it simpler and more computationally efficient, while still retaining the essential qualitative features of excitability and spiking.

The FitzHugh-Nagumo model abstracts away much of the biophysical complexity present in real neurons. Vestibular neurons, especially those in the vestibular nuclei, exhibit complex behaviors that are influenced by a variety of ion channels [51], synaptic inputs, and intrinsic membrane properties that the FitzHugh-Nagumo model does not fully capture. This simplification means the model may not accurately represent the precise dynamics of vestibular neurons, particularly the differences between regular and irregular spiking patterns, which are influenced by specific ion channel dynamics [36] and synaptic mechanisms [17].

$$\frac{dv}{dt} = v - \frac{v^3}{3} - w + I_{\text{ext}}, \tag{5.3}$$

$$\frac{dw}{dt} = \epsilon(v + a - bw), \tag{5.4}$$

where:

- v represents the membrane potential.
- w is the recovery variable, analogous to ion channel dynamics in the Hodgkin-Huxley model.
- I_{ext} is the external input current or stimulus.
- ϵ, a, and b are parameters that determine the behavior of the model, such as excitability and the speed of the recovery process.

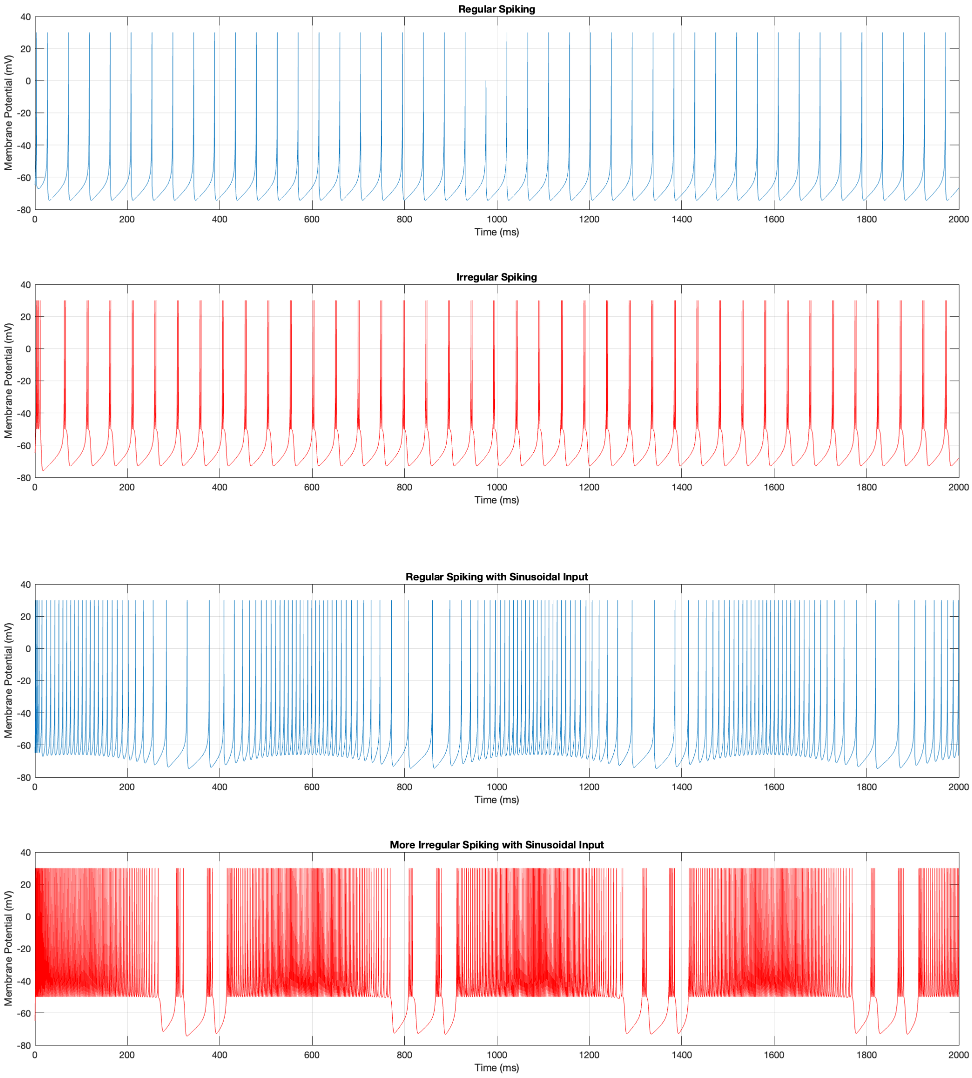

Figure 5.2: Izhikevich model simulation of continuous spiking and spiking in response to a sinusoidal input of 2Hz, simulating regular and irregular neurons.

In this form, the FHN model thus consists of two coupled, nonlinear ordinary differential equations, where the first one describes the fast evolution of the membrane voltage of a neuron (v), while the second one represents the slow recovery through the opening of potassium channels and the inactivation of sodium channels (w).

The FitzHugh-Nagumo model generally uses deterministic equations, with noise often added as an external factor rather than an intrinsic property of the axon model. Vestibular neurons, particularly irregular neurons, are known to exhibit stochastic behavior. The model's inability to intrinsically represent stochastic firing may limit its usefulness in studying the role of irregular spiking in vestibular signal processing. Another downside is that the FHN does not support phasic spiking and bursting, which does occur in the otolith afferents.

Conclusion

Previous research [44] has demonstrated the wide range of firing patterns that the HH model can reproduce, highlighting its versatility. However, this model also demands significant computational resources, as illustrated in Table 5.2. In contrast, while the IF model cannot replicate the full spectrum of neural

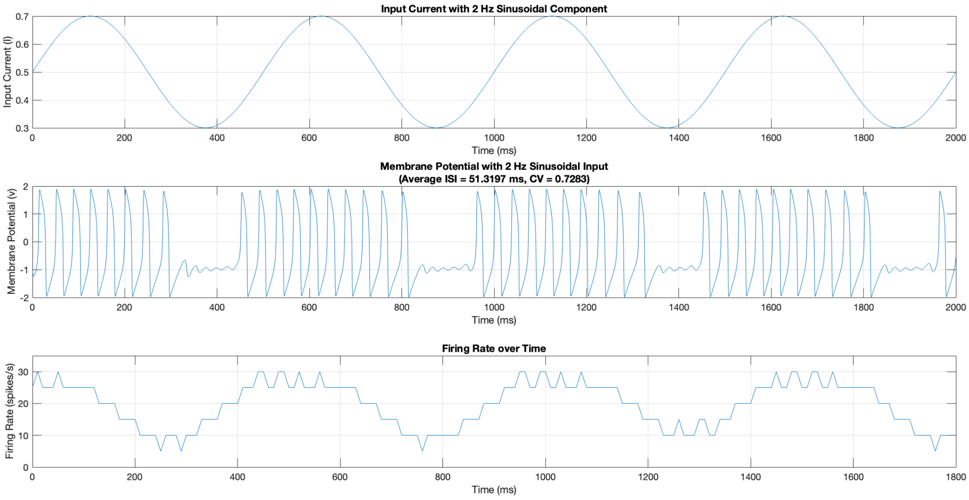

Figure 5.3: FHN model simulation of spiking in response to a sinusoidal input of 2Hz.

5.1

Models	biophysically meaningful	tonic spiking	phasic spiking	tonic bursting	phasic bursting	mixed mode	spike freq. adaptation	class 1 excitable	class 2 excitable	spike latency	subthreshold oscillations	resonator	integrator	rebound spike	rebound burst	threshold variability	bistability	DAP	accommodation	inhibition-induced spiking	inhibition-induced bursting	# of FLOPS
Integrate-and-fire	-	+	-	-	-	-	-	+	-	-	-	+	+	-	-	-	-	-	-	-	-	5
Quadratic integrate-and-fire	-	+	-	-	-	-	-	+	+	+	-	+	-	-	-	-	-	-	-	-	-	7
Izhikevich (2003)	-	+	+	+	+	+	+	+	+	+	+	+	+	+	+	+	+	+	+	+	+	13
FitzHugh-Nagumo	-	+	-	-	-	-	-	+	+	+	+	+	-	+	+	+	+	-	-	-	-	72
Hodgkin-Huxley	+	+	+	+	+	+	+	+	+	+	+	+	+	+	+	+	+	+	+	+	+	1200

Table 5.1: Comparison of neuron models with respect to their features and computational cost (FLOPS). Table adapted from [44]

firing behaviors, it has been shown to effectively simulate the spiking patterns of otolith afferents [85]. Additionally, GLMs serve as fundamental statistical frameworks, offering a straightforward approach to capturing the statistical properties of afferent spiking.

Considering the strengths and limitations of these models, the Integrate-and-Fire model, Generalized Linear Model, and Hodgkin-Huxley model have been selected to simulate the spiking behavior of otolith afferents. This combination strikes a balance between computational efficiency and biophysical accuracy, providing a comprehensive framework for studying both regular and irregular spiking behaviors.

The models will follow a structure like is shown in Figure 5.4. We will model two variants for each model type: the regular and irregular afferent.

We will start by looking at the Integrate-and-Fire model, then we will look at the Hodgkin-Huxley model, and finally the Generalized Linear Model is considered. The main objective is to create a model that is able to encode the stimulus into a spike train with statistic properties that resemble the regular and irregular otolith afferents.

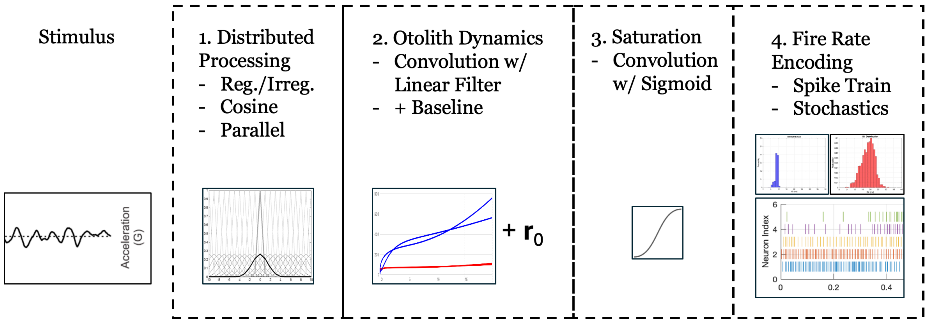

Figure 5.4: Overview of the spike rate encoding pipeline.

5.3. Integrate-and-Fire Model

To model the Integrate-and-Fire model: we will first define the input for the model (including linear and nonlinear transfer functions), then set the stochastic properties of the model, and finally we will tune and validate the model with the otolith afferent spiking data data from Jamali (2019) [48].

The I&F model abstracts the complex biophysical processes underlying action potential generation into a straightforward mathematical form. While it does not aim to replicate the exact mechanisms involved in spike generation, it captures the idea that neurons integrate inputs over time and fire when a certain threshold is reached. This simplification allows us to focus on understanding how neurons process information and interact within networks without delving into the complexities of ionic currents and membrane conductances.

The I&F model represents a neuron as a simple electrical circuit composed of a capacitor (representing the neuron's membrane) and a resistor (representing the membrane's leakage channels). The capacitor stores charge, and the voltage across it represents the membrane potential $V(t)$. Incoming synaptic inputs or external currents are represented as an input current $I(t)$ that charges the capacitor, leading to changes in the membrane potential. For our model, we will use the Leaky Integrate-and-Fire (LIF) model, which includes a leak term that reflects the diffusion of ions through the axon's membrane.

5.3.1. Principles and mathematical formulation

The model operates under the following basic principles:

1. Integration: The neuron integrates the incoming current over time, causing the membrane potential $V(t)$ to increase or decrease depending on the nature of the input. This process is described by a differential equation that governs the rate of change of the membrane potential.
2. Leakage: In the leaky version of the model, the membrane potential naturally decays towards a resting value in the absence of input due to the leakage of charge through the membrane's resistive channels. This leakage is a crucial feature, as it prevents the membrane potential from increasing indefinitely in response to continuous input.
3. Threshold and firing: When the membrane potential reaches a predefined threshold V_{th}, the neuron fires an action potential. In the I&F model, this firing event is represented as a simple threshold-crossing event, without explicitly modeling the spike's shape.
4. Reset and refractory period: After firing, the membrane potential is reset to a lower value, often called the reset potential V_{reset}, and the neuron may enter a refractory period during which it cannot fire again. This reset mechanism ensures that the neuron does not fire repeatedly due to a single input.

The output we are trying to simulate is the membrane potential $V(t)$. In the I&F model it is governed by the following equation:

$$C_m \frac{dV(t)}{dt} = -\frac{V(t)}{R_m} + I(t \tag{5.5}$$

where:

- C_m is the membrane capacitance, representing the ability of the membrane to store charge.
- R_m is the membrane resistance, representing the leakage channels in the membrane.
- $I(t)$ is the external input current, representing the sum of synaptic input or injected current.

The term $-\frac{V(t)}{R_m}$ accounts for the leakage of charge, causing the membrane potential to decay towards a resting value over time. The input current $I(t)$ can be time-varying and may include contributions from multiple synaptic inputs, or hair cell EPSCs and galvanic vestibular stimulation, as is typical for some vestibular experiments.

When the membrane potential reaches the threshold V_{th}, the model triggers a spike, and the membrane potential is reset according to the following rule:

$$\text{If } V(t) \geq V_{th}, \text{ then } V(t) \rightarrow V_{reset} \tag{5.6}$$

5.3.2. Input generation

The otolith haircells and afferents encode linear accelerations, which we will use as input to the LIF model. The input current $I(t)$ to the LIF model should be a time-varying signal that represents the encoded sensory information.

If modeling otolith organ afferents, the input might be proportional to the linear acceleration experienced by the head:

$$I(t) = k \cdot a(t) \tag{5.7}$$

Vestibular afferents are known to exhibit a certain level of variability in their responses, which can be modeled by adding noise to the input current. This can simulate the natural stochastic variability in sensory encoding. A common approach is to add Gaussian white noise:

$$I(t) = k \cdot a(t) + \sigma \cdot \eta(t) \tag{5.8}$$

where $\eta(t)$ is a Gaussian white noise process with zero mean and standard deviation σ.

Vestibular afferents have a baseline firing rate even in the absence of head movements. This can be modeled by adding a constant current to the LIF model:

$$I(t) = I_{baseline} + k \cdot a(t) + \sigma \cdot \eta(t) \tag{5.9}$$

where $I_{baseline}$ is a constant current that maintains the neuron's baseline activity. This is a tuneable parameter that we will match later to the otolith data.

Otolith inputs can vary dynamically depending on the nature of the head movement. For instance, vertical movement of a boat might represent a periodic head acceleration:

$$a(t) = a_0 \cdot \sin(2\pi f t) \tag{5.10}$$

where a_0 is the amplitude and f is the frequency of the head movement. This would result in an input current:

$$I(t) = I_{baseline} + k \cdot a_0 \cdot \sin(2\pi f t) + \sigma \cdot \eta(t) \tag{5.11}$$

However, we know the relationship between input, head movements, and output, spike trains, is more complex than what can be captured by a simple static linear factor k [85]. We will go into how to model this relationship in the next section.

5.3.3. Model input: vestibular response functions

There are previously published models of peripheral vestibular processing, which have demonstrated an accurate reproduction of the responses of peripheral otolith afferents to artificial stimuli [32]. One that is formulated based on empirical data is the response function by Angelaki et al. [1], which is defined as follows:

$$H_{\text{otolith}}(f) = k\frac{S^{k_1}(1+aS)^{k_2}}{1+bS} \tag{5.12}$$

The parameters used in the equations for regular and irregular afferents are derived from experiments done in [45] and listed in Table 5.2.

Parameter	Regular otolith afferents	Irregular otolith afferents	Description
k	59.0106 (spikes/s)/G	112.7417 (spikes/s)/G	Gain
k_1	0.0643	0.3084	Exponent for S
k_2	2.208	2.6834	Exponent for $(1 + aS)$
a	0.0138 s	0.0136 s	Time constant for $(1 + aS)$
b	0.0255 s	0.0318 s	Time constant for $(1 + bS)$

Table 5.2: Parameters for transfer functions of regular and irregular afferents, from [85].

Since the transfer function is fractional, it lacks a straightforward physical interpretation. The purpose of the function described by Angelaki et al. was not to define specific temporal filtering parameters, which are characteristics like cutoff frequency or time constant that describe how the system might filter different components of a signal over time. For this, the neurons are too multidimensional and not enough is known to describe this fully. However, it does help us with giving us a relatively simple model to encode the expected rate from both regular and irregular afferents.

The model can be used to multiply the input stimuli in the frequency domain. In the frequency domain, the signal's time-related information, such as when specific events occur, is lost. This can make it difficult to analyze or manipulate signals that have important time-domain characteristics, such as transients or specific timing events. Since we assume rate encoding, we are mostly interested in the gain and phase characteristics. Those are kept in the frequency domain.
Transforming the stimulus into a spike rate is done by converting the time domain signal $x(t)$ into its frequency domain representation $X(f)$ using the fast Fourier transform (FFT). A transfer function $H(f)$ is then applied to modify the signal in the frequency domain, resulting in $Y(f) = H(f) \cdot X(f)$. The modified signal is transformed back to the time domain using the Inverse FFT, giving the output signal $y(t) = \text{IFFT}(Y(f))$. We will use this output signal to encode the spike rate into individual spikes using a spike encoding model like the Leaky Integrate-and-Fire model.

When you perform a Fourier transform on a finite-length signal, the implicit assumption is that the signal is periodic. If the signal does not naturally begin and end at the same value, discontinuities at the boundaries can introduce artificial high-frequency components into the spectrum. This phenomenon is known as spectral leakage. The Hanning window is a type of window function used in signal processing to reduce the spectral leakage that occurs when performing a Fourier transform on a finite-length signal. The Hanning window is applied to a signal before performing the Fourier transform to smooth the edges of the signal. By tapering the signal to zero at the boundaries, the Hanning window reduces the discontinuities, which in turn minimizes spectral leakage.

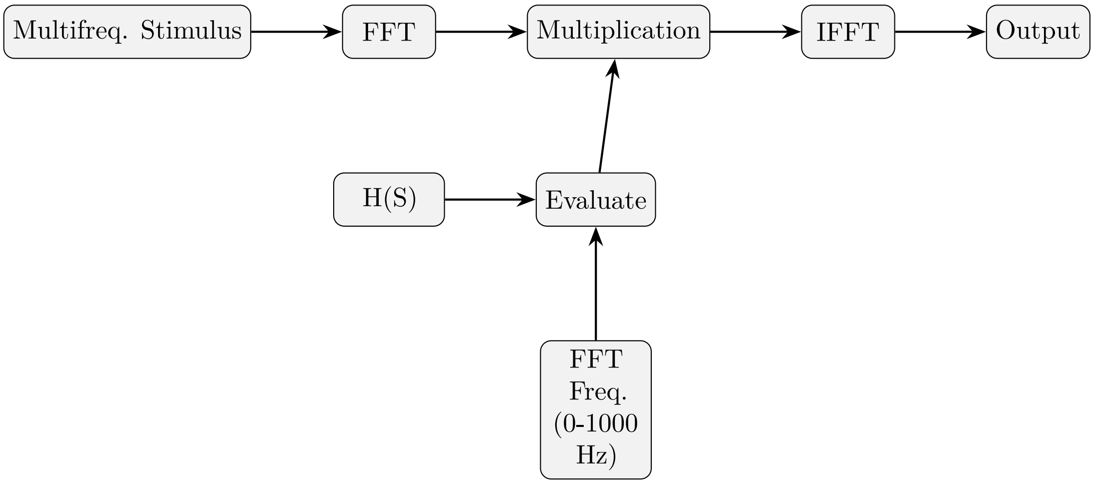

Angelaki's transfer function is designed to model the behavior of vestibular afferents for specific types of stimuli, particularly sinusoidal inputs. While it effectively captures the steady-state response, it may not fully reflect how the system responds to sudden changes or non-sinusoidal signals. This makes the transfer function very useful for certain experimental conditions, but it might need adjustments for different types of signals. Furthermore, since it is based on specific experiments, it might not be as accurate if used in other contexts without modifications. In the frequency domain, the time-related information of the signal, such as when specific events occur, is lost. This can make it difficult to analyze or manipulate signals that have important time-domain characteristics, such as transients or specific timing events.

The original transfer function is a fractional transfer function. We will fit integer-order transfer functions because they are simpler to analyze, simulate, and implement compared to fractional-order models. Integer-order systems are widely supported by standard control theory and signal processing tools, which makes it easier to design, optimize, and ensure the stability of systems. Additionally, integer-order models are computationally more efficient and are compatible with a wide range of existing software and hardware platforms. By fitting integer-order transfer functions, we can approximate the behavior of more complex systems while maintaining the practical benefits of simplicity and robustness.

Since we don't have access to the original data, we need to fit the function to the function from Schneider et al.[85].
We performed a brute force optimization. We can fit the fractional transfer function using Linear System Identification techniques. The fitting was performed in the frequency domain matching gain and phase from 0:20 Hz with a frequency resolution of x Hz. After selecting the model order, we found the best-fit transfer function that matched the given frequency response by iterating through different numerator and denominator orders. We used Matlab's invfreqs function to fit a transfer function to the frequency response data, calculating errors in both magnitude and phase. The best transfer function was selected based on error values and comparing Bode plots. The optimal results were obtained with a 9th-order transfer function for the irregular case and an 8th-order function for the regular case, see Equation 5.13 with parameters specified in Table 5.3. For very low frequencies, less than 0.2Hz, the matched transfer function deviates from the response of Angelaki's function. Looking at the matched responses, we can argue that these are actually more realistic since the magnitude for 0 Hz is not 0 spikes/s/G. Instead, it is a value of 75 spikes/s/G and 45 spikes/s/G for the irregular and regular afferents, respectively. This is more realistic because the afferents are also sensitive to static gravitational force. This is closely aligned with the static values reported by [26], which indicated a sensitivity of 58 spikes/s/G for irregular afferents and 34 spikes/s/G for regular afferents. Given that our resting discharge is slightly higher than the values measured in their study, and considering that sensitivity tends to increase with resting discharge, we can conclude that our results provide a reasonable estimate.

$$H(s) = \frac{N(s)}{D(s)} \tag{5.13}$$

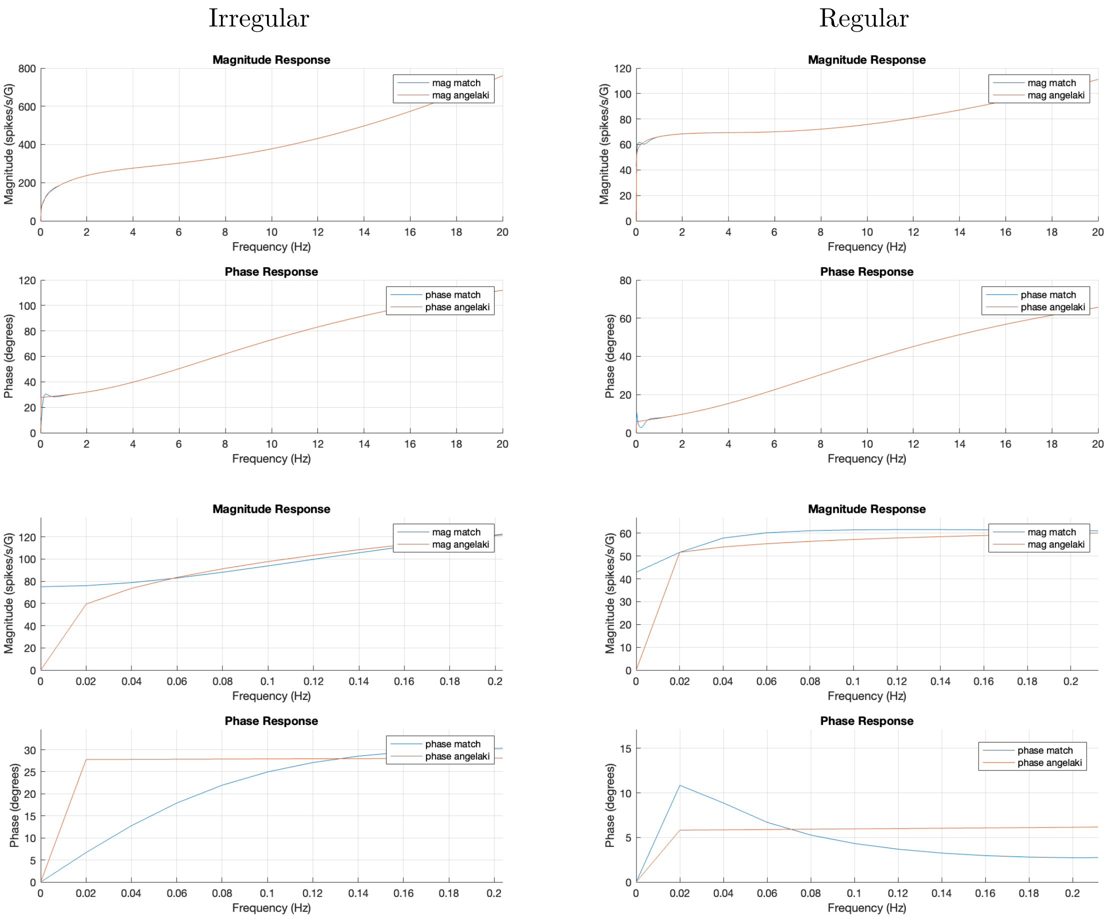

Figure 5.5: Comparison between the frequency response function by Angelaki [1] and the matched transfer function, for 0-20 Hz (top) and zoomed in to below 0.2 Hz (bottom). At high frequencies there is a good match, but below 0.2Hz the original and matched functions start to deviate.

where:

$$N(s) = As^9 + Bs^8 + Cs^7 + Ds^6 + Es^5 + Fs^4 + Gs^3 + Hs^2 + Is + J \tag{5.14}$$

$$D(s) = Ks^9 + Ls^8 + Ms^7 + Ns^6 + Os^5 + Ps^4 + Qs^3 + Rs^2 + Ss + T \tag{5.15}$$

	Regular		Irregular	
	Numerator Coeff.	Denominator Coeff.	Numerator Coeff.	Denominator Coeff.
s^9	$A = -1.255 \times 10^7$	$K = 1$		
s^8	$B = -7.006 \times 10^9$	$L = -3332$	-9313	1
s^7	$C = -1.227 \times 10^{12}$	$M = -3.822 \times 10^8$	-6.751×10^6	-6288
s^6	$D = -9.514 \times 10^{13}$	$N = -1.476 \times 10^{11}$	-1.458×10^9	-6.413×10^6
s^5	$E = -3.494 \times 10^{15}$	$O = -9.517 \times 10^{12}$	-1.264×10^{11}	-1.266×10^9
s^4	$F = -5.878 \times 10^{16}$	$P = -2.216 \times 10^{14}$	-4.499×10^{12}	-5.872×10^{10}
s^3	$G = -4.915 \times 10^{17}$	$Q = -2.396 \times 10^{15}$	-4.931×10^{13}	-7.329×10^{11}
s^2	$H = -1.448 \times 10^{18}$	$R = -1.102 \times 10^{16}$	-1.453×10^{14}	-2.353×10^{12}
s^1	$I = 1.247 \times 10^{18}$	$S = -1.22 \times 10^{15}$	-2.506×10^{14}	-4.099×10^{12}
s^0	$J = 1.42 \times 10^{18}$	$T = 1.892 \times 10^{16}$	-2.526×10^{13}	-5.887×10^{11}

Table 5.3: Coefficients of the 8th/9th order transfer functions.

Although using a high-order model can improve the fit, it can also lead to overfitting. The model becomes too finely tuned to the specific data used for matching and fails to generalize well to other conditions. Overfitting can result in a model that captures noise or irrelevant dynamics rather than the true underlying behavior of the system. By lowering the order, we lose accuracy in the replication of the frequency and phase response, but gain a transfer function that is less complex and possibly less overfitted.

Using a second-order transfer function gives us the following function and responses:

$$H(s) = \frac{a_0 + a_1 s + a_2 s^2}{1 + b_1 s + b_2 s^2}$$

The coefficients are given in Table 5.4, while the results are plotted in Figure 5.6.

Term	Order	Regular	Irregular
Numerator Coefficient	s^2	$a_2 = 0.1520$	$a_2 = 0.2117$
Numerator Coefficient	s^1	$a_1 = 19.4263$	$a_1 = 18.4364$
Numerator Coefficient	s^0	$a_0 = 55.9154$	$a_0 = 95.4884$
Denominator Coefficient	s^1	$b_1 = 0.2686$	$b_1 = 0.0609$
Denominator Coefficient	s^2	$b_2 = -0.00000598$	$b_2 = -0.00000102$

Table 5.4: Coefficients of the 2nd order transfer function for regular and irregular afferents.

Now we can evaluate the different functions. In order to do this, we have created an arbitrary multi-frequency stimuli. We'll transform the signal using all 6 transfer functions and compare the results.

The input signal is generated as the sum of multiple sinusoids with different frequencies, amplitudes, and phases. The frequencies are set at 2, 5, 10, and 19 Hz, with corresponding amplitudes of 1, 0.5, 0.8, and 0.6, respectively. The phases of each sinusoid are set to 0, $\frac{\pi}{4}$, $\frac{\pi}{2}$, and $\frac{3\pi}{4}$ radians. The total input signal, $x(t)$, is constructed by summing these individual sinusoidal components as follows:

$$x(t) = \sum_{i=1}^{4} A_i \sin(2\pi f_i t + \phi_i) \tag{5.16}$$

where A_i, f_i, and ϕ_i represent the amplitude, frequency, and phase of the i-th sinusoidal component.

The result can be seen in Figure 5.7. The responses look very similar, which might mean that we can use the simplest function further on in the model.

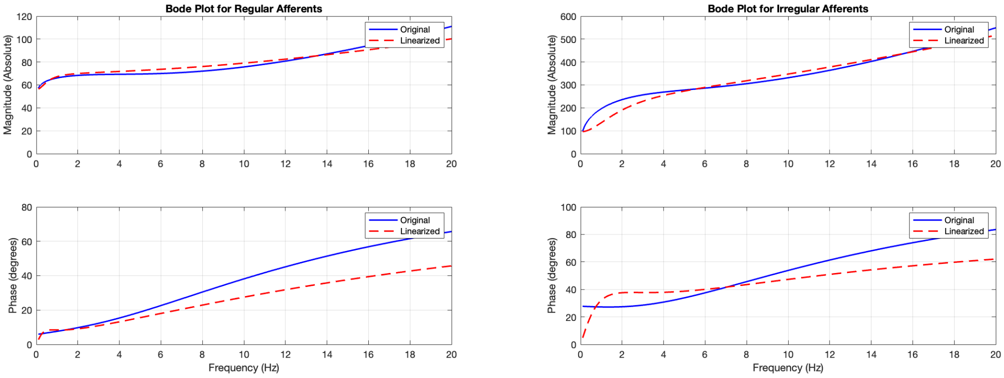

Figure 5.6: Frequency responses of the 2nd order transfer functions of the regular and irregular otolith afferents

When we measure the error between the original function and the 2nd and 8th/9th order functions, as expected, we see in Figure 5.8 that the error is lower for the higher order functions.

We used the higher-order integer transfer function in further modelling because it is expected to provide the highest accuracy and is also valid for static sensitivity. However, if computation time becomes a concern or if we need to implement control models, we can switch to the second-order model.

5.3.4. Non-Linear addition

We need to take into account two things. Most vestibular neurons have a baseline firing rate, and the spike rate of neurons cannot be negative. In order to model the baseline firing rate we can add r_0. The output firing rate $r(t)$ in response to stimulus $s(t)$ is then given by:

$$r(t) = (H * s)(t) + r_0,$$

where the asterisk denotes a convolution with a filter $H(t)$ and r_0 is the baseline firing rate in the absence of stimulation. For otolith afferents, $r_0 = 79$ Hz is used. This reflects the average baseline firing rates observed experimentally [84, 45].

When using this method to predict the firing rate for higher-amplitude stimuli, negative firing rates are predicted, especially for the more sensitive irregular neurons. This is not physiologically possible. To address this limitation, a nonlinear component is introduced, forming a linear–nonlinear (LN) cascade model [12].

The nonlinear component is a Gauss error function (erf) that "squeezes" the linear prediction between 0 and +- 280 spikes/s. This means that for predicted spike rates that are either negative or very high, the spike rate is brought back to a biologically realistic spike rate. As found by Schneider et al.[85] this matches the response of individual regular and irregular otolith afferents quite well. When requesting the original dataset, both Schneider and Jamali no longer had access to it. Thus, we will visually match the parameters of the erf function, using Figure 5.9 as a reference. This was confirmed by Schneider as a suitable approach that should give accurate results.

The erf function is defined as follows:

$$\text{erf} = \frac{c_3}{2}\left(1 + \text{erf}\left(\frac{x - c_2}{\sqrt{2c_1}}\right)\right) \tag{5.17}$$

where the to be identified parameters are $c1$, $c2$ and $c3$.

After making a first approximation, we plot the function in Matlab and use interactive sliders to tune the parameters, as can be seen in Figure 5.10. The final parameters $c1$, $c2$ and $c3$ are 10,000, 140, and 290, respectively.

Processing the transformed signal with the sigmoid erf function creates a response that should also be valid for high frequency and high amplitude signals. In Figure 5.11 we see the difference in response

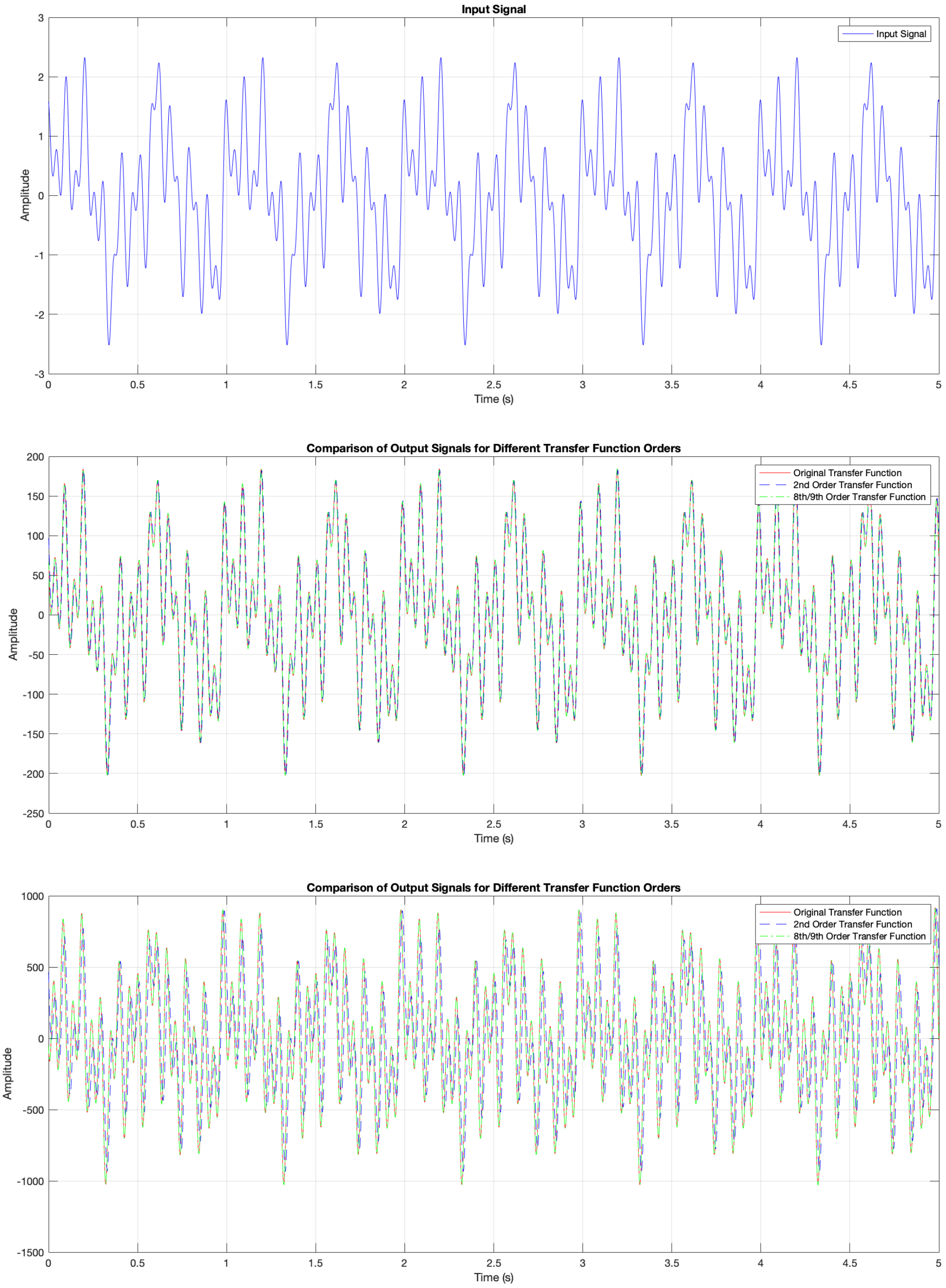

Figure 5.7: Multi-frequency input signal and it’s transformation into firing rate.

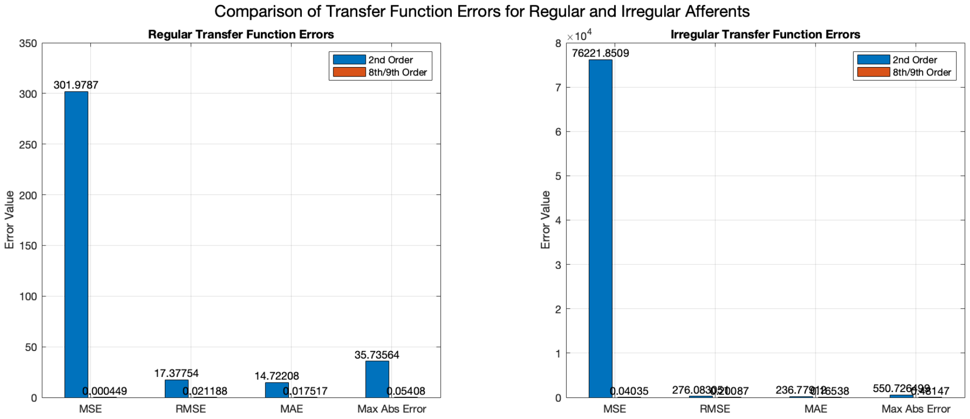

Figure 5.8: MSE, RMSE, MAE and Max Absolute Error for each function compared to the original fractional function. The higher-order models clearly have a lower error.

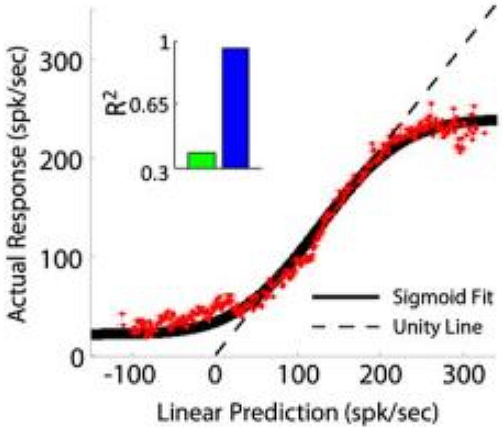

Figure 5.9: The relationship between the linear and actual response for otolith afferents, both regular and irregular, as discussed with Schneider. The key factors are the unit slope of the response and the saturation of the firing rate around ±300 spikes/s. Figure from [85]

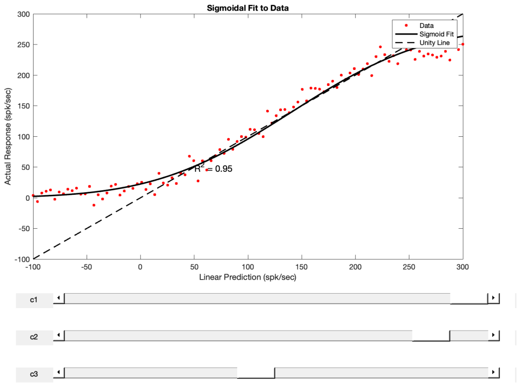

Figure 5.10: Tuning C1, C2, and C3 parameters to match the non-linear part of the Cascaded LN model to the results from [85]. The red data dots are exemplary since no research data was available. Values are: C1: 10000, C2: 140, C3: 290.

between high and low amplitude stimuli for both regular and irregular otolith afferents. Note the difference between the linear and nonlinear prediction.

We now have an accurate firing rate prediction, which can serve as the input for neuron spiking models. These models will encode the firing rate into a spike train, following the associated distribution.

5.3.5. Assumptions and modifications to Leaky Integrate and Fire model

We will now set up the complete integrate and fire model and use the input that we have just defined. Let us start with how the membrane voltage is updated.

Reset voltage.

Originally, in [46], the reset voltage in the LIF model was set to 0 mV and the threshold is -50 mV. This means that the neuron would immediately spike again as soon as it resets to 0 mV, because 0 mV is greater than the threshold of -50 mV. This would lead to continuous spiking, which is not the desired behavior for a typical integrate-and-fire model. To prevent continuous spiking, the reset voltage should be set below the threshold voltage. This ensures that after a spike, the membrane potential is reset to a value that requires the neuron to integrate a new input before reaching the threshold again. In a more

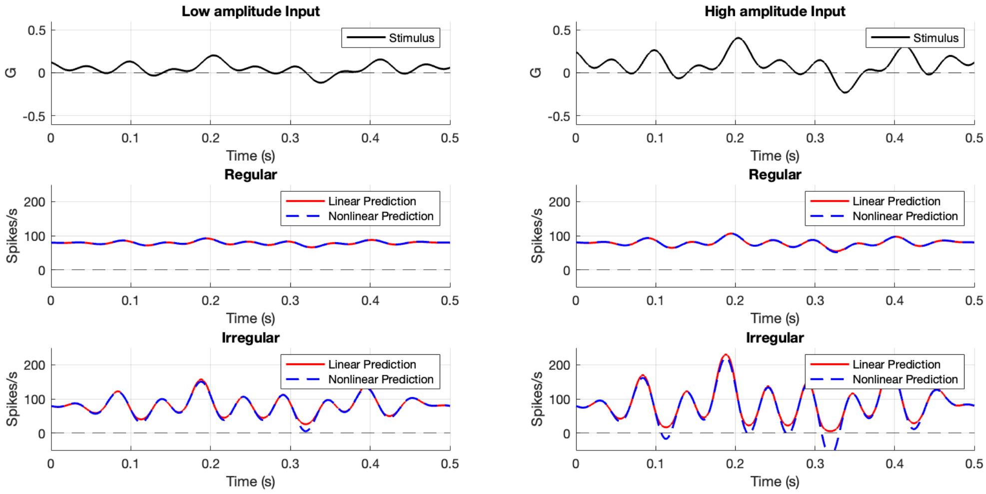

Figure 5.11: Implementing the Linear NonLinear Model.

realistic scenario, the reset voltage V_{rest} is often set to a value slightly below the resting potential, e.g., -65 mV, to account for the refractory period. This is what we applied.

Leak term.
In the Leaky Integrate-and-Fire model, the term $-g \cdot (V(t-1) - V_{\text{rest}})$ represents the leak current. The leak current tends to drive the membrane potential V back towards the resting potential V_{rest}. This is a common feature in many neuron models to simulate the effect of ion channels that work to maintain the resting potential.

The term $-g \cdot (V - V_{\text{rest}})$ describes the passive leakage of ions across the membrane, which drives the membrane potential V towards the resting potential V_{rest}.

- If V is above V_{rest}, the term $-g \cdot (V - V_{\text{rest}})$ will be negative, pulling V down.
- If V is below V_{rest}, the term $-g \cdot (V - V_{\text{rest}})$ will be positive, pushing V higher.

Summary.
With $S_t(t)$ defined by the transfer functions previously, the leak term established and the reset potential assumed to be -65 mV, a noise term was added to account for the inherent noise or variance in the otolith afferents. The noise term ξ is a Gaussian white noise process with zero mean and standard deviation σ_{noise}. To account for the difference in sensitivity between the regular and irregular a noisy sensitivity term is multiplied with the input signal $S_t(t)$, σ_{signal}.

The update rule for the membrane potential considering all currents can be expressed as:

$$V(t) = V(t-1) + \left(\frac{-g \cdot (V(t-1) - V_{\text{rest}}) + I_{\text{bias}} + S_t(t)\sigma_{\text{signal}} + \xi(t)\sigma_{\text{noise}}}{C_m} \right) \cdot dt$$

where membrane capacitance $C_m = 1\,\text{nF}$, membrane conductance $g = 0.22\,\mu\text{S}$, and $I_bias = 3.53nA$

5.3.6. Validating model with Jamali (2019) CV* results

To validate the correct implementation of our model, we can compare it to the results of Jamali (2019) [48]. By tuning I_{bias}, σ_{noise} and σ_{signal}, the static data can be replicated as shown in Figure 5.12. We co-varied σ_{noise} and σ_{signal} to ensure that their ratio remains unity, which corresponds to Jamali et al.'s approach and to measurements on the relation of sensitivity and variability done by Fernandez et al.[26].

The input to the model is a broadband noise current, which is low-pass-filtered white noise. A second-order Butterworth filter with a cut-off frequency of 15Hz is applied. This simulates a multi-frequent input signal. As can be seen in Figure 5.12 our results resemble the results of [48]. The

Variable	Value	Description
C_m	1 nF	Membrane capacitance
g	0.22 µS	Leak conductance, inverse of membrane resistance: $\frac{1}{R_m}$
I_{bias}	3.53 nA	Bias current, increasing I_{bias} increases firing rate, lowers ISI
$\sigma_{\text{noise, Regular}}$	0.68 nA	Standard deviation of noise (Regular)
$\sigma_{\text{signal, Regular}}$	0.68 nA	Standard deviation of signal (Regular)
$\sigma_{\text{noise, Irregular}}$	8.8 nA	Standard deviation of noise (Irregular)
$\sigma_{\text{signal, Irregular}}$	8.8 nA	Standard deviation of signal (Irregular)
dt	0.025 ms	Time step
T	1000 ms	Total simulation time

Table 5.5: List of model variables and their descriptions

parameters for σs were mentioned as $\sigma_{\text{Regular}} = 0.14$ and $\sigma_{\text{Irregular}} = 1.9$, however, in the figure we can see marked by the blue and red dot, that the values for the regular and irregular noise should be ±1.3 and 17 respectively. Our estimates are in-between these two sets of values, so we assume the approach is correct and the model is correctly implemented.

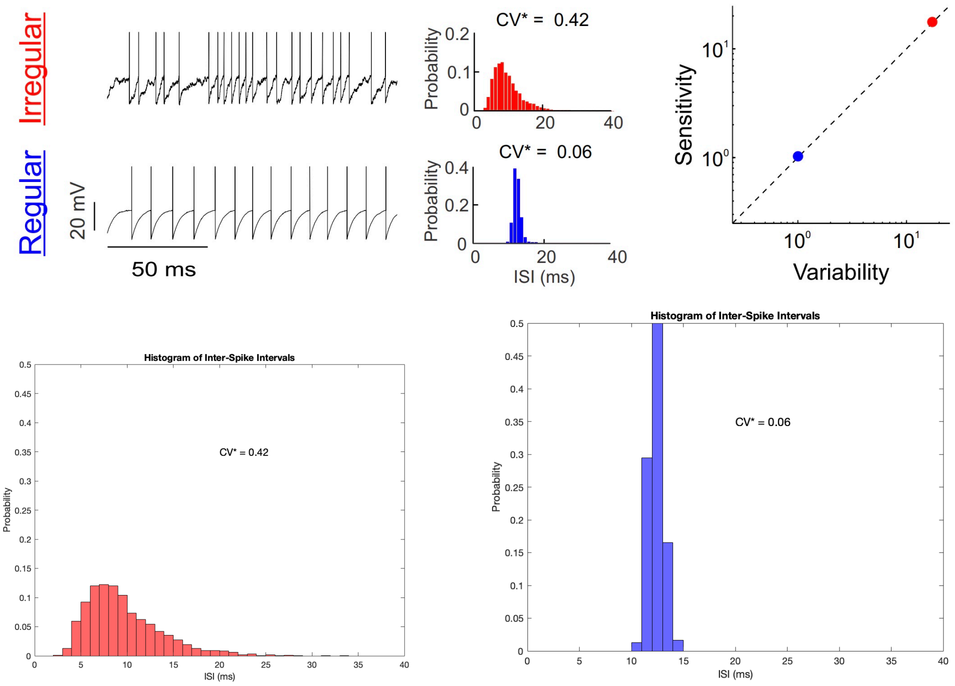

Figure 5.12: Validating the model by replicating Figure 4A from [48]. The paradigm simulated here is the resting discharge from the afferents. The CV* is calculated as the standard deviation of the interspike-intervals (ISIs) divided by the mean of the ISIs at 80 spikes/s. The interspikes intervals are binned in 1ms bins and counted. The narrow distribution of the regular afferent's distribution indicates high precision.
Top: Original Jamali result. Bottom left: Irregular, Bottom right: Regular

5.3.7. Validating: Discrimination performance

The regular and irregular afferent models are defined, and we know they have the correct ISI distributions. To confirm our hypothesis that the irregular afferents transmit information at high frequencies and the regular afferents at low frequencies we need to measure their performance at these frequencies. A way to do this is to measure the Van Rossum distance at different timescales.

Based on the discrimination performance seen in Figure 5.14 we can argue that the regular afferents are better in discriminating low frequencies, while the irregular afferents perform better higher frequencies.

Let us explain this. The Van Rossum distance is a metric used to quantify the difference between two spike trains. This distance measure is particularly useful when comparing the temporal patterns of neural activity across different conditions or experiments.

The Van Rossum distance is defined as the integral of the squared difference between two functions over time. Mathematically, for two spike trains $S_1(t)$ and $S_2(t)$, the Van Rossum distance D can be expressed as:

$$D = \frac{1}{2\tau} \int_{-\infty}^{\infty} \left[(S_1(t) * h_\tau(t)) - (S_2(t) * h_\tau(t))\right]^2 dt \tag{5.18}$$

where $h_\tau(t) = \exp(-t/\tau)$ is the exponential kernel.

The value of τ in the van Rossum distance metric determines the temporal resolution at which spike trains are compared, influencing discrimination performance at different frequencies. A small τ emphasizes precise spike timing, making it effective for discriminating high-frequency signals where exact timing is crucial. Conversely, a large τ smooths timing differences, focusing on overall firing rates, which improves performance for low-frequency signals where timing precision is less critical. As τ increases, discrimination performance typically decreases for high-frequency stimuli but may improve for low-frequency stimuli. Thus, the optimal τ depends on the frequency content of the stimulus: low τ for high-frequency precision and high τ for rate-based discrimination. Experimenting with different τ values allows for analyzing how temporal resolution affects the ability to distinguish between different stimuli. This means the value of τ modulates the balance between spike-timing precision and rate coding.

Jamali et al. [48] predicted that if information is transmitted through precise spike timing, discrimination performance would peak at timescales shorter than those of the stimulus (for 15Hz low-pass filtered stimulus: <50 ms). Our findings confirmed this, showing that irregular afferents achieved maximum discrimination at around 10 ms. In contrast, regular afferents exhibited much lower discrimination performance, with a peak at a longer timescale of 37 ms, which is closer to the timescales present in the stimulus.

This result means that the LIF model can potentially embed the precise spike timing and rate encoding characteristics from regular and irregular afferents. This makes the model suitable to test our hypothesis that the regular and irregular afferents have different ”specializations”, specifically about information in specific frequencies that they can convey. To support this, a confusion matrice is included in Figure 5.14 to demonstrate the model's discriminative performance for different neural responses, validating its utility for our study.

5.3.8. Validating: Gain and frequency results

Knowing that the model has the expected discrimination performance for different frequencies, we created the frequency dependent gain relationship based on the transfer functions defined earlier. When including both the I_{bias} for steady state behaviour (no stimulus input) and the sigmoidal erf function, the steady firing rate becomes the minimal firing rate. The use of the sigmoidal function inherently produces only positive values, regardless of the input. As a result, the model is unable to accurately represent negative accelerations, which would normally reduce the neuron's firing rate to zero. This limitation hinders the model's ability to capture the full range of physiological responses, particularly those involving inhibitory inputs.

To account for this we removed the sigmoidal transformation and argue that this is okay to do since the LIF model accounts for negative firing rate by itself, it cannot fire 'negatively'. This does not take into account the fact that each neuron has a refractory period of at least 3 ms [78].

To improve the accuracy of our LIF model, we incorporated a refractory period to reflect the natural behavior of biological neurons. After each spike, the neuron entered a brief period of inactivity during which it could not generate another spike. This was implemented by defining a refractory period

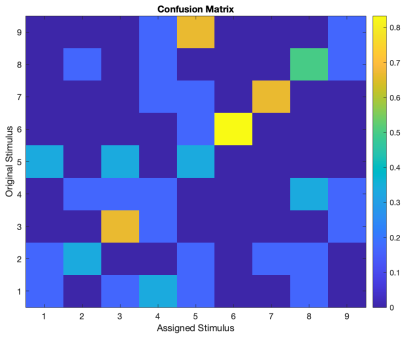

Figure 5.13: The confusion matrix represents the results of assigning spike trains to those generated by the same stimulus section. The diagonal entries indicate the proportion of experiments where the spike trains were correctly matched to their corresponding stimulus. Perfect discriminative performance would show as diagonal elements that are close to 1.

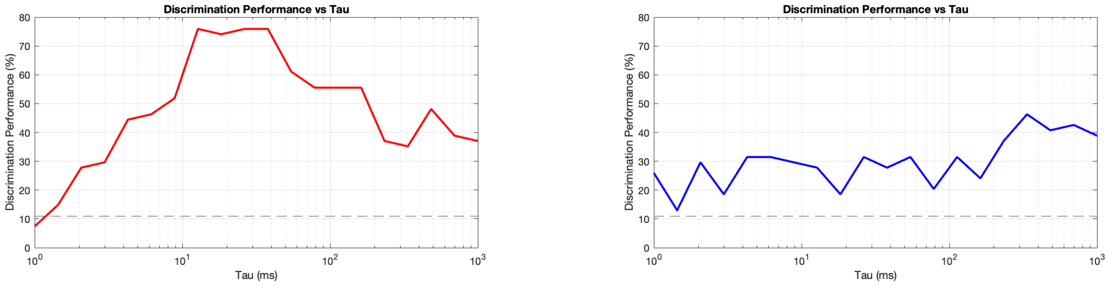

Left: Discrimination performance for irregular afferents based on the Van Rossum distance.

Right: Discrimination performance for regular afferents based on the Van Rossum distance.

Figure 5.14: Discrimination performance based on the Van Rossum distance for both irregular and regular afferents. The diagonal of the confusion matrix represents the number of correct classifications or matches, i.e., instances where the spike trains were correctly assigned to the stimulus they arose from. To use this information to derive a discrimination performance metric, we use the True Positive Rate (TPR).

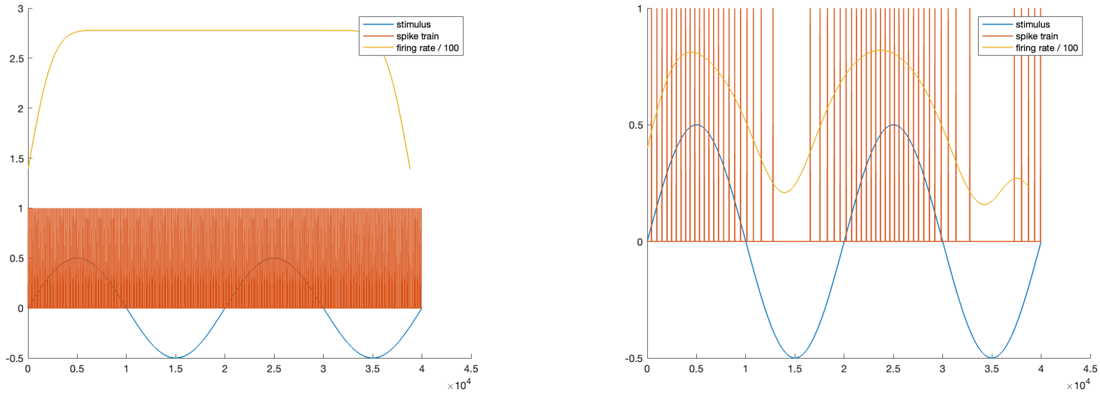

Incorporating both the nonlinear (sigmoid) transformation and the I_{bias} term results in a model that fails to produce valid spiking data.

Removing the sigmoid and extending the LIF model by introducing a 3 ms refractory period to enforce a firing limit yields satisfactory results.

Figure 5.15: Comparison of the spiking behavior in different LIF model configurations.

duration and adding logic to the model that kept the membrane potential fixed at the reset potential during this time. Specifically, after each spike, the model bypassed the voltage update, ensuring no further spikes occurred until the refractory period had elapsed.

This adjustment was crucial for accurately simulating neuronal dynamics, as it ensured the model adhered to the physiological constraints observed in real neurons. By including this refractory mechanism, the model better represented the temporal patterns of spike generation, particularly in scenarios involving high-frequency stimuli. This prevented the unrealistic accumulation of spikes and maintained the model's fidelity to biological processes.

The response of a simple sinusoid to the regular LIF model is shown in Figure 5.15. The firing rate has been calculated using a sliding window approach, using a window width of 0.03 s. Then smoothed with a Gaussian kernel.

The nonlinear sigmoidal function in combination with the linear transfer function can still be used to tune our LIF model. By creating variants of broadband noise inputs, low-pass filtered with a second-order Butterworth filter at 15 Hz, and modifying both I_{bias} and the sensitivity the LIF model can be tuned to align with the LNL model.
The right fit, that can be seen in Figure 5.16 was achieved with $I_{\text{bias}} = 3.63$ and a sensitivity of 1/30 and 1/60 for the irregular and regular afferent, respectively.

Regular

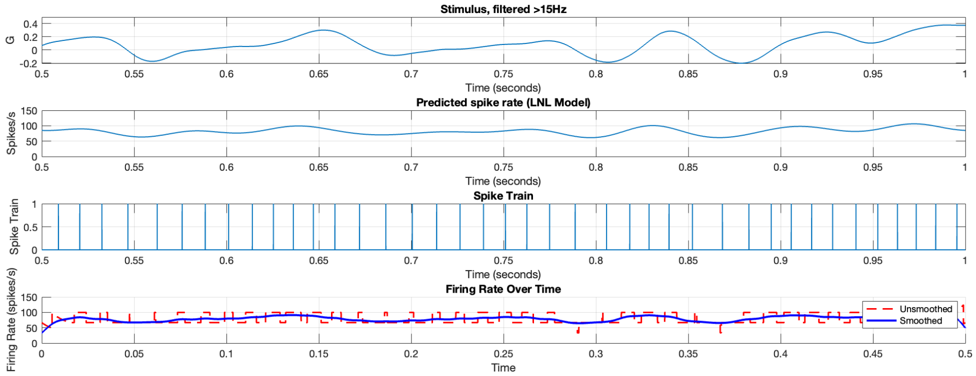

Irregular

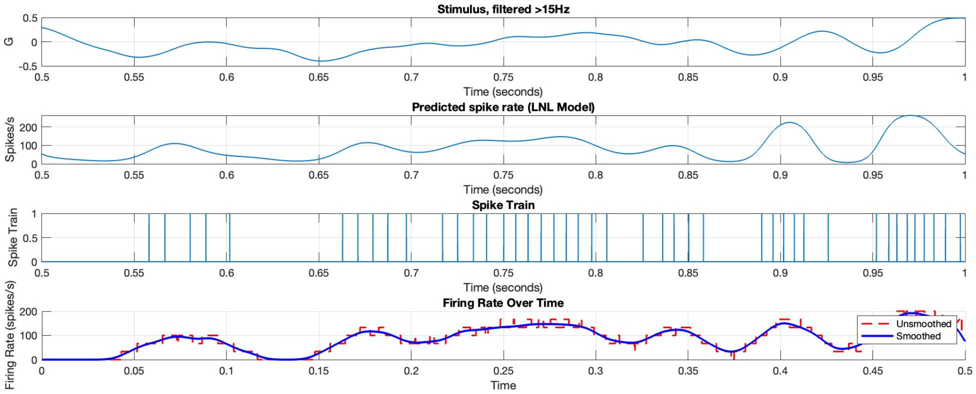

Figure 5.16: Tuning the LIF model using the LNL model. The model has been calibrated across various motion stimuli patterns to prevent overfitting.

5.4. Hodgkin-Huxley Model

The Leaky Integrate-and-Fire model successfully reproduces the experimental results from Jamali (2019) [48], capturing some aspects of neuronal behavior. While it shares certain similarities with biological neurons, its ability to accurately mimic their complexity is limited. In contrast, the Hodgkin-Huxley model provides a more detailed and accurate representation of neuronal activity, describing the initiation and propagation of action potentials based on the biophysical properties of neuronal membranes.

5.4.1. Principles and mathematical formulations

1. Ion channels and membrane potential: The model describes how the membrane potential of a neuron changes over time due to the flow of ions (such as sodium (Na^+) and potassium (K^+)) through ion channels in the neuron's membrane. The membrane potential is a voltage difference between the inside and the outside of the neuron, which is crucial for the initiation and propagation of action potentials.
2. Conductance-based model: The Hodgkin-Huxley model is a conductance-based model, where the flow of ions is described by their conductance (how easily ions pass through the membrane) and the difference between the membrane potential and the equilibrium potential of each ion. The model assumes that the ion channels can be open or closed, with the probability of being open depending on the membrane potential.
3. Gating variables: The probability that a channel is open is described by gating variables, which follow first-order kinetics. These gating variables change over time and are governed by differential equations. There are specific gating variables for each ion channel, such as m, h, and n for sodium and potassium channels, which represent the activation and inactivation processes of these channels.

The model is governed by the following equations:

Membrane potential: change in the membrane potential V over time is described by the following differential equation:

$$C_m \frac{dV}{dt} = I_{\text{ion}} + I_{\text{ext}} \tag{5.19}$$

where:

- C_m is the membrane capacitance.
- I_{ion} is the total ionic current, which is the sum of currents through different ion channels.
- I_{ext} is an external current applied to the neuron.

Ionic current: the total ionic current I_{ion} is the sum of the sodium, potassium, and leak currents:

$$I_{\text{ion}} = g_{\text{Na}}(V - E_{\text{Na}}) + g_{\text{K}}(V - E_{\text{K}}) + g_{\text{L}}(V - E_{\text{L}}) \tag{5.20}$$

where:

- $g_{\text{Na}}, g_{\text{K}}, g_{\text{L}}$ are the conductances for sodium, potassium, and leak channels, respectively.
- $E_{\text{Na}}, E_{\text{K}}, E_{\text{L}}$ are the equilibrium potentials for sodium, potassium, and leak currents, respectively.

Sodium and potassium conductance: conductance for sodium and potassium depends on the gating variables m, h, and n:

$$g_{\text{Na}} = \bar{g}_{\text{Na}} m^3 h \tag{5.21}$$

$$g_{\text{K}} = \bar{g}_{\text{K}} n^4 \tag{5.22}$$

where:

- $\bar{g}_{\text{Na}}$ and $\bar{g}_{\text{K}}$ are the maximum conductances for sodium and potassium channels.

- m is the activation gating variable for sodium, h is the inactivation gating variable for sodium, and n is the activation gating variable for potassium.

Gating variable dynamics: gating variables m, h, and n follow first-order differential equations:

$$\frac{dx}{dt} = \alpha_x(1-x) - \beta_x x \quad \text{for } x = m, h, n \tag{5.23}$$

where α_x and β_x are rate constants that depend on the membrane potential V.

The rate constants are given by formulas derived from experimental data:

$$\alpha_m(V) = \frac{0.1(V+40)}{1-e^{-(V+40)/10}} \tag{5.24}$$

$$\beta_m(V) = 4e^{-(V+65)/18} \tag{5.25}$$

$$\alpha_h(V) = 0.07e^{-(V+65)/20} \tag{5.26}$$

$$\beta_h(V) = \frac{1}{1+e^{-(V+35)/10}} \tag{5.27}$$

$$\alpha_n(V) = \frac{0.01(V+55)}{1-e^{-(V+55)/10}} \tag{5.28}$$

$$\beta_n(V) = 0.125e^{-(V+65)/80} \tag{5.29}$$

These equations describe how the gating variables change over time in response to changes in the membrane potential, thereby controlling the opening and closing of the ion channels.

In the Hodgkin-Huxley model, when the injected current is increased, the neuron undergoes a Hopf bifurcation. This leads to a characteristic behavior where the neuron either does not fire at all or fires at a minimum frequency, with no gradual increase in firing rate. The amplitude of the action potential does not increase smoothly but instead jumps suddenly. This all-or-none response is typical of neuronal models, where increasing the current typically increases the firing rate, but due to the Hopf bifurcation, there's a threshold below which no firing occurs and above which the neuron fires at a set minimum rate.

Next to the bifurcation, the model's complexity arises from the numerous equations and parameters involved, making it challenging to formulate without access to experimental data for parameter verification. This model is primarily designed for researchers who possess the necessary data to accurately implement and calibrate these parameters, enabling them to explore the intricate dynamics of neuronal behavior with precision. Luckily, Hight and Kalluri have done so for the vestibular afferents.

Hight and Kalluri[36] have adapted the Hodgkin-Huxley model so that it can replicate both the static discharge of regular and irregular neurons by altering one parameter in the model. They based their model on the model from Rothman et al. [82].
Kalluri et al. [51] proposed that the regularity of neuronal firing is influenced by the density of low-voltage-activated potassium currents (IKL). To investigate this, they developed a neuron model with three key conductances: transient sodium (gNa), low-voltage-activated potassium (gKL), and high-voltage-activated potassium (gKH). The model showed that removing gKL caused the neuron to depolarize, increased its input resistance, and changed its firing pattern from transient (brief) to sustained (continuous) when responding to current inputs. When the model included gKL, spikes occurred only in response to large, rapidly arriving synaptic events, leading to irregular firing patterns. In contrast, when gKL was absent, the neuron could integrate multiple rapid inputs and produced regular spiking patterns. This suggests that the presence of gKL promotes irregular spiking, while its absence supports

regular spiking, depending on the nature of the synaptic inputs.

We can replicate this model and use it as a base to create a spiking train that we can use in our Bayesian inference model.

The overall model can be conceptualized as two distinct components: one that generates the input signals and another that simulates the axon dynamics. The input generation model produces a combination of excitatory postsynaptic currents (EPSCs) and electrical currents. Although the current implementation does not include direct electrical stimulation, this input model could be adapted in future work to explore the effects of galvanic vestibular stimulation on motion sickness. The EPSCs are drawn from a distribution, reflecting the random nature of synaptic transmission, which introduces inherent variability into the model. Additionally, the axon dynamics contribute to this variability, as the model captures the nonlinear, chaotic behavior of neural responses.

Another source of input from the haircells is in the form of nonquantal transmission. This is mostly associated with high frequency stimuli, which we will not model. However, Steinhardt [89] has created an implementation for this in her HH model. If the need in the future arises, this could be added to our model as well. For now, we will only use EPSC input.

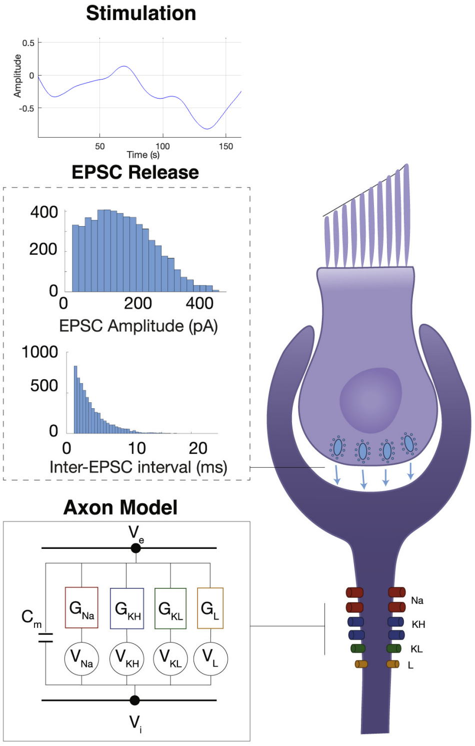

Figure 5.17: Overview of the Hodgkin-Huxley model shown for a Calyx (irregular) synapse. On the left the EPSC model and Axon model are shown. Adapted from [89] Figure 2.

5.4.2. EPSC input model

As described in the previous chapter, the input to the otolith afferent originates from the haircell, which sends vesicles through the synaptic connection to innervate the otolith afferent. The two types of synaptic connections, the bouton and the calyx, can produce both regular and irregular firing patterns. Similar pathways in fish have only bouton connections and can produce both firing patterns; this is why it is likely that the irregular firing pattern emerges from the axon's properties. Modeling the axon in an HH model means that we can change the properties to model both regular and irregular afferents.

Synaptic input is simulated by modeling EPSC distributions, as described in Chapter 4. The

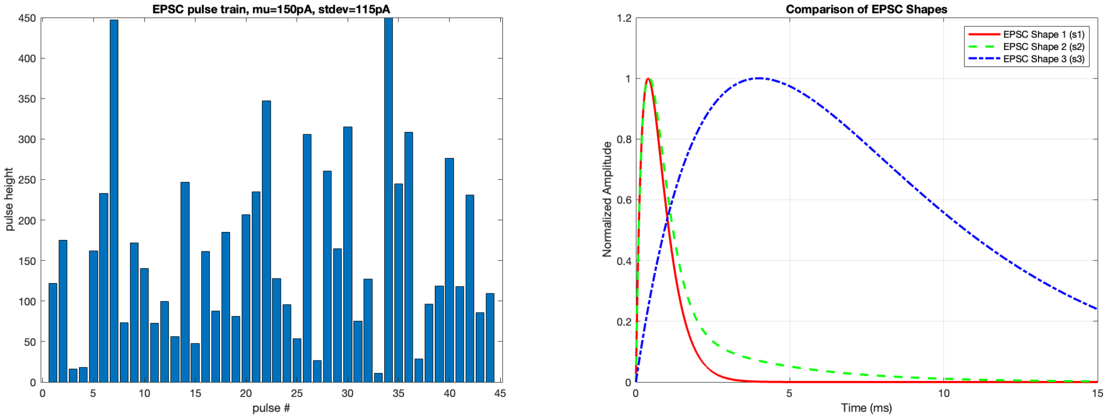

Figure 5.18: Left: EPSC pulses drawn from normal distribution before convolution. Right: overview of the different EPSC shapes implemented in the model. The convolution of the samples of the left distribution with the right shape is used as input for the axon model.

Hodgkin-Huxley (HH) model incorporates numerous biologically relevant parameters, which makes it crucial to use accurate values, since they significantly affect the spiking behavior. To ensure that the parameters align with biological reality, we use experimentally derived values from Steinhardt et al. [Steinhardt2021direct].

The EPSC (excitatory postsynaptic current) signal is generated by simulating the arrival of synaptic inputs at the neuron in a way that reflects the randomness and variability of real synaptic activity. First, the timing of each synaptic input is determined by generating intervals between pulses, known as inter-pulse intervals (IPTs), which are drawn from an exponential distribution. This approach captures the natural variability in the timing of synaptic events.

Each synaptic input, or pulse, also has a specific amplitude, referred to as the pulse height. These heights are sampled from a normal distribution, ensuring that most pulses have amplitudes around a certain average value, with some variation. Once the IPTs and pulse heights are established, a pulse train is created. This pulse train is essentially a series of time points where each synaptic input occurs, with each point in time marked by its corresponding amplitude.

To convert these sharp, discrete pulses into a more realistic synaptic signal, each pulse is shaped into an EPSC waveform, as can be seen in Figure 5.18. This waveform typically has a characteristic shape that rises quickly and then decays over time, mirroring the way real synaptic currents behave when they arrive at a neuron. The final EPSC signal is generated by convolving the pulse train with the EPSC shape, a process that smooths out the sharp spikes of the pulse train into smooth, continuous waveforms. The result is a realistic simulation of the synaptic currents that input the otolith axon.

Using an average inter-pulse interval (μ_{IPT}) of 0.75 ms and an EPSC shape s_1 with a mean amplitude of 150 pA, the static paradigm of EPSC release from the hair cells was simulated. The amplitude was choosen to reflect the synaptic current amplitudes and rates observed in voltage-clamped spiral ganglion terminals at approximately -97 mV, as measured by Hight et al. [36]. In Figure 5.19, the EPSC input is plotted alongside the corresponding response of the axon's membrane potential. The red markers indicate identified spikes.

5.4.3. Tuning the axon and input model

The axon model has 17 parameters to configure. Based on research Hight and Kalluri [36][89] 15 are set. The parameters in the axon that are subject to tuning are two of the conductance values, g_{Na} and g_{KL}. Those parameters determine sensitivity and irregularity of the spiking pattern.

To investigate the influence of the conductance value parameters we ran 150 simulations to quantify their relationship with the CV value. The result of the simulation can be seen in Figure 5.20. We found that for values of g_{Na}=25 and g_{KL}=0 the CV values over the whole ISI range of 0-100ms where lower

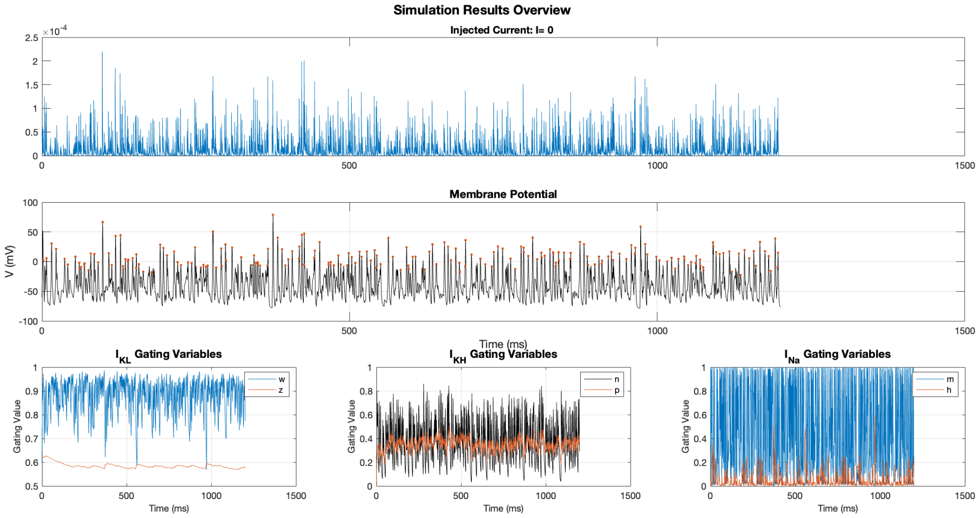

Figure 5.19: The result of the first simulation, only simulating a spike train with an EPSC input with: average pulse interval 0.75 ms and average pulse amplitude 150 pA. The resulting spike rate is approximately 90 spikes/s. Top: EPSC input from the input model. Middle: Membrane voltage including identified spikes. Bottom: State of the three ion channels, which are crucial to the dynamics of the model and therefore visualized here for clarity.

than for low g_{Na} and higher g_{KL} values. This corresponds with previous finding [36]. The irregular afferent, with values of g_{Na}= 13 and g_{KL}= 1.1 did show a clear trend that indicates that the CV value rises as the ISI increases. This corresponds with research by Fernandez et. al [26]. Surprisingly, the intermediate afferent, with values of g_{Na}= 13 and g_{KL}= 0, did not show a consistent trend. This could be due to implementation deviations.

We continued with the following two afferents:

- Irregular: $g_{\mathrm{Na}} = 13$ and $g_{\mathrm{KL}} = 1.1$
- Regular: $g_{\mathrm{Na}} = 25$ and $g_{\mathrm{KL}} = 0$

When simulating a regular neuron, the resulting coefficient of variation (CV) did not fall below 0.17. This is notable because regular afferents are typically classified as having a CV below 0.15, or even 0.1. Consequently, our current model does not accurately capture the behavior of regular afferent axons. Attempts to increase the sodium conductance (g_{Na}) further led to unrealistic results, indicating that simply adjusting this parameter is insufficient. To address this, the input variability needs to be reduced to decrease the variance in the output. The input is currently modeled using an exponential distribution to generate the mean inter-pulse interval (IPT), with a variance given by:

$$\text{Variance}_{\text{exponential}} = \left(\frac{1}{\lambda}\right)^2 = \frac{1}{\lambda^2} \tag{5.30}$$

where λ is the mean, defined as μ_{IPT}. Since the exponential distribution is characterized by a single parameter, λ, there is limited flexibility in adjusting its variance. However, we can influence the variability by modifying the normal distribution used to model the EPSC amplitude. By refining this distribution, we can better control the input variability and potentially achieve a more accurate representation of the regular afferent's response. When decreasing the standard deviation of the EPSC amplitude we eventually do approach an asymptotic value of 0.2 as well. Therefore, we concluded the model in its current form is not fully capable of simulating regular afferents.

Nevertheless, the model still holds utility in our Bayesian inference framework due to its capacity to differentiate between regular and irregular firing patterns, even though the statistical characteristics do not completely align with empirical data. Future work may explore the introduction of new mechanisms

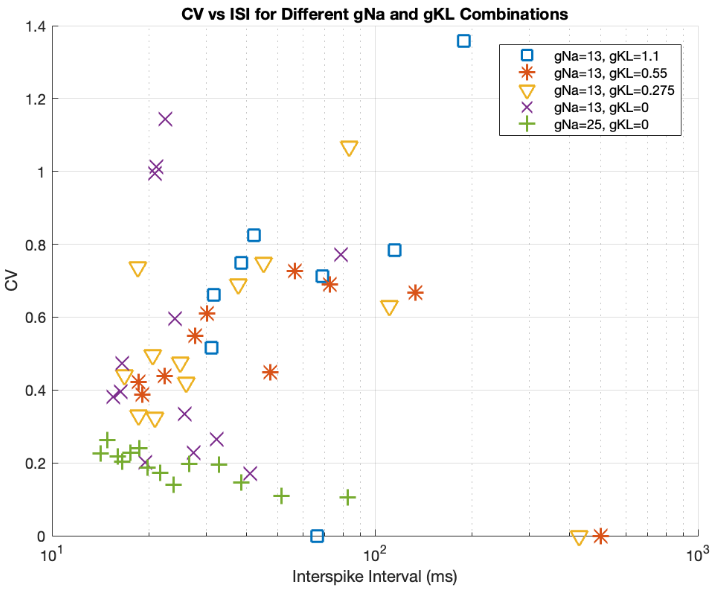

Figure 5.20: As EPSC amplitude is varied, from 0.01x to 3x the initial value of 150 pA, different axons have different ISI and CV response characteristics. The lower the CV value, the higher the regularity of the axon. We look at the overall trend, due to the nature of the simulation there are some artifacts/outliers in the results that we should ignore.

to address this discrepancy and enhance the model's accuracy in simulating regular afferent responses.

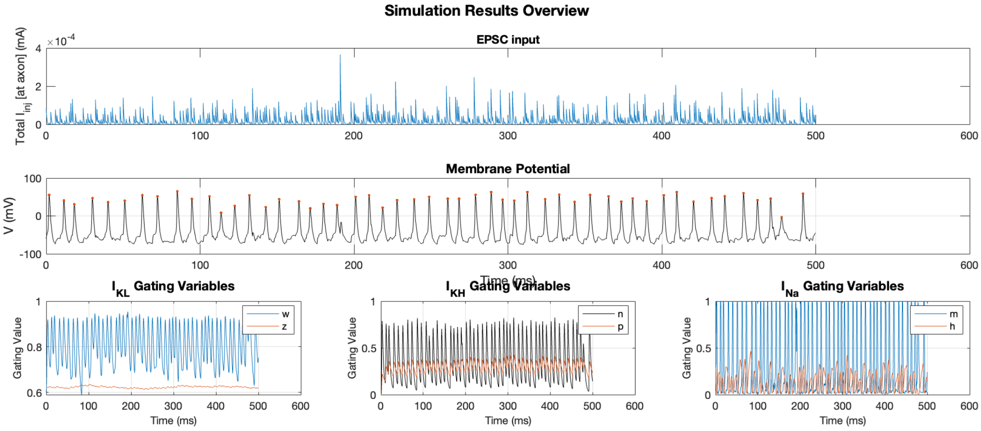

Figure 5.21: Afferent simulated as regular spiking with an ISI coefficient of variation of 0.177 over a period of 500ms.

Subsequently, the regular and irregular models were tuned to spike with about 79 spikes/s when no stimulation was given outside of the EPSC defined earlier, to simulate the resting state. This was done by simply changing the mean of the EPSC amplitude input until the mean of the firing rate over a simulation period of 10 seconds was 79 spikes/s.

After we achieved a baseline firing rate of approximately 79 spikes/s for both regular and irregular afferents and the coefficient of variation adjusted to mirror low CV values for regular afferents and high CV values for irregular afferents, we needed to tune the model to stimuli. A multi-frequency stimulus was implemented, ensuring it remained within the linear operational limits of otolith afferents and it's frequency content filter above 15 Hz, as we've done before for the LIF model. This was crucial to prevent the stimulus from inducing nonlinear responses, which could complicate the comparison between model outputs and physiological data. The stimulus was subsequently applied to the model in two ways:

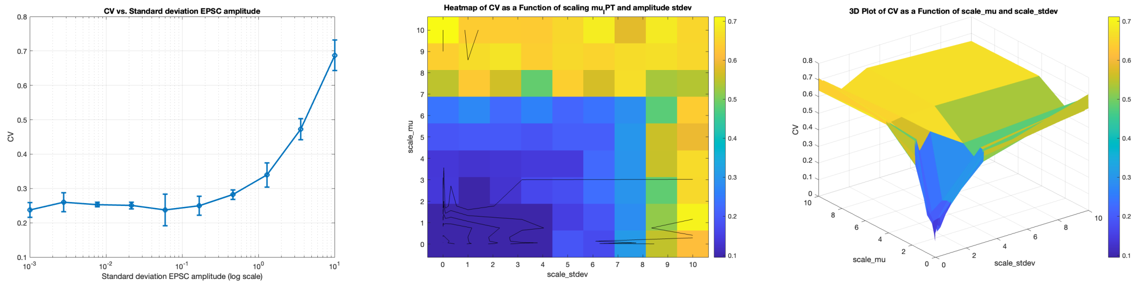

Figure 5.22: Left: As the standard deviation of the EPSC amplitude input is reduced, while, μ_{IPT} is kept constant, the CV correspondingly decreases, eventually approaching an asymptotic value of 0.2. Right: Scaling down both the standard deviation of the amplitude and (μ_{IPT}) further decreases the CV, but the value does not drop below 0.1. Since regular firing neurons are typically characterized by a CV of less than 0.1, this suggests that the model in its current form is unable to replicate these afferents.

HH EPSC input:

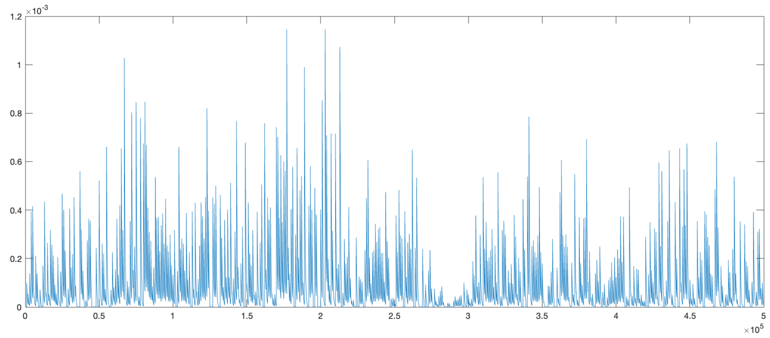

LNL & HH model responses:

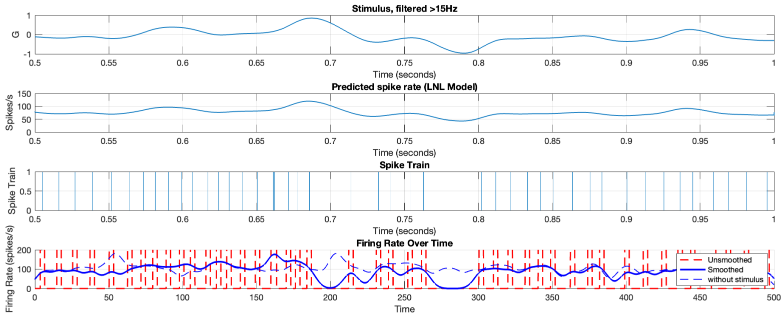

Figure 5.23: When attempting to match the regular model to the output predicted by the LNL model, the nonlinearities inherent in the Hodgkin-Huxley model, combined with the high variance in the EPSC data, make achieving an accurate match challenging. The bottom figure illustrates the response both in the absence of a stimulus (dashed lines) and when a stimulus is applied (solid lines). It becomes evident that the variance in the axon model's response is so significant that inferring the presence or characteristics of a stimulus from the resulting spike train is difficult.

Regular Afferent

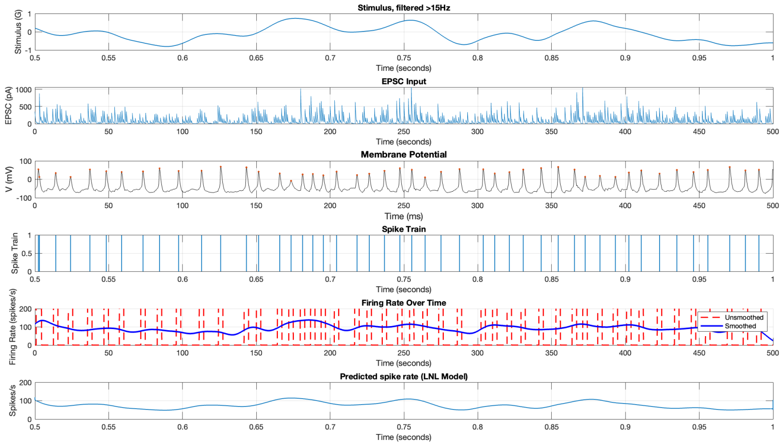

Irregular Afferent

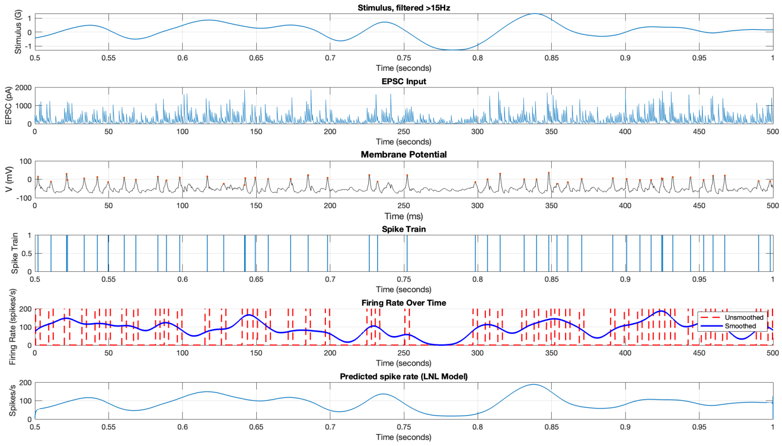

Figure 5.24: Matching the regular and irregular responses to the LNL model does not give satisfactory results. Both the models vary too much from the firing rate that is predicted by the LNL model.

directly to observe the model's response, and after passing it through a linear transfer function. The latter approach facilitated a comparison with a linearly-filtered input, similar to the linear-nonlinear (LNL) model we applied earlier.

The outputs from the model were then compared against the LNL model to evaluate the accuracy and reliability of the simulated afferent responses. The primary goal was to assess how well the model replicated the known physiological responses of vestibular afferents under varying stimulus conditions. To fine-tune the model's accuracy, the sensitivity to stimuli was iteratively adjusted, focusing on achieving the correct spike rate and variability (CV) characteristic of regular and irregular afferents.

Exploratory adjustments were considered and tried, including modifications to input distributions and model parameters. However, due to the model's chaotic and nonlinear nature, such adjustments were deemed overly complex and out of the scope of the current thesis. The final parameter settings, which were found to best represent the physiological characteristics of regular and irregular afferents, are summarized in the table below.

The Hodgkin-Huxley (HH) model is widely regarded as one of the most comprehensive frameworks for understanding neuronal dynamics due to its detailed biophysical representation of ionic conductances. However, its nonlinear nature presents significant challenges when attempting to reliably predict spike trains from stimuli. The primary difficulty lies in the model's sensitivity to initial conditions and

Parameter	Regular Afferents	Irregular Afferents
g_{KL}	0	2
g_{Na}	30	13
Sensitivity	0.01	0.01

Table 5.6: Parameter settings for fitting regular and irregular vestibular afferents responses.

parameter settings, which can lead to highly variable outcomes, particularly when simulating responses to complex or noisy stimuli.

The inherent nonlinearity of the HH model means that small changes in input or parameters can result in disproportionately large variations in output, making it difficult to achieve consistent and predictable results. This sensitivity complicates the task of parameter tuning, as the model may require fine adjustments to accurately reproduce physiological behaviors. However, even with meticulous calibration, the model's outputs often exhibit variability that is not entirely representative of actual neuronal responses.

Furthermore, the statistical properties of the spike trains generated by the HH model do not always align with experimental data. For instance, the coefficient of variation (CV) may differ from those observed in biological neurons. This discrepancy suggests that while the HH model captures the essential dynamics of action potential generation, it may not yet fully account for the statistics of otolith firing patterns. However, this first implementation shows that the model is promising and that reasonable results can be achieved.

In conclusion, the nonlinear nature of the Hodgkin-Huxley model, while crucial for its ability to replicate the complex dynamics of neuronal behavior, also limits its reliability as a predictive tool for spike train generation. The challenges in achieving consistent parameter settings and the mismatches in spike train statistics indicate that additional mechanisms or alternative modeling approaches may be necessary to more accurately simulate the probabilistic nature of neural responses. The model is four-dimensional, meaning it involves four coupled differential equations, one for each of the gating variables (m, h, n) and the membrane potential (V). This dimensionality makes the model computationally intensive and difficult to analyze, especially when extending it to networks of neurons. The gating variables (α and β) depend on the membrane potential (V), which adds further complexity to the system. These dependencies make the model highly sensitive to changes in voltage, and small perturbations can have significant effects, complicating both implementation and analysis.

5.4.4. Hodgkin-Huxley Specific Application: Motion Sickness Alleviation Through Noise Stimulation

The model remains valuable when empirical data for parameters is available and computational resources are sufficient. It offers a detailed way to simulate noise stimulation of the vestibular organs, which can help alleviate motion sickness.

A theoretical explanation for noise stimulation for motion sickness relieve is as follows. By applying Galvanic Vestibular Stimulation (GVS) to the vestibular organ, the baseline membrane current shifts, altering the amplitude of synaptic inputs (EPSCs) without changing their timing. These EPSCs follow a stochastic process, akin to "sampling" from a larger pool of potential events. The key concept is "sampling variance": cathodic GVS increases the number of EPSCs triggering action potentials (APs), reducing variability and resulting in more regular firing. Conversely, anodic stimulation decreases events, increasing variability and leading to less regular firing.

This relationship between event frequency and variability impacts the regularity of neuronal firing, measured by CV* (Coefficient of Variation). The model demonstrates that CV* can be adjusted predictably by modulating sampling variance under GVS, ensuring consistent firing patterns even without new EPSCs. This suggests that anodic stimulation could increase the variance of otolith afferents. This in turn decreases their influence in Bayesian estimation of motion and reducing sensory conflict and thus alleviate motion sickness.

This would be a valuable purpose for a HH model based inference model and should be explored in the future.

5.5. Generalized Linear Model(s)

Arguably, the simplest way to create a spike train from a stimulus is to use a generalized linear model (GLM). Using a GLM for spike train generation involves modeling the relationship between a set of input stimuli and the spiking activity of a neuron. When using a Poisson process, the GLM framework is particularly well-suited because the Poisson distribution naturally models the random occurrence of spikes over time.

We considered two alternative models: the Exwald distribution and Hawkes processes. Both were explored through the development of basic models. However, due to time constraints, we opted to continue with the Poisson model, as it offered the simplest implementation.

5.5.1. Poisson GLM framework

The Poisson GLM framework combines the earlier defined linear transfer functions with a Poisson process embedding.

The Poisson GLM is based on the assumption that the spike generation process of a neuron can be modeled as a Poisson process. This process is characterized by the fact that spikes occur randomly over time, with the probability of a spike occurring in a small time interval being proportional to the instantaneous firing rate, λ. A coefficient of variation (CV) of an afferent, which is based on its interspike interval, aligns with the standard deviation of its spike rate. Specifically, afferents with a CV of 1 exhibit a standard deviation that is equal to their mean firing rate, which is characteristic of a Poisson distribution. Thus this Poisson framework is especially applicable to irregular otolith afferents with a CV of 1.

The first step involves applying a linear filter to the input stimulus. Here we can use the linear filter from Angelaki et al. [1], which captures the influence of stimuli on neuronal activity and transforms the stimulus into a firing rate. The output of the linear filter is then passed through a nonlinear function. This step transforms the linear input drive into a non-negative firing rate. The exponential function is particularly suitable as it ensures the firing rate is always positive and can model a wide range of firing rate responses, from low to high, in response to changes in the input. Here we can use the nonlinear transformation defined by [85], but any sigmoid with unit slope and a cutoffs at ±0 spikes/s and 300 spikes/s should work. When using a Poisson process we do not necessarily need to use a nonlinear transformation, since it will not produce spikes when the rate parameter is below 0. The firing rate obtained from the nonlinear transformation is used as the rate parameter λ in a Poisson distribution. At each time step, a spike is generated with a probability determined by this Poisson distribution.

The probability of observing k spikes in an interval Δt is given by:

$$P(N = k) = \frac{(\lambda(t) \cdot \Delta t)^k \cdot e^{-\lambda(t) \cdot \Delta t}}{k!} \tag{5.31}$$

where:

- N is the number of spikes.
- k is the number of spikes in the interval Δt.
- $\lambda(t) \cdot \Delta t$ is the expected number of spikes in that interval.

The Matlab function poissrnd($\lambda(t) \cdot \Delta t$) generates a random number according to this distribution, representing the actual number of spikes that occur in the time interval Δt. This number can be 0, 1, 2, etc., but is probabilistically weighted by the Poisson distribution's parameters. This means that there is a possibility that a single neuron spikes twice at one time instance. As this is biophysically not possible, it is a shortcoming of the model. However, to simulate neuron population dynamics, assuming Poisson statistics, the model is usable.

As can be seen in Figure 5.25, the model spikes during peaks of stimuli in the preferred direction, as expected. Note that for this implementation the input is a simple sinusoid and the transfer functions that map the frequency dynamics are not implemented. It can also be seen that there does not occur spiking when the firing rate is lower then 0, showing the model's natural resilience against "negative firing rate" input. To investigate the statistics of the Poisson process model, we ran a 1000 trials in parallel and measured both the mean spike rate and its standard deviation over time. As can be seen in Figure 5.26, and as stated in the theory, the variance increases as the spike rate increases.

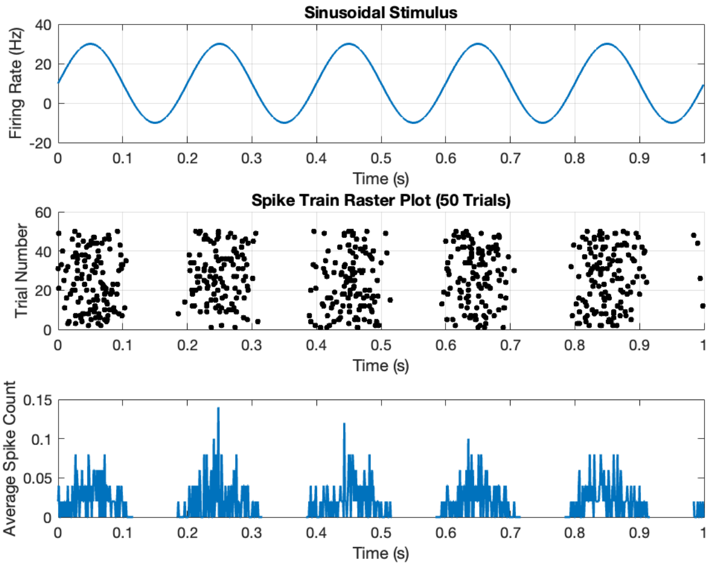

Figure 5.25: 50 neurons simulated by a Poisson process model that evaluates the input at every timestep.

Poisson Distribution and CV Value
Fernandez et al. [26] have quantified the relationship between the standard deviation of vestibular neuron firing rates and their interspike intervals (ISI), encapsulated in the coefficient of variation (CV), as illustrated in Figure 4.4.

To determine the standard deviation of the firing rate given the coefficient of variation (CV) of the ISI, we use the following definitions and relationships:

- Firing Rate (FR): The number of spikes per second, defined as the reciprocal of the ISI:

$$\mathrm{FR} = \frac{1}{\mathrm{ISI}}$$

- Interspike Interval (ISI): The time between successive spikes.
- Standard Deviation of ISI (σ_{ISI}): Provided as 1 ms for an ISI of 10 ms.
- Coefficient of Variation (CV): The ratio of the standard deviation to the mean of the ISI:

$$\mathrm{CV} = \frac{\sigma_{\mathrm{ISI}}}{\mu_{\mathrm{ISI}}}$$

Using the given information, we calculate the relationship between the CV value and the standard deviation of the firing rate:

$$\begin{aligned}
\mu_{\mathrm{ISI}} &= 10 \text{ ms} \\
\sigma_{\mathrm{ISI}} &= 0.1 \times 10 \text{ ms} = 1 \text{ ms} \\
\mu_{\mathrm{FR}} &= \frac{1}{\mu_{\mathrm{ISI}}} = \frac{1}{10 \text{ ms}} = 100 \text{ Hz} \\
\sigma_{\mathrm{FR}} &= \frac{\sigma_{\mathrm{ISI}}}{\mu_{\mathrm{ISI}}^2} = \frac{1 \text{ ms}}{(10 \text{ ms})^2} = \frac{1}{100} \text{ kHz} = 0.01 \text{ kHz} = 10 \text{ Hz}
\end{aligned}$$

This analysis indicates that the coefficient of variation (CV) of an afferent directly correlates with the standard deviation of its firing rate. Specifically, afferents with a CV of 1 exhibit a standard deviation equal to their mean firing rate, a characteristic of a Poisson distribution.

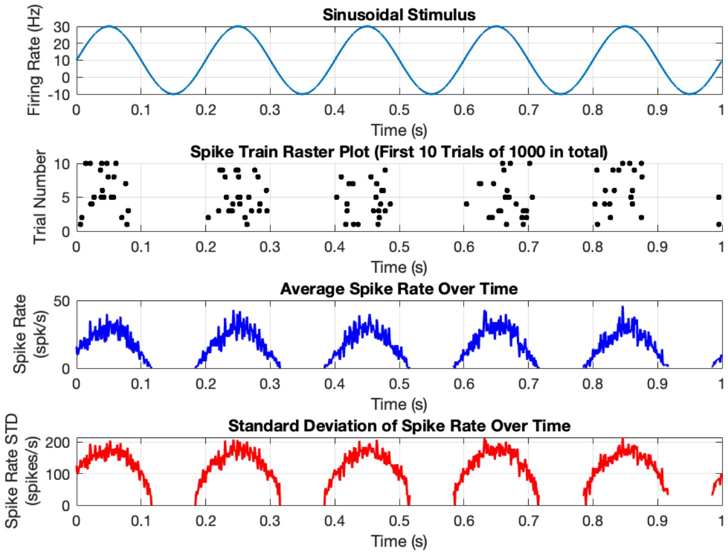

Figure 5.26: Poisson process model: When running 1000 neurons in parallel, we can get an idea about the standard deviation in the spike rate.

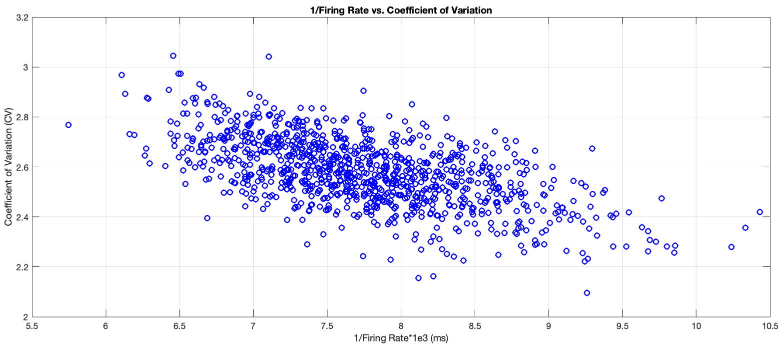

Figure 5.27: Poisson process model: The coefficient of variation (CV) of the spike rate is plotted against the inverse of the spike rate. The negative correlation observed here is not in line with empirical results from [26]. This suggests that the Poisson process may not be an ideal candidate for accurately modeling spike rate variability.

5.5.2. Exwald GLM

The Poisson framework is only applicable to highly irregular afferents with a CV of 1. Another distribution is needed for more regular afferents.

Paulin et al. [80] evaluated spike train data from chinchilla semicircular canal neurons and found that their complex organization can be accurately modeled with just three parameters. These spike trains are described by Exwald distributions, a combination of Inverse Gaussian and Exponential distributions. They showed that neurons can naturally compute these distributions, enabling efficient Bayesian estimation of head movements. This model suggests that Bayesian inference, driven by energy efficiency, is fundamental to nervous system evolution. The brain likely uses this method to process vestibular information, computing head kinematics from sensory data. After a discussion with Paulin, we concluded that it should be possible to implement an Exwald based model for the otolith afferents as well. This will be included in the future work section.

5.6. Conclusion on Neuron Spiking Models

The implementation of various neural models, including the Leaky Integrate-and-Fire (LIF) model, the Hodgkin-Huxley model, and Generalized Linear Model (GLM)-based approaches, has produced plausible spike trains that capture essential neuronal dynamics. Each of these models has its strengths, but also certain limitations in specific contexts.

The Hodgkin-Huxley model, while highly detailed and biologically accurate, particularly in its ability to simulate the ionic currents underlying action potentials, proved inadequate in replicating the spiking statistics of regular afferents. This limitation is critical because accurately capturing these statistics is essential for performing reliable Bayesian inference, which depends on precise modeling of spike train variability and temporal dynamics. There is also a practical downside to the HH model, which is the large computation capacity required. This limits the time length and amount of parallel models that can be run on an ordinary laptop.

On the other hand, the GLM framework offers a simpler yet effective approach to generating spike trains that are consistent with observed neural data. The GLM allows for the incorporation of both stimulus features and spike history effects, making it well-suited for initial proofs of concept where flexibility and ease of implementation are crucial. However, the GLM, while powerful for specific applications, lacks the biophysical realism and detailed temporal dynamics that may be necessary in more complex scenarios.

Given these considerations, we propose to use the GLM framework for demonstrating the Bayesian inference concept, as it provides a balance between simplicity and the ability to capture key statistics of neural spiking. For the final model, however, we will transition to the Leaky Integrate-and-Fire (LIF) model. The LIF model provides a good balance between computational efficiency and biological plausibility, allowing for the replication of essential spiking statistics while being more manageable than the Hodgkin-Huxley model. The LIF model's simplicity makes it particularly useful for large-scale simulations and integration with Bayesian frameworks, where the focus is on the probabilistic interpretation of neural coding rather than on detailed ionic mechanisms. Another important point to note is that the implementation of the LIF model replicates the frequency-dependent discrimination characteristics observed in actual otolith afferents. This alignment with empirical data increases the likelihood that our data will provide strong evidence, allowing us to either reject or fail to reject our hypothesis with greater confidence.

In conclusion, the GLM framework will be employed for initial validation of the Bayesian inference process, while the LIF model will be the preferred choice in the final model due to its suitability for accurately replicating the spiking characteristics necessary for robust Bayesian analysis. The Hodgkin-Huxley (HH) model is considerably more computationally expensive. This longer computation time limits its practicality for large-scale simulations but may be valuable for scenarios where detailed neuronal behavior is critical.

Model	Computation Time	Timestep (dt)	Simulation Duration
LIF Model	0.1 seconds	0.000025 seconds	2 seconds
GLM Model	0.01 seconds	0.000025 seconds	2 seconds
HH Model	15 seconds	0.000025 seconds	2 seconds

Table 5.7: Comparison of computation times for different models on an Apple M1 Silicon processor.

6

Estimating Perception and Sickness using Bayesian Inference

6.1. Introduction

To estimate orientation and motion perception in a way that is plausible for the brain to use, we must define a method that is biologically plausible and consistent with known neural mechanisms.

The brain is believed to operate in a way similar to Bayesian inference [28]. When the brain receives sensory input, like sights, sounds or motions, it does not just passively absorb the information. Instead, it actively interprets this input by comparing it against prior experiences, prior probabilities. The brain constantly updates its beliefs about the environment based on new sensory information, effectively calculating a ”posterior” belief that combines what it already knows with what it has just perceived. This approach allows the brain to make more accurate and reliable predictions about the world, even when the sensory information is incomplete or noisy.

As discussed in Chapter 5, when the otoliths convert motion into a signal that is used for inference of motion, the signal contains noise. To make reliable estimates about the original stimulus it is believed the neural sections after the vestibular sensory afferents perform Bayesian inference [79], this is what we are modelling in this chapter.

Bayesian inference is a statistical method that updates the probability estimate for a hypothesis as more evidence or information becomes available. It is based on Bayes' Theorem, which mathematically combines two key components: the prior probability and the likelihood. The prior probability represents your initial belief or knowledge about a hypothesis before considering the current evidence. It's what you think might be true based on previous experiences or general knowledge. The likelihood is the probability of the observed evidence assuming that the hypothesis is true. It represents how likely the new evidence is given your hypothesis. After considering the new evidence, the prior probability is updated to form the posterior probability, which is a revised estimate of the hypothesis's probability. For more information on experiments and references that provide a strong backing for the Bayesian brain theory, I refer to the chapter ”Bayesian Brain” included in my attached literature review.

The mathematical formulation of Bayes' Theorem is as follows:

$$\text{Posterior Probability} = \frac{\text{Likelihood} \times \text{Prior Probability}}{\text{Probability of the Evidence}} \tag{6.1}$$

6.1.1. Overview on approach

The Bayesian framework offers many possibilities for modeling motion perception and predicting motion sickness. In this section, we present the approach used in this research.

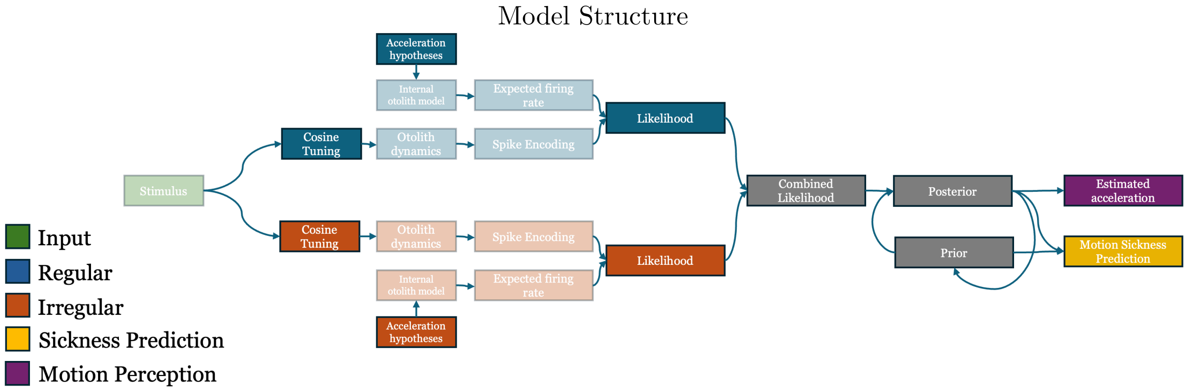

Figure 6.1: Structure of the whole acceleration estimation and sickness prediction process. We will go through the highlighted modules in this chapter. Transparent modules refer to Figure 5.1 in the previous chapter.

In line with other neural inference models [81], we define a rate-based model. This means that we assume that stochastic firing of spikes can be measured as a firing rate. We note that this could be valid for the peripheral otolith afferent fibers, but is probably not for the cerebellum and higher cortical areas involved in spatial orientation and balance. There are more signals integrated in these areas and the information in the signals is probably not all given in the firing rate. However, it is likely that these integrations occur in a Bayesian way. Thus, our approach could possibly be modified later to include encoding principles different to firing rate.

There are three 'streams' that are needed for Bayesian inference: the sensory data that provides the input data, the internal model to which the maximum likelihood is estimated, and the prior probability which will be recurrently based on the posterior probability. The sensory data stream we have defined in the previous chapter. For the internal model, we could choose the same models, but we need to define the distributions on which the maximum likelihood estimation is based. Alternatively we could use sampling methods like a particle filter. In Figure 5.1 we can see an overview of the process.

The decision to avoid using a particle filter at this stage is grounded in the desire to maintain a deterministic approach to understanding the dynamics of the model. Particle filters, while powerful for dealing with non-linear and non-Gaussian processes, inherently introduce elements of sampling and stochasticity, which can complicate the initial interpretation of the model's behavior. Bayesian inference with Maximum Likelihood Estimation (MLE) is typically deterministic in the sense that, given a set of data and a model, it will always produce the same result if the same data and model parameters are used. It also has symmetries to how the neural system functions [79].

The primary goal of the model is to accurately replicate motion perception by simulating the sensory inputs and processing mechanisms involved in detecting motion, despite the presence of noisy sensory data. We base this on the assumption that the neural structures responsible for these functions have evolved over millions of years to optimally estimate acceleration, even with imperfect sensory information, including efficient energy use by the brain. Additionally, the model is designed to generate a metric that quantifies the likelihood of motion sickness as a secondary outcome. This dual-purpose approach not only deepens our understanding of the connection between motion perception and the onset of motion sickness, but also tries to draw a parallel to processes that occur in the brain.

6.1.2. Overview on the different models

We have developed a range of models, each with distinct specifications. The model structures were refined in steps, based on empirical observations and theoretical considerations. We began with the simplest model configuration, using it as a base to introduce modifications and enhancements as needed. We started with a simple model and gradually introduced changes and improvements, allowing us to explore how various assumptions and parameters affect the model's accuracy and robustness. By starting with a basic model and making iterative improvements, we were able to identify the key factors that influence the model performance. This step-by-step approach helped us pinpoint key factors influencing the model's performance, leading to increasingly sophisticated proposed representations of the otolith system. The evolution of these models is described in Table 6.1.

Model	Regularity	PD Tuning	Spike Model	MLE	Prior	Gravity
0	Regular	Gauss/Cos	GLM	-	Recursive Gaussian	×
1	Regular	Cosine	LIF	Poisson	Recursive Gaussian	×
2	Regular	Cosine	LIF	Dyn. Gauss.	Recursive Gaussian	×
3	Reg. + Irreg.	Cosine	LIF	Dyn. Gauss.	Recursive Gaussian	×
4	Reg. + Irreg.	Cosine	LIF	Dyn. Gauss.	Based on Posterior	×
5	Reg. + Irreg.	Cosine	LIF retuned	Dyn. Gauss.	Based on Posterior	✓

Table 6.1: Evolution of models and their changes in configurations.
Dyn. Gauss. = Dynamic Gaussian, Reg. = Regular, Irreg. = Irregular

A summary on the final model, Model 4:

Our approach is called model-based MLE. The goal is to estimate the most likely acceleration that could have generated the observed spike train data and the subsequent motion sickness incidence. Steps involved:

1. Hair cells are cosine-tuned to a sinusoidal stimulus.
2. This stimulus is transformed into spike trains for both regular and irregular afferents by an Leaky-Integrate-and-Fire model.
3. The model differentiates between regular and irregular neurons, each with distinct noise characteristics and response properties.
4. For each time window, the model calculates the likelihood of different acceleration values F given the observed spike rates for both regular and irregular neurons.
5. The likelihoods are computed based on a Gaussian distribution, where the spike rate is compared to the expected firing rate given by the cosine-tuned internal model.
6. The standard deviation for the Gaussian distribution is scaled by the spike rate itself, reflecting the variability in neuron firing [26].
7. The likelihoods from regular and irregular neurons are combined multiplicatively. Regular and irregular neuron data are combined to form a joint likelihood.
8. The likelihoods are normalized to ensure that they sum to 1, making them valid probability distributions.
9. The prior is set to a Gaussian distribution centered around a prior estimate to incorporate previous knowledge.
10. The prior is multiplied by the likelihood to obtain the posterior distribution.
11. Maximum A Posteriori (MAP) is used to estimate the acceleration.
12. KL Divergence is calculated to quantify the difference between the prior and posterior distributions. While KL Divergence itself is not directly equivalent to Motion Sickness Incidence (MSI), it is a measure that can be used in the process of predicting MSI.

The model is parameterized by the expected firing rates of neurons, which are functions of the acceleration and frequency. The likelihood is constructed for each possible value of F based on the degree to which the observed spike rates match the expected rates under the model. For each window of time, the MLE finds the value of F that maximizes the combined likelihood function. This value of F is the one that the model considers most likely, given the data.

Note: The above steps do not match the numbering of steps indicated in section 3.5.
Note 2: Consistency in units is the aim throughout this thesis, but keep in mind: F $\propto$ a to avoid confusion.

The following sections will include both a description of the evolution of the model and preliminary results. The results for the final model are outlined in chapter 7.

6.2. Preferred Direction Tuning

6.2.1. Tuning curve definition

Each neuron has a preferred direction (PD), which is the direction of movement that elicits the highest firing rate from the neuron. This section describes Step 1 in Figure 3.1.

The relationship between the firing rate of the neuron and the direction of movement can often be described by a cosine function. Mathematically, the firing rate $R(\theta)$ as a function of the angle θ between the preferred direction and the actual direction of movement can be modeled as:

$$R(\theta) = R_{\text{baseline}} + R_{\text{max}} \cdot \cos(\theta - \theta_{\text{preferred}}) \tag{6.2}$$

where:

- $R(\theta)$ is the firing rate of the neuron for a given direction θ,
- R_{baseline} is the baseline firing rate of the neuron when no movement is occurring,
- R_{max} is the maximum modulation of the firing rate above the baseline when the movement is in the preferred direction,
- $\theta_{\text{preferred}}$ is the angle corresponding to the neuron's preferred direction.

In the context of population coding and Poisson encoding models, the expected firing rate $f_i(F)$ of a neuron i given a stimulus F is often modeled as proportional to some function of the stimulus. A common formulation is:

$$f_i(F) \propto g(F, \theta_i) \tag{6.3}$$

where:

- $f_i(F)$ is the firing rate of neuron i given the stimulus F.
- $g(F, \theta_i)$ is a function that describes the neuron's response to the stimulus F parameterized by θ_i.
- θ_i are parameters specific to the neuron i, which could include factors such as the preferred stimulus or the parameters of the tuning curve.

A typical form for $g(F, \theta_i)$ in neural coding could be a Gaussian tuning curve model, such as:

$$f_i(F) \propto \exp\left(-\frac{(F - \theta_i)^2}{2\sigma^2}\right)$$

In this case, θ_i could represent the preferred stimulus of neuron i, and σ represents the width of the tuning curve.

Given that the neurons are tuned in a cosine relation to the force F_{max}, we can use a tuning curve to model the expected firing rates. In this case, the firing rate $f_i(F)$ of neuron i given a stimulus force F and the preferred direction/angle Θ_i can be expressed as follows:

$$f_i(F) \propto \exp\left(-\frac{(F\cos(\Theta_i) - F_{max})^2}{2\sigma^2}\right) \tag{6.4}$$

Where:

- $F\cos(\Theta_i)$ represents the component of the force F in the direction of the neuron's preferred angle Θ_i.
- F_{max} is the maximum force that can be expected.
- σ is the standard deviation of the tuning curve, controlling the width of the tuning curve.

This expression models the firing rate $f_i(F)$ as being proportional to a Gaussian function centered around the preferred direction's force component $F\cos(\Theta_i)$:

$$f_i(F) = A\exp\left(-\frac{(F\cos(\Theta_i) - F_{max})^2}{2\sigma^2}\right) \tag{6.5}$$

where A is a proportionality constant. This formula shows that the firing rate of a neuron is highest when the force F is aligned with the neuron's preferred direction Θ_i, and decreases as the alignment deviates from this preferred direction.

6.2.2. Combining the tuning curve with a probability distribution

The formulation describes a Gaussian tuning curve, which is used to model how the firing rate of a neuron changes with respect to the stimulus. However, the actual spike trains of neurons are often modeled using a Poisson process. We use the Gaussian tuning curve to estimate the expected firing rate, and then generate spikes based on that rate using a Poisson process.

1. Gaussian Tuning Curve: This determines the expected firing rate $f_i(F)$ based on the stimulus F:
$$f_i(F) = A \exp\left(-\frac{(F\cos(\Theta_i) - F_{max})^2}{2\sigma^2}\right) \tag{6.6}$$
2. Poisson Encoding: Given this expected firing rate $f_i(F)$, the expected spike train of the neuron is modeled as a Poisson process with rate $f_i(F)$.

To put it all together:

- The expected firing rate $f_i(F)$ is determined by the Gaussian tuning curve.
- The spikes are modeled as being generated from a Poisson distribution with mean $f_i(F)$.

A explicit formulation that incorporates both aspects:

1. The expected firing rate:
$$f_i(F) = A \exp\left(-\frac{(F\cos(\Theta_i) - F_{max})^2}{2\sigma^2}\right)$$
2. The spike count r_i in a given time window as a Poisson random variable:
$$r_i \sim \text{Poisson}(f_i(F))$$

This means that for each neuron i, given the stimulus F, the number of spikes r_i in a given time window follows a Poisson distribution with mean $f_i(F)$.

The Poisson distribution describes the probability of a given number of events (spikes) occurring in a fixed interval of time or space, given a known constant mean rate of occurrence. The formula for the Poisson distribution is:

$$P(r_i|\lambda_i) = \frac{\lambda_i^{r_i} e^{-\lambda_i}}{r_i!}$$

where:

- $P(r_i|\lambda_i)$ is the probability of observing r_i spikes.
- r_i is the spike count (number of spikes) for neuron i in a given time window.
- λ_i is the expected firing rate (mean number of spikes) for neuron i in that time window. This value we will replace with $f_i(F)$.
- e is the base of the natural logarithm.

In the context of our model:

1. The expected firing rate λ_i is given by the Gaussian tuning curve:
$$\lambda_i = f_i(F) = A \exp\left(-\frac{(F\cos(\Theta_i) - F_{max})^2}{2\sigma^2}\right)$$
2. The spike count r_i for neuron i follows a Poisson distribution with mean λ_i:
$$P(r_i|\lambda_i) = \frac{\left[A \exp\left(-\frac{(F\cos(\Theta_i) - F_{max})^2}{2\sigma^2}\right)\right]^{r_i} e^{-A \exp\left(-\frac{(F\cos(\Theta_i) - F_{max})^2}{2\sigma^2}\right)}}{r_i!}$$

Putting it all together, the probability of observing r_i spikes for neuron i given the stimulus F is:

$$P(r_i|F) = \frac{\left[A \exp\left(-\frac{(F\cos(\Theta_i)-F_{max})^2}{2\sigma^2}\right)\right]^{r_i} e^{-A\exp\left(-\frac{(F\cos(\Theta_i)-F_{max})^2}{2\sigma^2}\right)}}{r_i!}$$

This formula combines the Gaussian tuning curve to determine the expected firing rate and the Poisson distribution to model the actual spike counts. Our MLE estimator is initially based on the assumption that the brain encodes information using this method, as it is well-supported in existing literature [98]. However, as we further improve this model, we will adapt this approach to better align with observed data.

Gaussian curve

When doing experiments using a Gaussian curve, as can be seen in Figure 6.2, the observable acceleration range is limited by the maximum acceleration specified ahead of the experiment. If an unexpected large acceleration would occur, it would not be able to fit in the predefined Gaussian mapping. This is a disadvantage when using a Gaussian curve in the context of otolith afferents. Another example can be seen in Figure 6.4, where the forces on the x-axis shown the predefined variables that can be used to estimate the sensory data. When the sensory data goes beyond the bounds of these variables, the model will consider any of the variables to have small likelihood, since the variables do not match the incoming data. As explained, the Gaussian tuning curve 'maps' the orientation of a haircell to an expected spiking rate. This expected spiking rate is based on acceleration/force. In Figure 6.4 you can see the mapping used for the first experiments. During the experiments, we were able to estimate the stimulus. However, when the amplitude of the stimulus was increased, the model was unable to track it. The resulting spike trains from this tuning curve can be seen in Figure 6.5. It is clear in their spiking pattern that the neurons have a preferred direction. This proves that the concept works as expected.

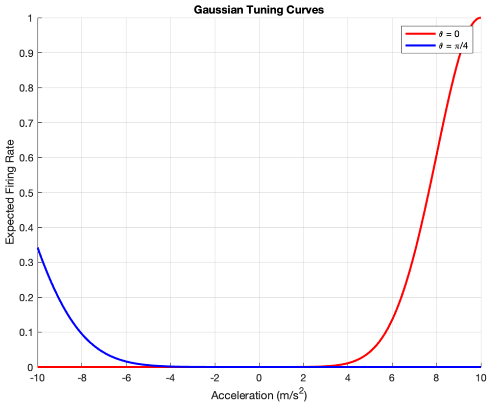

Figure 6.2: Gaussian tuning curves for angles 0 and $\frac{\pi}{4}$. We can see that the range is limited by the maximum and minimum acceleration.

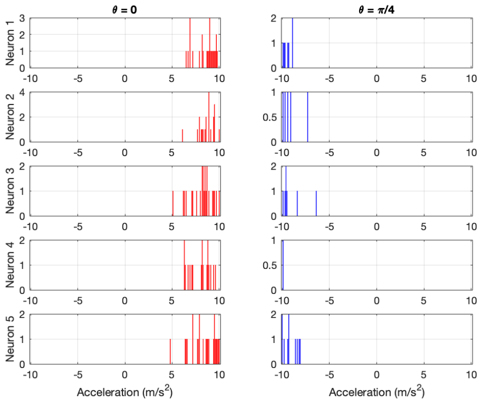

Figure 6.3: Response of Poisson process model to different accelerations.

When we extend the model to have a larger number of 100 neurons, we get the spike trains shown in Figure 6.6. The model is able to read the pattern of the spike trains and infer the original stimuli. Note that processing more neurons in parallel provides computational overhead, so we need to find a balance between accuracy and validity of the model and the computational efficiency.

Cosine curve

Since the Gaussian tuning curve does not exhibit the desired behavior, we will adopt an alternative approach. An alternative to Gaussian tuning is Cosine tuning, which is commonly used in neuroscientific research [93]. We assume that the hair cells are uniformly spread around a circle and for this pure vertical experiment located in either the coronal or sagittal plane (in the saccular macula). The preferred direction of each hair cell is characterized by an angle Θ_i, which represents the orientation of the hair cell relative to the vertical force vector. The key idea behind cosine tuning is that the force

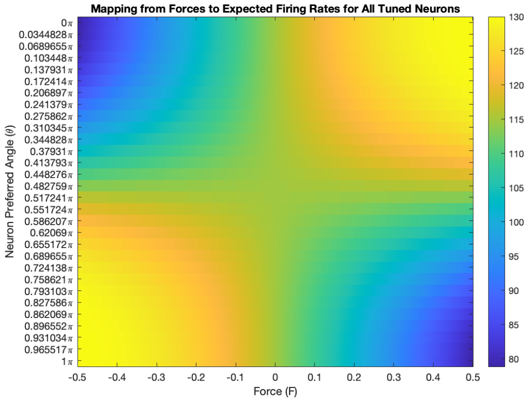

Figure 6.4: When using Gaussian tuning, each neuron has an expected firing rate based on the magnitude of the force. If an acceleration outside of this mapping presents itself, the model is not able to map it. While this approach is used often in neuroscience, this does not seem a realistic approach for our model.

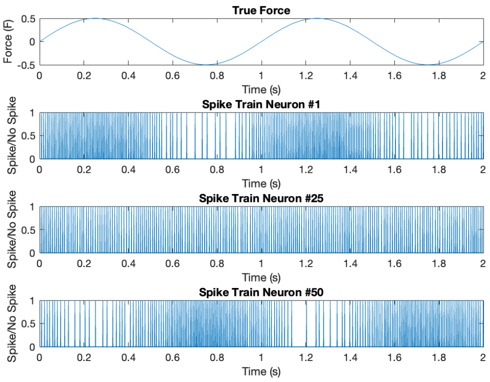

Figure 6.5: The input force and resulting spike trains. Neuron number 25, oriented $\pi/2$ radians away from the direction of acceleration, does not receive any input since it is tuned perpendicular to the force. Number 50, oriented π radians relative to the acceleration, is sensitive in the direction opposite to number 1's sensitivity.

experienced by each hair cell in its preferred direction is proportional to the cosine of this angle.

If we denote the magnitude of the vertical force as F , then the force component F_i acting in the preferred direction of hair cell i is given by the formula:

$$F_i = F \cdot \cos(\Theta_i) \tag{6.7}$$

where:

- Θ_i: The angle between the vertical force vector and the preferred direction of the ith hair cell.
- F_i: The force component in the preferred direction of the ith hair cell.

This means that the response of each hair cell depends on how aligned it is with the direction of the force. For hair cells that are perfectly aligned with the force (where $\Theta_i = 0$ or $\Theta_i = 2\pi$), they experience the full magnitude of the force. In contrast, hair cells that are orthogonal to the force direction (where $\Theta_i = \pi/2$ or $\Theta_i = 3\pi/2$) experience no force in their preferred direction. Hair cells that align in the opposite direction to the force (where $\Theta_i = \pi$) experience the force in the opposite direction, resulting in a negative force component. It is believed this is how the otoliths are structured and interact with forces [27].

This approach helps the neural system with the limitations of neuron saturation. Saturation typically occurs when a large number of neurons are activated simultaneously at their maximum firing rates, which can reduce the system's ability to encode additional information or respond to changes in stimulus intensity. The cosine tuning ensures that even under strong forces, only some hair cells reach their maximum firing rates, while others respond at lower levels or not at all. This balanced activation across the population of hair cells means that the overall input to the vestibular afferents remains within a manageable range, reducing the likelihood of saturation. Different cells reach their peak response at different force magnitudes and directions, so afferent signals represent a wide range of stimulus intensities without reaching the maximum of the capacity. Because many hair cells are distributed across different orientations, the system is not reliant on a single group of cells to encode force information. This redundancy allows the system to maintain accurate encoding even if some cells are saturated or do not respond well.

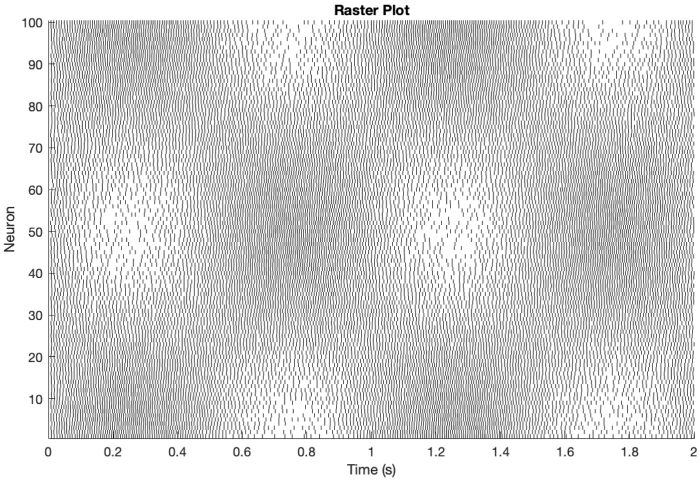

Figure 6.6: Proving the concept works with the Leaky Integrate-and-Fire model as well. Simulating 100 otolith afferents using the LIF model. The otoliths are all positioned in different preferred direction.

6.3. Model 1

Regular firing + Cosine tuning + Leaky-Integrate-and-Fire Model + Poisson MLE

Using a cosine tuning curve, we encoded a sinusoidal stimulus with a frequency of 1 Hz and an amplitude of 0.5G, modeling both regular and irregular afferents. The resulting spike trains, as illustrated in Figure 6.7, were then incorporated into a Bayesian framework as sensory input. Initially, we will use regular spiking patterns as input for our inference model.

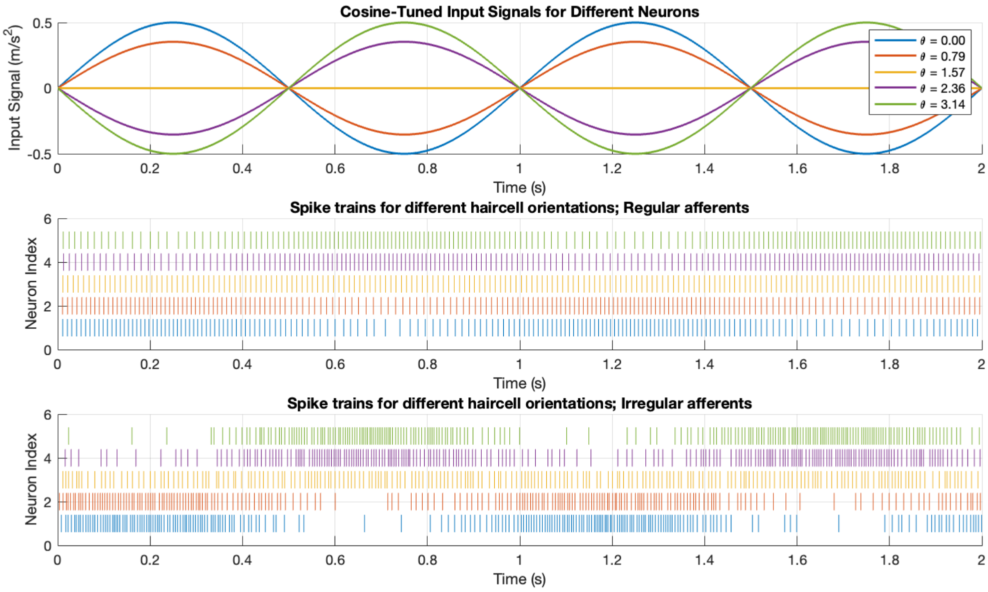

Figure 6.7: For regular and irregular afferents: Encoding of a sinusoidal stimulus with a frequency of 1 Hz and an amplitude of 0.5 m/s² by hair cells situated around a half circle.

6.3.1. Structure of Maximum Likelihood Estimation

Maximum Likelihood Estimation (MLE) is a method used in Bayesian inference to estimate the parameters of a statistical model. In Bayesian inference, we often have some hypothesized parameters that describe our model, and we want to determine the values of these parameters that make our observed data most likely.

The likelihood function is the probability of observing the firing rate r given the acceleration a. Mathematically, this is expressed as:

$$L(a) = P(r|a) \tag{6.8}$$

If we have multiple neurons, say $r_1, r_2, \ldots, r_n$, and assume they are independent, the likelihood function becomes:

$$L(a) = \prod_{i=1}^{n} P(r_i|a) \tag{6.9}$$

where n is the total number of neurons, we initially will use 5 neurons spread out over a half circle.

To estimate the acceleration a that best explains the observed firing rates, we maximize the likelihood function. The value of a that maximizes $L(a)$ is called the maximum likelihood estimate $\hat{a}$. This is expressed as:

$$\hat{a} = \arg\max_a L(a) \tag{6.10}$$

Suppose we hypothesize that the firing rate r follows a Poisson distribution with parameter a, representing the acceleration. Given observed data (e.g., firing rates $r_1, r_2, \ldots, r_n$), the MLE would find the value of a that maximizes the likelihood $L(a)$.

6.3.2. Poisson MLE

Given that we assume a Poisson distribution for the spike trains during the MLE process and that the Gamma distribution is the conjugate prior for the Poisson, it is analytically ideal to define our prior using a Gamma distribution. In this case, if the prior distribution for the rate parameter λ follows a Gamma distribution, the posterior distribution will also be Gamma after incorporating the observed Poisson-distributed data. This conjugate relationship greatly simplifies the update process and ensures consistency between the prior and posterior distributions.

However, since we are calculating the posterior numerically, we are not strictly bound to using the conjugate prior. Instead, we can choose a prior that may be more convenient or better suited to our data or model requirements. For example, we might opt to use a Gaussian distribution as the prior for λ, despite it being non-conjugate, because it offers flexibility and may better represent prior beliefs or empirical data regarding the firing rates.

The standard deviation σ of the Gaussian prior allows us to control the spread of the prior distribution, thereby influencing how strongly the prior beliefs affect the posterior distribution. A smaller σ suggests that we have high confidence in our prior estimate of λ, while a larger σ indicates greater uncertainty and allows the observed data to have a stronger influence on the posterior.

In our approach, we define the prior using a Gaussian distribution, with σ set based on considerations of the firing rate. This allows us to incorporate empirical knowledge or assumptions about the expected variability in the firing rates, while still leveraging numerical methods to calculate the posterior distribution, providing a robust framework for inference even in the absence of a conjugate prior.

The prior is initially Gaussian, centered around the maximum expected value F_{max} for the first time window. For subsequent windows, it is centered around the previous estimated acceleration. This Gaussian prior is represented as:

$$\text{prior} = \exp\left(-\frac{(F_{\text{values}} - \mu_{\text{prior}})^2}{2\sigma^2}\right) \tag{6.11}$$

where μ_{prior} is either F_{max} or the estimated acceleration at the previous timestep.

For each time window w, we calculate the total number of spikes for each neuron within that time window. The spike rate for each neuron is determined by dividing the spike count by the duration of the time window. For each possible value of acceleration, we calculate the expected firing rate f_i . This is based on the cosine tuning curve that relates the acceleration force and the neuron's preferred direction Θ_i. We created a formulation for the expected firing rate based on the transfer functions defined earlier, in Chapter 5. The likelihood of observing the actual spike rates given the expected firing rates is then calculated using the Poisson probability mass function:

$$\text{Likelihood}(F) = \prod_{i=1}^{N} \frac{\lambda_i^{k_i} e^{-\lambda_i}}{k_i!} \tag{6.12}$$

Where:

- N is the number of neurons
- k_i represents the observed spike rate (or spike count) for the ith neuron
- λ_i is the expected firing rate for the ith neurons

When dealing with likelihoods that can become extremely small, a common approach to prevent numerical underflow is to work with log-likelihoods rather than likelihoods themselves. This is because

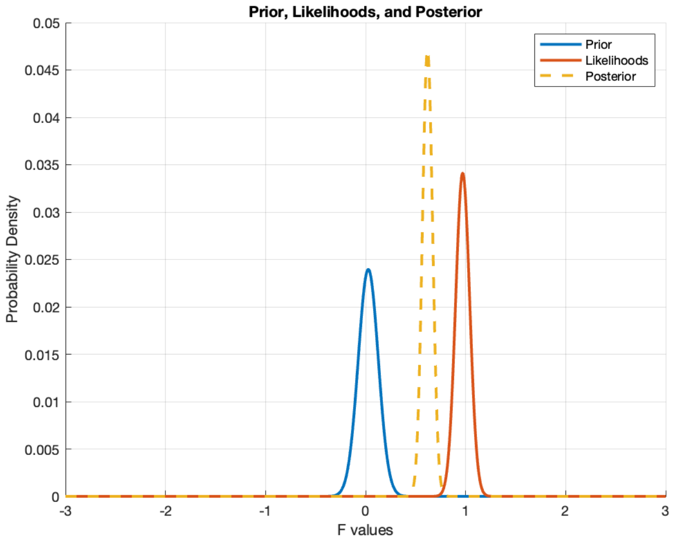

Figure 6.8: An example from a randomly selected update step in model 4.

the logarithm of a product becomes a sum, which helps prevent the values from becoming too small to represent numerically. The Log-Likelihood is later transformed back into Likelihood.

$$\text{Log-Likelihood}(F) = \sum_{i=1}^{N} [k_i \cdot \log(\lambda_i) - \lambda_i - \log(k_i!)] \tag{6.13}$$

We then calculate the posterior by multiplying the likelihood by the prior:

$$\text{posterior} = \frac{\text{likelihoods} \times \text{prior}}{\sum \text{likelihoods} \times \text{prior}} \tag{6.14}$$

We can see the process visualized in Figure 6.8. In this example, we can see that the prior is centered approximately around 0G and that the sensory measurements result in a likelihood at 1G. The resulting posterior is then calculated to be around 0.8G. The reason the sensory data is weighted more than the prior distribution is due to the lower spread in the data of the sensory data.

6.3.3. Acceleration Estimation

We estimate the acceleration using the Maximum A Posteriori (MAP) method, which identifies the parameter value with the highest probability in the posterior distribution. In this context, the MAP estimate corresponds to the “mode” of the posterior, representing the most likely value of acceleration based on the observed data and the defined inference model. This method provides a robust estimation by combining prior knowledge with the likelihood of the observed data.

An alternative approach to MAP would be to use the expected value (or mean) of the posterior distribution, which takes into account the entire distribution rather than just the peak. This approach could provide a more nuanced estimate, particularly in cases where the posterior distribution is skewed or multi-modal, as it accounts for the entire probability mass rather than focusing solely on the mode. However, for our implementation, this gave worse acceleration estimation results.

When the size of the neuron population is limited to just five neurons, the estimation response becomes highly variable. However, by increasing the population size to 50 neurons, the response becomes smoother. This improvement is a result of averaging the individual likelihoods during the likelihood calculation stage, effectively reducing variability and enhancing the stability of the inferred response. The model is able to infer the accelerations accurately, as can be seen in Figure 6.9.

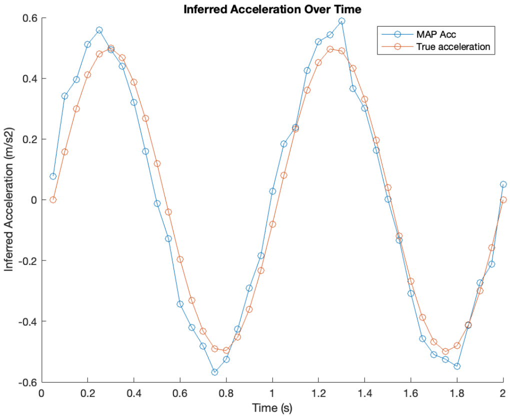

Figure 6.9: The model is able to accurately estimate the acceleration, thus giving accurate perception for vertical motions. Note that due to the slight phase lead of the otolith transfer function, the estimation also has a phase lead. When we calculate the RMS Error: 0.075053 m/s^2.

6.3.4. Motion Sickness prediction

Now we have established a model that is able to perform motion perception, lets see if we can also model the resulting motion sickness. For this we make use of the Kullback-Leibler divergence metric.

Kullback-Leibler (KL) divergence is a fundamental measure of the difference between two probability distributions, its unit when using the natural logarithm is in nats. In Bayesian inference, it is used to assess how well a predicted distribution approximates the true distribution of outcomes. KL divergence captures both the difference in central tendency (bias) and the spread (variance) between distributions, making it an ideal tool for quantifying the accuracy of Bayesian inference.

In cognitive neuroscience, it is hypothesized that the brain minimizes prediction errors by reducing KL divergence between its internal models and the external world [28]. The difference between the posterior and the prior, often referred to as 'surprisal,' represents the discrepancy between our expectations and the incoming sensory data.

To quantify this difference in a Bayesian framework, the KL divergence at each time window can be calculated as:

$$\text{KL divergence} = \sum_{x \in \mathcal{X}} P(x) \log \left(\frac{P(x)}{Q(x)} \right)$$

where P(x) represents the posterior distribution and Q(x) represents the prior distribution.

It is important to note that KL divergence provides a combined measure of both the spread (variance) and bias (mean) differences between distributions. To gain deeper insights into the onset of motion sickness, it would be valuable to separate these components and analyze them individually.

An alternative way to measure performance of the vestibular inference mechanism would be to measure the root-mean-square deviation (RMS error) between the stimulus and the estimate. If we assume the proprioceptive system and the eyes are able to give us a perfect estimate of our accelerations, we could use the original stimulus acceleration signal to compare to the best estimate (MAP) from the otolith organs data. The error should scale with the Motion Sickness Incidence, which can be measured empirically. This is out of scope for this thesis, but it is a future research direction.

6.3.5. O'Hanlon et al. Model

Remember that the data we are expecting to emerge from the perception model is similar to the data from O'Hanlon et. al[49]. The model, shown in Figure 6.11, demonstrates a strong fit to empirical data. The accuracy of the O'Hanlon model is evidenced by its low root-mean-square (RMS) deviation of only 3.96% between the model and the actual experimental data. It does ignores several critical factors,

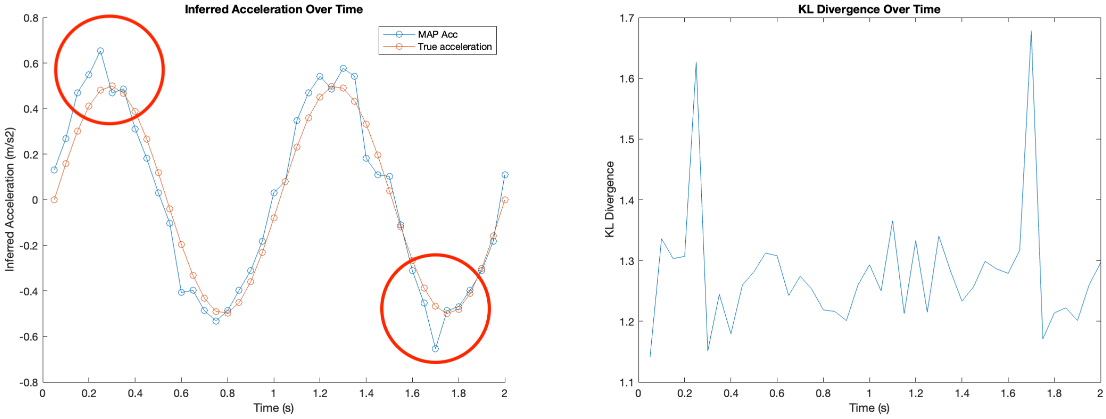

Figure 6.10: We can see that the peaks of the KL divergence over time match the prediction errors from the model.

such as the exposure period and acclimatization to motion. Without considering these variables, the model's predictions might be less accurate or applicable in real-world scenarios where exposure times can vary greatly and acclimatization can significantly affect an individual's response to motion. The model assumes a simplistic relationship between frequency, acceleration, and MSI, potentially overlooking other complex physiological and psychological factors that contribute to motion sickness. For instance, the model does not account for the possible cumulative effects of motion exposure over time, which could influence MSI in prolonged exposures. However, the model is still relevant to predict sensitivity to vertical frequencies and accelerations.

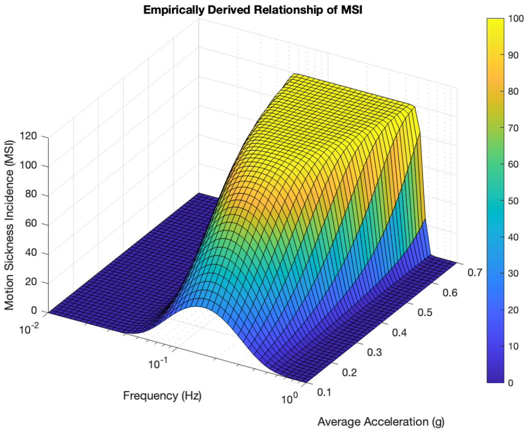

Figure 6.11: Motion Sickness Incidence curve based on the original O'Hanlon et al. [49] function of MSI for vertical sinusoidal motion.

6.3.6. Motion Sickness Results

We begin by simulating a 1 Hz sinusoidal signal with an amplitude of 0.5G and measuring the KL divergence at each timestep. The results, shown in Figure 6.10, indicate that the KL divergence increases at the peaks and troughs of the acceleration. To further analyze how KL divergence varies with different frequencies, we will run the model for 5 seconds across a range of sinusoidal inputs and calculate the average KL Divergence for each scenario. The average is calculated by dividing the sum of all KL divergences with the number of timesteps in the simulation. This secures that we can compare simulations of different time lengths.

As shown in Figure 6.12, there is a pronounced peak around 2.5 Hz, which supports our hypothesis that regular neurons may struggle to perform optimally beyond their typical response range for static

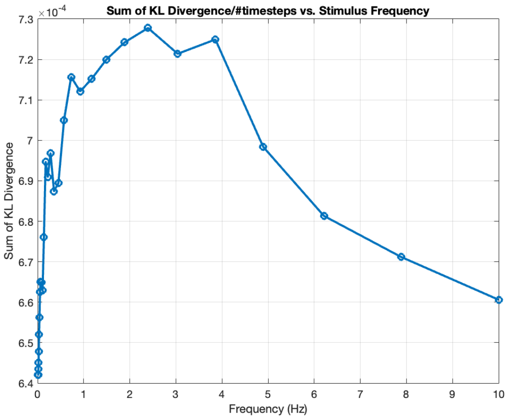

Figure 6.12: Average KL divergence during a 5 second stimulus as function of input stimuli frequency, at an amplitude of 0.5 m/s^2.

or low-frequency stimuli. This finding suggests a frequency-dependent limitation in the regular neurons' ability to encode motion information accurately at higher frequencies. This finding aligns with the experimental results[49], where a peak was observed at 0.17 Hz, although our results are an order of magnitude higher.

McCauley provides information about the motion sickness incidence at different amplitudes, ranging from 0.1G to 0.7G. This is shown in Figure 6.16.

Given that irregular neurons exhibit better discrimination at frequencies above 0.1 Hz, it is hypothesized that the neural pathway places greater emphasis on irregular neurons in the perception process at these higher frequencies. This could indicate that the regular afferents do not play a role in transmitting higher frequency information and the 'surprisal' is thus minimized above 0.1 Hz due to influence of the irregular afferents. To evaluate this we will include the irregular neurons in the model as well.

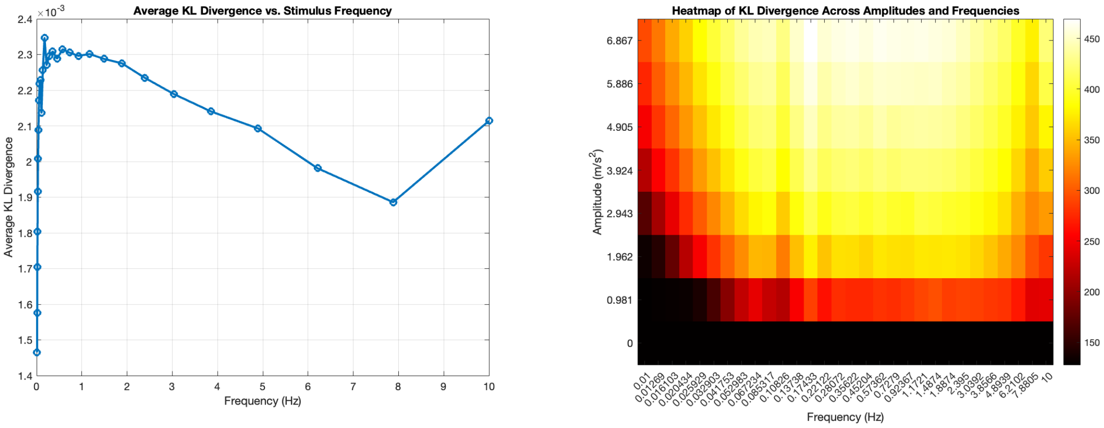

Figure 6.13: Average KL divergence per frequency for a sinusoidal motion with an amplitude of 0.7G.

Figure 6.14: Heatmap of average KL divergence per combination of sinusoid amplitude and frequency.

Figure 6.15: Model 1: results showing average KL divergence dependency on frequency and amplitude.

The spike train data is divided into smaller, fixed-length time intervals, or windows, each of size w. This means that within each window, we consider the spikes that occurred in that specific time interval. The window size w is a critical parameter as it determines the temporal resolution of our analysis. A smaller w provides finer temporal resolution, but may result in less data within each window, while a larger w increases the data available in each window but reduces the temporal resolution.

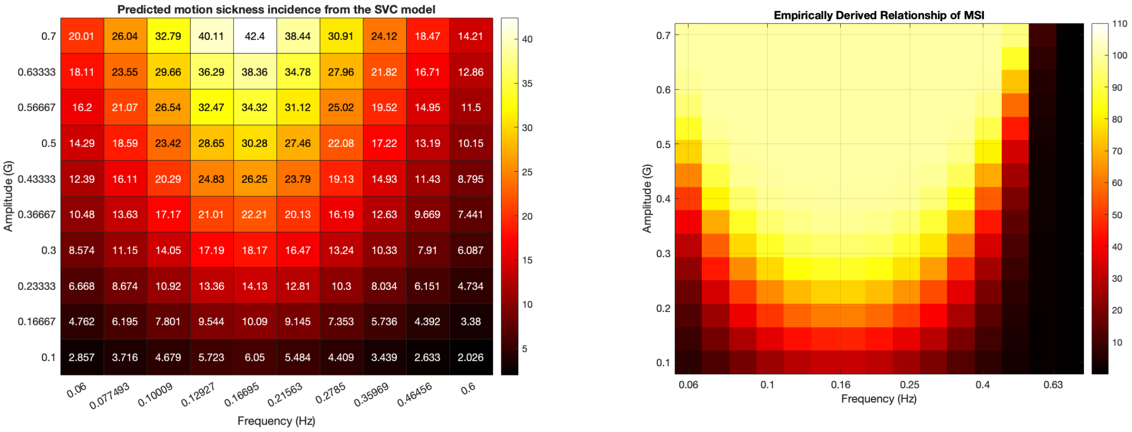

Amplitude (G)	0.06	0.077493	0.10009	0.12927	0.16695	0.21563	0.2785	0.35969	0.46456	0.6
0.7	20.01	26.04	32.79	40.11	42.4	38.44	30.91	24.12	18.47	14.21
0.63333	18.11	23.55	29.66	36.29	38.36	34.78	27.96	21.82	16.71	12.86
0.56667	16.2	21.07	26.54	32.47	34.32	31.12	25.02	19.52	14.95	11.5
0.5	14.29	18.59	23.42	28.65	30.28	27.46	22.08	17.22	13.19	10.15
0.43333	12.39	16.11	20.29	24.83	26.25	23.79	19.13	14.93	11.43	8.795
0.36667	10.48	13.63	17.17	21.01	22.21	20.13	16.19	12.63	9.669	7.441
0.3	8.574	11.15	14.05	17.19	18.17	16.47	13.24	10.33	7.91	6.087
0.23333	6.668	8.674	10.92	13.36	14.13	12.81	10.3	8.034	6.151	4.734
0.16667	4.762	6.195	7.801	9.544	10.09	9.145	7.353	5.736	4.392	3.38
0.1	2.857	3.716	4.679	5.723	6.05	5.484	4.409	3.439	2.633	2.026

SVC Model: MSI intensity heatmap.

O'Hanlon model: MSI intensity heatmap [49]

Figure 6.16: Examples of MSI intensity heatmap from the SVC model and experimental data from O'Hanlon et al.

6.3.7. Conclusion

Model 1 provides accurate acceleration estimations and promising sickness results. There is a clear amplitude and frequency dependency for motion sickness that emerges from the model. This validates our approach in the sense that it is a possible explanation for the way motion perception is performed in the neural pathway and that KL Divergence can function as a proxy metric for Motion Sickness Incidence.

6.3.8. Shortcomings

Model 1 has several shortcomings. First, the Poisson Maximum Likelihood Estimation (MLE) does not account for population distribution information that is encoded by the spiking models. In a Poisson model, the variance is assumed to be equal to the expected value, λ. However, in regular neurons, the inter-spike interval (ISI) variance is often lower than the mean (underdispersed), which this model fails to capture.

Additionally, an elegant approach to argue the fact that the surprisal should go down above 0.1 Hz would involve a mechanism that incorporates both the rate encoding and the precise spiking characteristics of the afferents, offering a more accurate and nuanced representation of their role in sensory processing. This could be implemented using the Van Rossum metric, this is out of scope for this thesis, but is recommended for future work.

To address one of these two key shortcomings, following sections present a model that specifically accounts for the irregular afferents.

6.3.9. Model 1.1: Irregular afferent

If we simply replicate the model concept from the regular afferents, using the irregular transfer functions, we get the KL divergence result in Figure 6.17 and acceleration estimations in Figure 6.18. Based on the assumption that the irregular afferents are better in describing the high frequency information [48], we would assume that the KL Divergence goes down for these frequencies. That seems to be the case here. However, a surprising result is that the KL Divergence decreases for low frequencies, which means the perception performance increases for low frequencies. Based on Jamali (2019) and a discussion with professor Ian Curthoys, who is an expert on the otoliths, this seems unlikely. We argue this is due to the assumed distributions which do not reflect the sensory data.

6.3.10. Proposal on improvements

Before we include both the regular and irregular afferents in our model, we make a distinction in the assumption that we make for the distributions for the regular and irregular afferents. In model 1.1 they

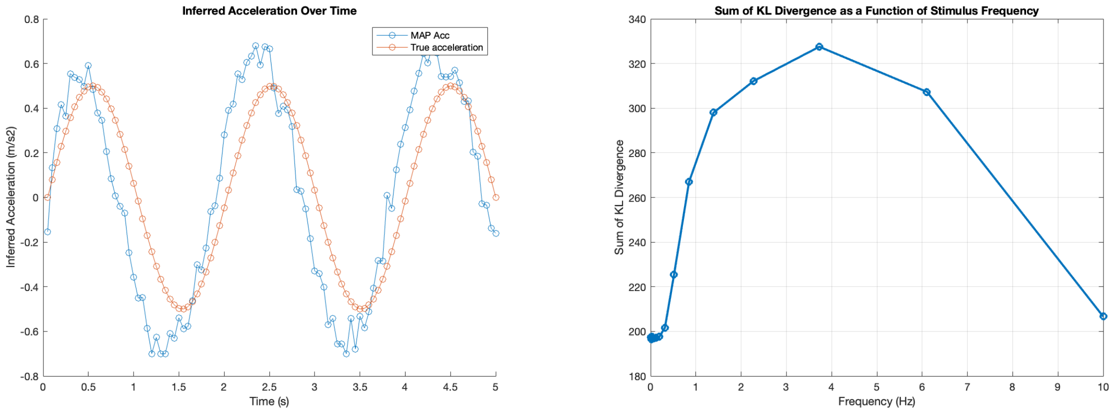

The response of the irregular afferent to a sinusoid of 0.5Hz and an amplitude of 0.5G.

KL Divergence per stimulus frequency of the inference model for the irregular afferent.

Figure 6.17: Model 1.1: irregular afferent responses and KL divergence metrics.

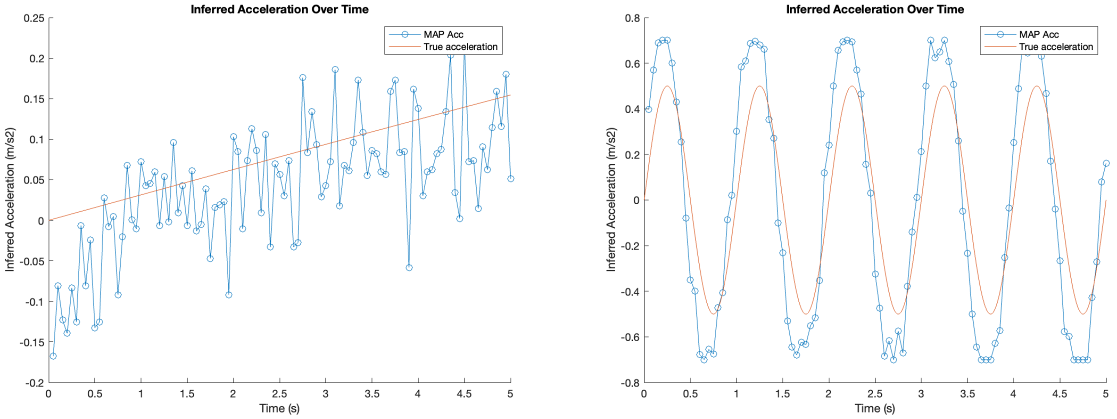

Figure 6.18: Model 1.1: Irregular afferent response to unfiltered low frequency sinusoids. Left: 0.1Hz, Right: 1Hz. Both responses show robust stimuli perception, while not perfectly accurate.

have the same Poisson distribution. However, in reality, their firing rate is distributed differently. We will instead implement a different distribution to account for the difference in firing rate statistics in the two afferent types.

6.4. Model 2

Regular firing + Cosine tuning + LIF Model + Dynamic Gaussian MLE

6.4.1. Distribution assumption, σ=0.1

Instead of assuming a Poisson distribution for the firing rate, we change our approach to assume a Normal distribution for the regular afferents. As indicated by Paulin [78] this should be a valid approach for the regular afferents. A downside to using a Gaussian distribution is that negative input is also accepted, but this should not influence our results since the expected firing rate values are always positive due to the implementation of the sigmoid, just as the spike count cannot be negative. Therefore, it is acceptable to use a Gaussian distribution. Alternatively, we could us the Inverse Gaussian distribution, also known as the Wald distribution. In such a distribution the mean is always positive and it has proven to be able to accurately describe vestibular afferents [78]. For now, we will use a Gaussian distribution.

We assume a standard deviation for the fire rate equal to the CV, as calculated in Chapter 4. For the regular neurons, this means that we will assume $\sigma = 0.1$*FiringRate. Assuming a narrow distribution means that whenever the expected firing rate does not align well with the measured firing rate, the probability of the associated acceleration variable decreases. Thus, only accelerations that match the sensory data well are included. Since the standard deviation is dependent on the firing rate from the sensory data, the values are changing with every step of the inference process.

6.4.2. Window size w

In addition to exploring the impact of stimulus parameters, it is equally important to evaluate the effectiveness of our modeling implementation, particularly with respect to the chosen window size w. The window size w determines the time interval over which sensory data are sampled and subsequently analyzed. Increasing the window size allows for the accumulation of more spikes, effectively increasing the number of ‘data points’ available for our Bayesian inference process. This larger dataset generally leads to more stable and reliable estimates of the neural response, as the increased sample size helps to smooth out the inherent variability in spike trains. Consequently, the model’s predictions become more robust, reducing the impact of random fluctuations and noise in the data.

However, there is a trade-off to consider. As the window size increases, the temporal resolution of our analysis decreases. This reduction in temporal resolution means that the model becomes less sensitive to rapid changes in the stimulus or the corresponding neural responses. In other words, while a larger window size may provide a more stable estimate, it also causes the model to lose its ability to capture fast, transient dynamics in the afferent signals. This loss of temporal fidelity can be particularly problematic when dealing with irregular afferents, which are known for their rapid and precise spike timing. Thus, the choice of window size represents a balance between stability and temporal accuracy. A smaller window size preserves the model’s ability to detect quick changes in the stimulus, but at the cost of increased variability in the computed likelihoods and posteriors. On the other hand, a larger window size reduces this variability, offering a more consistent estimate, but at the expense of the model’s sensitivity to fast temporal changes.

Careful consideration must be given to this trade-off when implementing and evaluating our model. A nuanced understanding of this balance will allow for more informed decisions about the optimal window size, depending on the specific goals of the analysis, whether it be capturing rapid neural responses or achieving stable, long-term predictions.

In the future we could create two parallel models that both have their own time window w, one where it is smaller for the irregular afferents and one that is longer to model the Bayes process for the regular afferents. This aligns with our approach in determining discrimination performance between the regular and irregular afferents in section 5.3.7.

6.4.3. Motion Perception validation

We begin by validating the model's capability to accurately estimate sinusoidal vertical accelerations across a wide range of frequencies and amplitudes, specifically from 0 to 15 Hz and 0 to 1G. This initial step is important in establishing the model's sensitivity and reliability in simulating the vestibular system's response to varying motion stimuli.

We systematically test the model against these parameters to ensure it can handle both low and high-frequency oscillations, as well as subtle to intense gravitational forces. By doing so, we assess whether the model can maintain accuracy across the full spectrum of conditions typically encountered in real-world scenarios. This validation process also serves to identify any potential limitations or areas for further refinement, ensuring the model's robustness in predicting motion perception.

6.4.4. Motion Sickness prediction

Next, we validate the model's ability to predict motion sickness across the same range of stimuli. This involves a comparison of the model's predictions against experimental data, particularly focusing on its sensitivity to variations in frequency and amplitude, as seen in Figure 6.20. While capturing the sickness prediction results, we also take random snapshots of how the model is performing visually. In Figure 6.19 we can see that the model operates well in most situations, but there are still paradigms where the model struggles to create an accurate estimation.

To see what the influence of the standard deviation of the Gaussian distribution is in the likelihood estimation, we have increased the value from 0.1 to 0.2 to validate if the model is more stable using a larger 'uncertainty' value.

If we research the estimation graphs better, we can see that there are some anomalies that cause wrong acceleration estimates. When we look at the dashboard that was made for trouble shooting we can see in Figure 6.22 that there is no likelihood for certain timesteps. This is caused by numerical instabilities. Some of them were solved by using Log-Likelihood instead of Likelihood before. The issues in this model are due to the lack of firing causing a column in a matrix in the likelihood calculation to become "NaN". Even though a very small *eps* value was added before, the calculation was still unstable. By increasing *eps* to a baseline value of 0.5 for the regular and the irregular to the standard deviation ($\sigma_{\text{Gauss}} * \text{FiringRate}$, nominal value around) of the sensory data distribution the system becomes stable again. This has negligible influence on the outcome and has empirically been tested to be the lowest range to apply.

6.4.5. Motion Sickness validation

We validate the model and its different parameters to the data from O'Hanlon and McCauley [49].

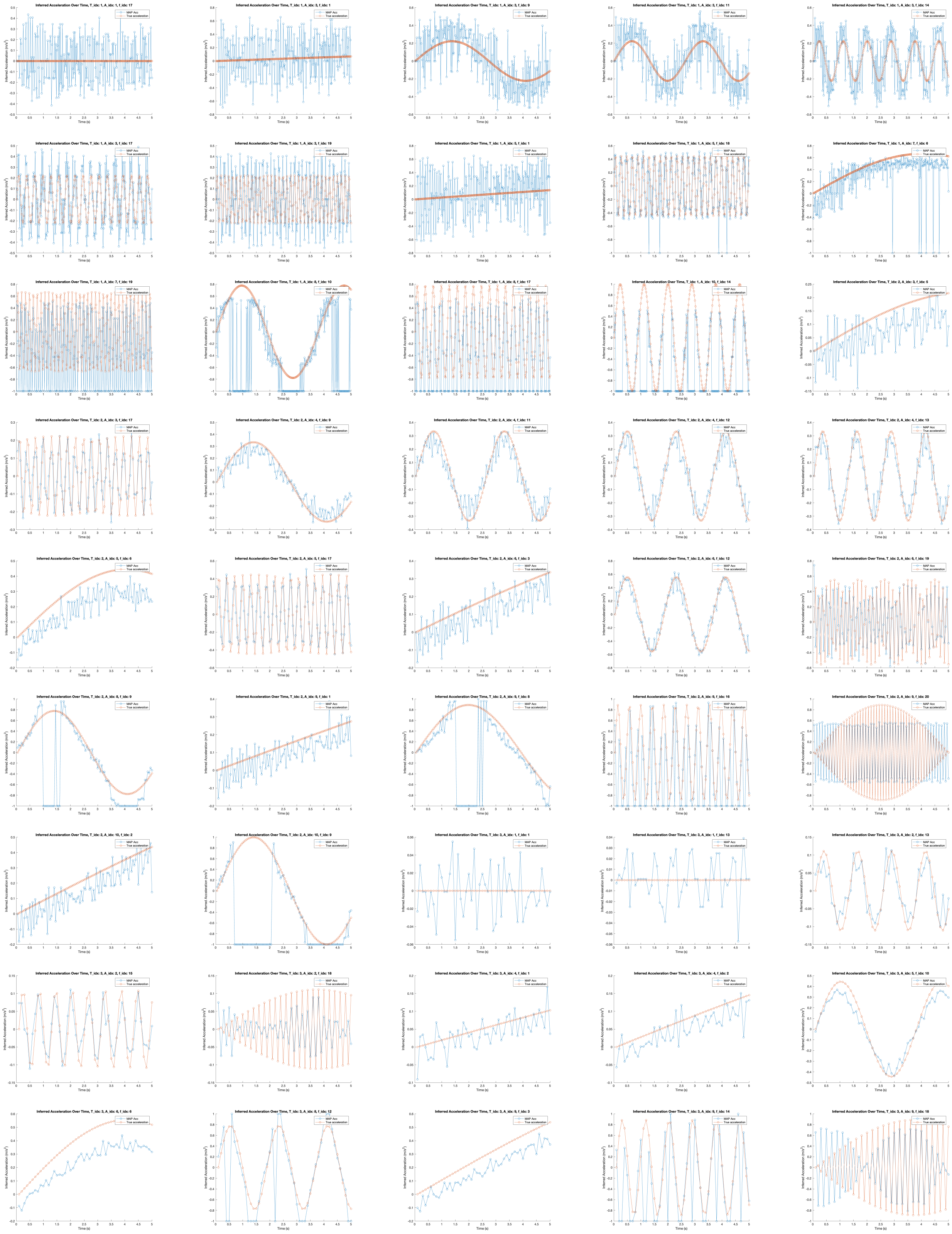

Inferred Acceleration Over Time, T_idx: 1, A_idx: 1, f_idx: 17
Inferred Acceleration Over Time, T_idx: 1, A_idx: 3, f_idx: 1
Inferred Acceleration Over Time, T_idx: 1, A_idx: 3, f_idx: 9
Inferred Acceleration Over Time, T_idx: 1, A_idx: 3, f_idx: 11
Inferred Acceleration Over Time, T_idx: 1, A_idx: 3, f_idx: 14
Inferred Acceleration Over Time, T_idx: 1, A_idx: 3, f_idx: 17
Inferred Acceleration Over Time, T_idx: 1, A_idx: 3, f_idx: 19
Inferred Acceleration Over Time, T_idx: 1, A_idx: 5, f_idx: 1
Inferred Acceleration Over Time, T_idx: 1, A_idx: 5, f_idx: 18
Inferred Acceleration Over Time, T_idx: 1, A_idx: 7, f_idx: 6
Inferred Acceleration Over Time, T_idx: 1, A_idx: 7, f_idx: 19
Inferred Acceleration Over Time, T_idx: 1, A_idx: 8, f_idx: 10
Inferred Acceleration Over Time, T_idx: 1, A_idx: 8, f_idx: 17
Inferred Acceleration Over Time, T_idx: 1, A_idx: 10, f_idx: 14
Inferred Acceleration Over Time, T_idx: 2, A_idx: 3, f_idx: 5
Inferred Acceleration Over Time, T_idx: 2, A_idx: 3, f_idx: 17
Inferred Acceleration Over Time, T_idx: 2, A_idx: 4, f_idx: 9
Inferred Acceleration Over Time, T_idx: 2, A_idx: 4, f_idx: 11
Inferred Acceleration Over Time, T_idx: 2, A_idx: 4, f_idx: 12
Inferred Acceleration Over Time, T_idx: 2, A_idx: 4, f_idx: 13
Inferred Acceleration Over Time, T_idx: 2, A_idx: 5, f_idx: 6
Inferred Acceleration Over Time, T_idx: 2, A_idx: 5, f_idx: 17
Inferred Acceleration Over Time, T_idx: 2, A_idx: 6, f_idx: 3
Inferred Acceleration Over Time, T_idx: 2, A_idx: 6, f_idx: 12
Inferred Acceleration Over Time, T_idx: 2, A_idx: 6, f_idx: 19
Inferred Acceleration Over Time, T_idx: 2, A_idx: 8, f_idx: 9
Inferred Acceleration Over Time, T_idx: 2, A_idx: 9, f_idx: 1
Inferred Acceleration Over Time, T_idx: 2, A_idx: 9, f_idx: 8
Inferred Acceleration Over Time, T_idx: 2, A_idx: 9, f_idx: 16
Inferred Acceleration Over Time, T_idx: 2, A_idx: 9, f_idx: 20
Inferred Acceleration Over Time, T_idx: 2, A_idx: 10, f_idx: 2
Inferred Acceleration Over Time, T_idx: 2, A_idx: 10, f_idx: 9
Inferred Acceleration Over Time, T_idx: 3, A_idx: 1, f_idx: 1
Inferred Acceleration Over Time, T_idx: 3, A_idx: 1, f_idx: 13
Inferred Acceleration Over Time, T_idx: 3, A_idx: 2, f_idx: 13
Inferred Acceleration Over Time, T_idx: 3, A_idx: 2, f_idx: 15
Inferred Acceleration Over Time, T_idx: 3, A_idx: 2, f_idx: 18
Inferred Acceleration Over Time, T_idx: 3, A_idx: 4, f_idx: 1
Inferred Acceleration Over Time, T_idx: 3, A_idx: 4, f_idx: 2
Inferred Acceleration Over Time, T_idx: 3, A_idx: 5, f_idx: 10
Inferred Acceleration Over Time, T_idx: 3, A_idx: 6, f_idx: 6
Inferred Acceleration Over Time, T_idx: 3, A_idx: 8, f_idx: 12
Inferred Acceleration Over Time, T_idx: 3, A_idx: 9, f_idx: 3
Inferred Acceleration Over Time, T_idx: 3, A_idx: 9, f_idx: 14
Inferred Acceleration Over Time, T_idx: 3, A_idx: 9, f_idx: 18

Figure 6.19: Model 2: Using sigma = 0.1: Samples of the perception results when varying the amplitude, frequency and window size. We randomly produced results with a probability of once every ten runs. Most perception results look accurate, while others seem to show large deviations in their estimates compared to the original stimulus.

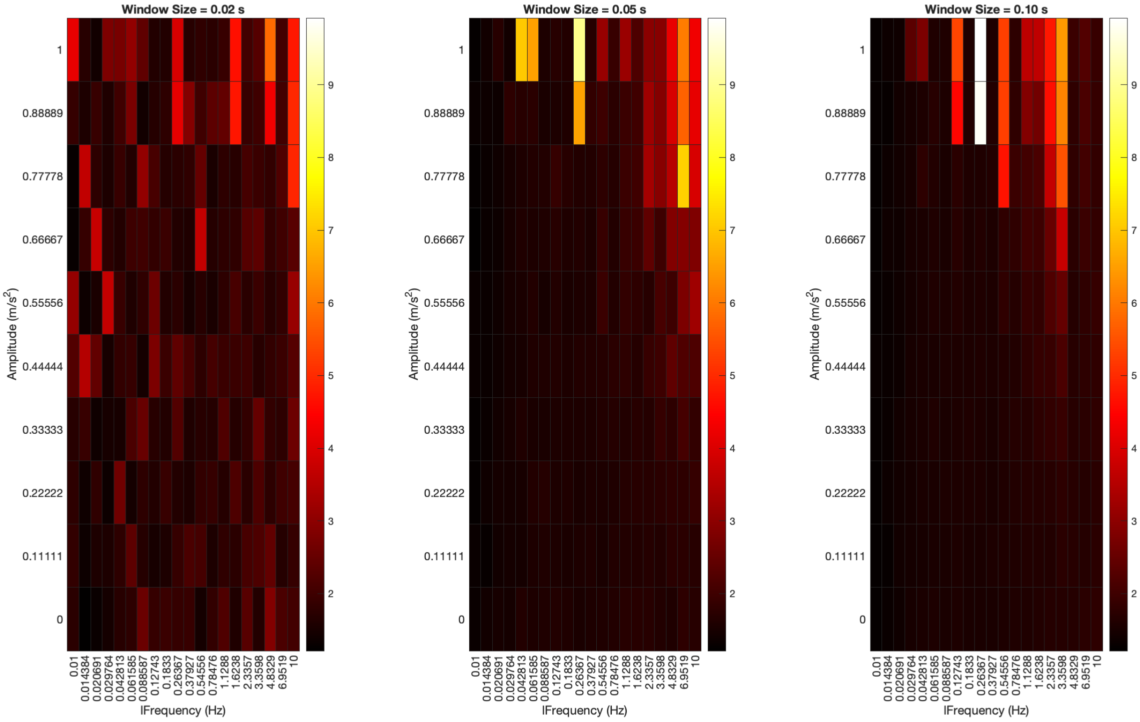

Figure 6.20: Model 2: Average KL Divergence as a result of amplitude and frequency. Varying the window size w. We observe that the frequency dependency changes with the window size. The amplitude dependency seems to be similar across different values of w.

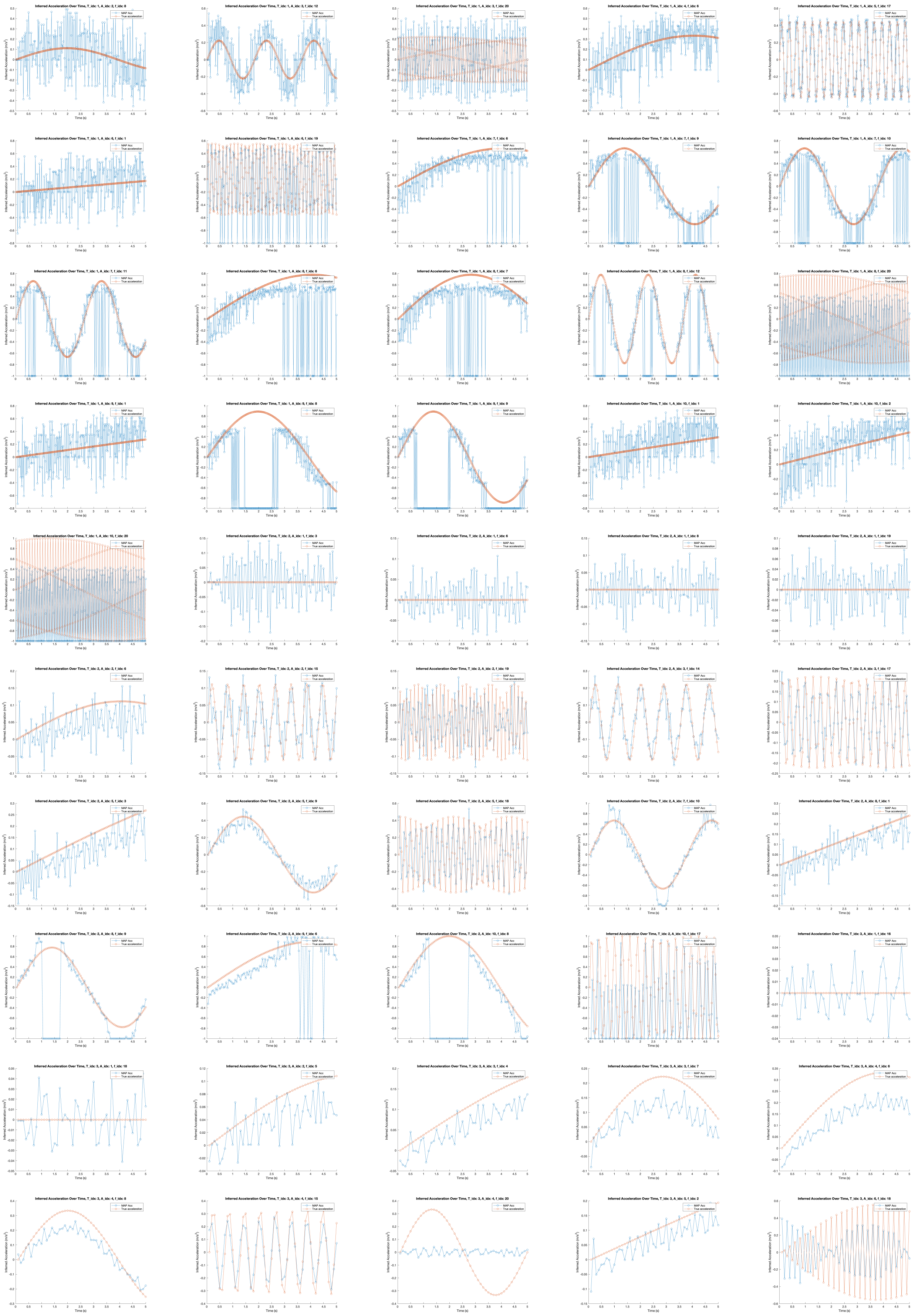

Figure 6.21: Model 2: Using sigma = 0.2: Samples of the perception results when varying the amplitude, frequency and window size. We randomly produced results with a probability 0.1, resulting in a result once every ten runs. Most perception results look accurate, while others seem to show large deviations in their estimates compared to the original stimulus. We can see the model struggles primarily with the peaks of the sinusoids, when the spike rate of opposite tuned neurons decreases.

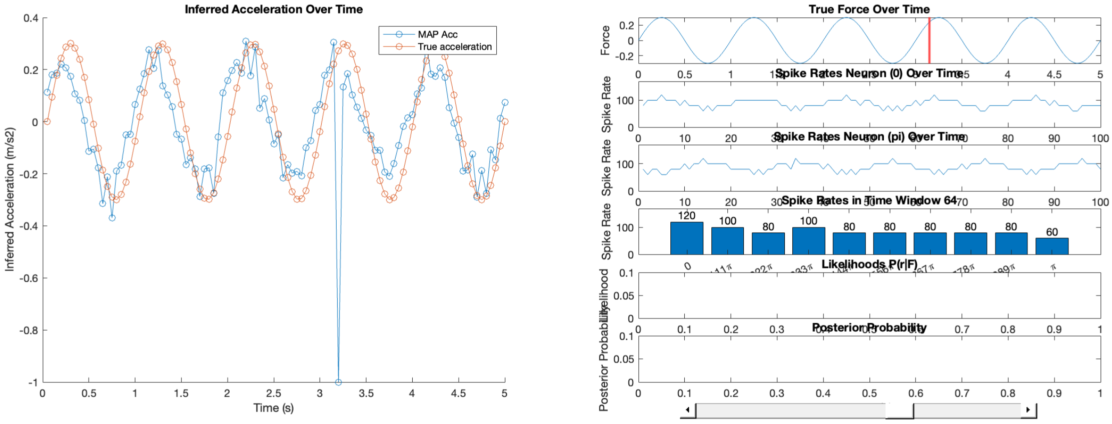

(a) Acceleration and estimated acceleration over time. An anomaly can be seen around timestamp 3.2s.

(b) Dashboard that shows from top to bottom: the true acceleration/force, the spike rates for the first and second neuron during all time steps, the spike rates at timestep t, the likelihood during t and the Posterior during t. By moving the slider you can see the model's different states over time.

Figure 6.22: Model 2: Troubleshooting the model. The likelihood function is invalid at time step ±3.3s, which results in a wrong acceleration estimate. On the right we can select the timestep and investigate different states of the model.

6.5. Model 3

Regular + Irregular + Cosine tuning + LIF Model + Dynamic Normal MLE

In this model we implement both regular and irregular afferents. Still, the afferents have a dynamic normal distribution which should favor the regular afferents at similar firing rates due to their lower standard deviation.

When combining regular and irregular afferents in our model, the assumption is that this integration enhances performance due to evolutionary optimization. Evolution likely shaped these afferent types to work together, providing an optimal balance between sensitivity, energy efficiency, and stability (homeostasis). The reduced sensitivity to low-frequency motions may be a deliberate energy-saving adaptation, reflecting the lack of such motions in everyday life. The increased inaccuracy to high-amplitude motions may be an intentional energy-conservation strategy as well, recognizing that these conditions are relatively rare in normal daily activities as also hypothesised by Schneider et al.[85] in their argumentation for the optimal sensory distribution curves.

Regular afferents, with their stable, low-variance responses, may ensure consistent baseline performance, while irregular afferents, with their heightened sensitivity to changes, could offer rapid adaptation and response to dynamic stimuli. This dual-system approach likely supports efficient and robust motion perception. Further, the balance between these two types of afferents may also be critical for maintaining energy efficiency, as irregular afferents might require more metabolic resources, but their selective activation during dynamic events could optimize the overall energy expenditure of the system. We also know that irregular afferents utilize non-quantal spike transmission, which compensates for the cost of responsiveness[76].
By integrating both afferent types, the model likely reflects the evolutionary pressures that shaped the vestibular system to be both responsive and efficient, providing robust motion perception even in complex and variable environments. This combined system should not only enhance the accuracy of motion perception but also ensures that the system remains energy-efficient. We note that energy efficiency might explain the shortcomings of the inference. However, we will not quantify this in this thesis.

What we will quantify is the accuracy of the perception and the measure of 'surprisal'. According to Friston's free energy principle [28], biological systems, including the brain, aim to minimize "free energy", which is a measure of the difference between expected and actual sensory inputs. In terms of energy efficiency, the brain minimizes 'surprisal' by reducing uncertainty and aligning predictions with actual outcomes. This efficient prediction process conserves energy by avoiding unnecessary adjustment in response to environmental stimuli, like overcompensating while balancing in the context of the vestibular system.
Thus, the maximum KL divergence peaks that we measure should be a result of energy conservation due to these low-frequency motions not being prevalent in daily life.

6.5.1. Motion Perception

In Figure 6.24, we observe that the model estimates acceleration with high accuracy in low-frequency paradigms. This indicates that the model's inference process effectively captures the neural response to lower frequency motion stimuli, where the dynamics of the system are more easily tracked and interpreted. However, as the frequency increases beyond 10 Hz, the accuracy of the inference process diminishes, and the model's sensitivity decreases. This decline in performance at higher frequencies can be attributed to several factors. First, the rapid fluctuations in neural firing patterns at high frequencies may not be fully captured by the model, especially if the window size used for processing the spike data is not optimally tuned to these fast dynamics. In high-frequency conditions, the model struggles to maintain the temporal resolution needed to track rapid changes in acceleration, leading to less accurate estimations.

6.5.2. Motion Sickness

In Figure 6.23, we observe that the average KL Divergence increases when the window size is set to a smaller value of 0.02 s. This increase can be attributed to the loss of ‘firing rate’ resolution as the window size decreases. With a smaller window, fewer spikes are counted, leading to higher variance in the spike counts. This increased variance reflects the greater sensitivity of the model to instantaneous fluctuations in neural firing, which is a direct consequence of the reduced averaging over time.

When larger windows are used, spike counts are averaged over a longer period, which smooths out these fluctuations, resulting in lower variance. This averaging effect reduces the temporal resolution, meaning the model becomes less sensitive to rapid changes in neural activity. However, in the context of this simulation, the higher temporal resolution afforded by smaller windows appears to capture more detailed information about the firing patterns, especially at higher frequencies of motion. Interestingly, the average KL Divergence for high-frequency motion is significantly higher with the smaller window size compared to larger window sizes. Smaller windows are more effective in detecting subtle changes in neural firing patterns that occur in response to high-frequency stimuli. On the other hand, larger windows may miss these nuances due to the averaging effect, potentially leading to an underestimation of the neural response to high-frequency motion. There seems to be a trade-off between temporal resolution and firing rate resolution. This highlights the importance of an appropriate window size.

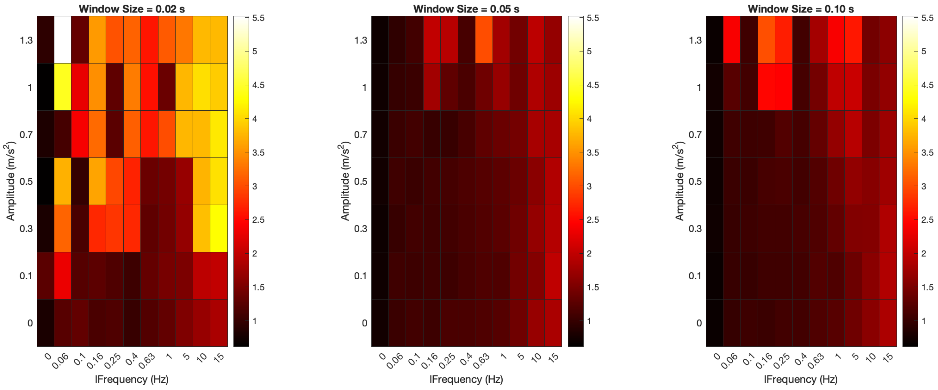

Figure 6.23: Model 3: Results of combined model of regular and irregular otolith afferents. The low KL divergence when there is no motion is to be expected, since we do not get motion sick during static situations. The amplitude dependency is also expected due to saturations in the firing rate.

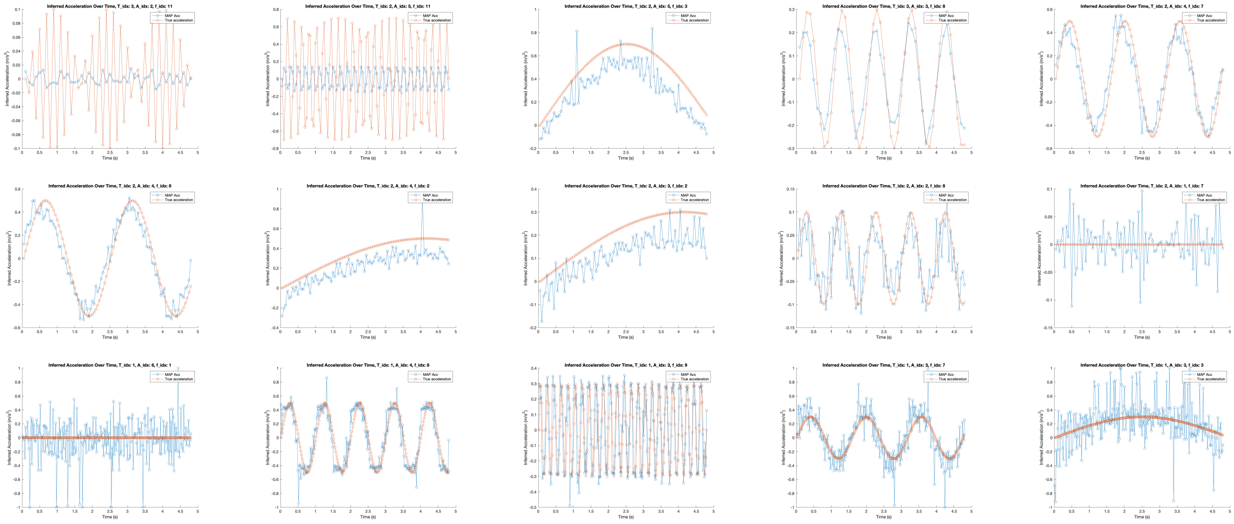

Figure 6.24: Model 3: Perception results of combined model of regular and irregular otolith afferents for different values of amplitude, frequency and w.

6.6. Model 4

Regular + Irregular + Cosine tuning + LIF Model + Dynamic Normal MLE + Prior based on Posterior

A change in the prior allows the model greater flexibility in shaping distributions. Previously, the prior was based on a Gaussian distribution, but it is now derived from the posterior's shape. We introduce a parameter α, which can be tuned to control the weight of the update process. Initially it is set to 0.1. α essentially tunes how much the model updates its belief (prior) based on new evidence (posterior). A small α results in a more gradual update, while a large α leads to a more aggressive update based on the new data. By choosing $\alpha = 0.5$, the model maintains stability and avoids drastic changes in the prior, which is particularly useful in scenarios where the new data may be noisy or uncertain as it is in the otolith system. This approach ensures that the model's prior beliefs are adjusted cautiously, reducing the risk of overfitting to new, potentially unrepresentative data, and maintaining a balance between incorporating new information and retaining current understanding. We hypothesise that this parameter could change the models behaviour regarding frequency and amplitude response, because at high frequencies and amplitudes the model might struggle to update fast enough when a is defined as a low value.

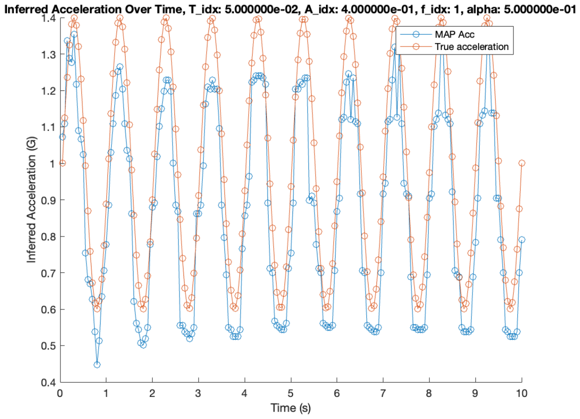

Figure 6.25: Model 4: An alpha of 0.5 strikes a good balance between incorporating new information and retaining current understanding.

In previous configurations, we varied the distribution of hair cells (neurons) across the semicircle to capture different orientations. However, we have not yet increased the number of hair cells aligned in the 'parallel' direction. To do this, we multiply the existing row of neurons by a factor 'NumParallel,' which results in a larger population of identically tuned hair cells with similar stochastic behavior. This approach introduces redundancy, thereby reducing the impact of variability and noise, and could also improve the model's sensitivity to small perturbations in the input stimuli. However, this modification comes with trade-offs, including increased computational demands and potentially higher energy consumption in a biological context.

To assess the effects of this change, we increased the number of parallel neurons from 1 to 10. This modification resulted in a reduction in the average RMS error from 0.2089 G to 0.20419 G, indicating a 2.3% improvement in accuracy. While this is a positive outcome, the marginal improvement raises questions about the efficiency of increasing the number of identically tuned neurons. This suggests that either the current implementation is not fully optimized to take advantage of the added redundancy, or that beyond a certain point, adding more neurons offers diminishing returns in terms of accuracy.

7

Results from Final Model

Using Model 5, the most developed realisation, we will gather results on the models behaviour. We have defined the following parameters as important for the tuning and evaluation of the model:

- The standard duration is set to 10 seconds to capture a full sinusoidal loop.
- The inference time window is matched to Nyquist–Shannon sampling theorem of 1/(2*B), which mean we require a sampling of at least $1/20 = 0.05$ seconds for a 10Hz frequency. We are mostly interested in the 0-1 Hz region.
- The numbers of neurons is set to 10, since this gives us smooth enough results, while not being too computationally expensive.
- The number of parallel neurons is set to 1, since increasing this would result in too much computational capacity.
- The σ_{Gauss} has a value of 1, a higher value indicates more weight put onto new measurements.
- The σ_{Regular} and $\sigma_{\text{Irregular}}$ are divided by the firing rate of the regular and, respectively, irregular afferents, to match experimental results [26][85]. Their values approximate the actual width of their distributions.
- The Searchwidth limits the search area for accelerations.
- The SearchResolution determines how much values for acceleration are considered.
- The dt determines the resolution of the sensory data, it is a parameter for the spike encoding model. This value is needed to accurately describe hyperpolarization, both in the Hodgkin-Huxley and the Leaky-Integrate-and-Fire model.
- The prior update factor α maintains stability and avoids drastic changes in the prior.

Table 7.1: Parameters used for experiments and their default values. Assume defaults are used unless stated otherwise.

Parameter	Value	Description
Frequency	2 Hz	Sinusoidal motion frequency
Amplitude	0.5 G	Sinusoidal motion amplitude
Gravity	1 G	Constant force
Duration	10 s	Duration of the exposure
Window w	0.05 s	Length of inference time window
nNeurons	10	Number of neurons on Z-curve
nParallel	1	Number of neurons in parallel, see Figure 7.6.
σ_{Gauss}	1	Standard deviation prior
σ_{Regular}	500/FiringRate	Standard deviation regular distribution
$\sigma_{\text{Irregular}}$	1200/FiringRate	Standard deviation irregular distribution
Searchwidth	3 G	Maximum and minimum sampled acceleration
SearchResolution	1000	Number of samples of acceleration
Time-step dt	0.025 ms	Length of sensory data time-step
α	0.5	Balances updating prior with new information

7.1. Experiment 1: Minimal Model - Increasing Neuron Count

Purpose:
The primary aim of this experiment is to evaluate the performance of the model in its most minimal configuration, beginning with just two neurons. The experiment then explores the impact of progressively increasing the number of neurons to determine how this affects the model's stability and accuracy in estimating the neural responses.

Table 7.2: Parameters used for experiment 1.

Parameter	Value	Description
Frequency	1 Hz	Sinusoidal motion frequency
Amplitude	0.5 G	Sinusoidal motion amplitude
Gravity	0 G	Constant force
nNeurons	2:10:50:100	Number of neurons on Z-curve
σ_{Regular}	1000/(FiringRate+1)	Standard deviation regular distribution
$\sigma_{\text{Irregular}}$	2500/(FiringRate+1)	Standard deviation irregular distribution

Conclusions:

- The model remains functional even with a minimal setup of only two opposite neurons. However, as the number of neurons increases, the variability of the estimation improves, which is evidenced by the increased smoothness of the resulting estimates. This is clear when comparing the smoothness in the peaks in Figure 7.1 and Figure 7.3.
- The performance of estimation does not seem to vary.
- As the number of neurons reaches a high count, 100 neurons in this particular instance, the model begins to exhibit instability. This instability arises due to the compounded multiplication of a large number of likelihoods, many of which are close to zero, leading to numerical instability in the combined likelihood estimate.
- To mitigate this issue, an increase in the standard deviation parameter is effective. This adjustment helps maintain numerical stability while maintaining the overall accuracy of the model.

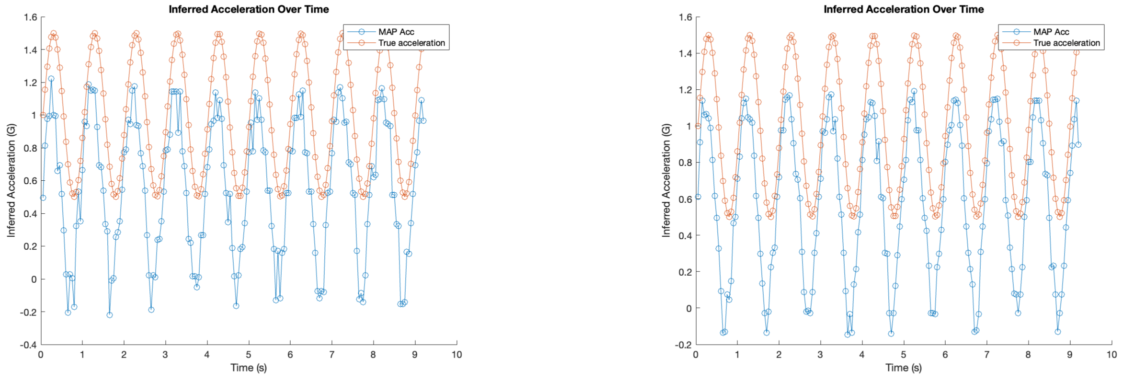

Figure 7.1: nNeurons = 2

Figure 7.2: nNeurons = 10

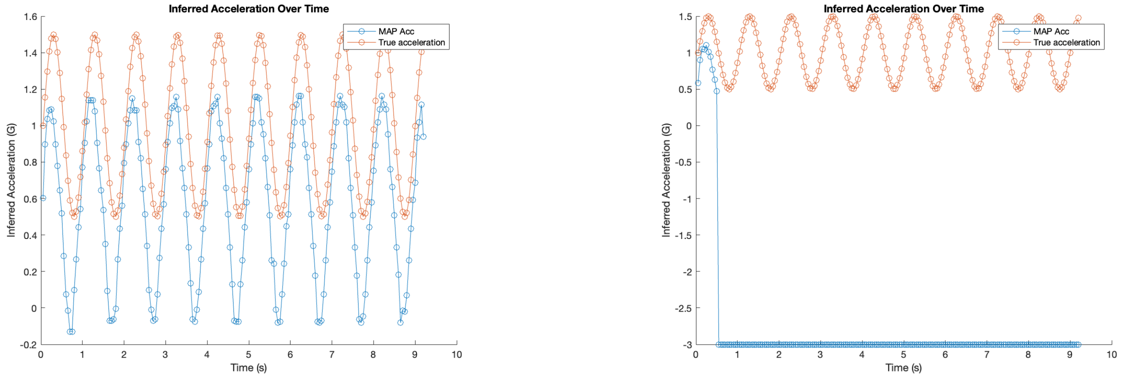

Figure 7.3: nNeurons = 50

Figure 7.4: nNeurons = 100

Figure 7.5: Experiment 1: Influence of altering the number of neurons on acceleration estimation.

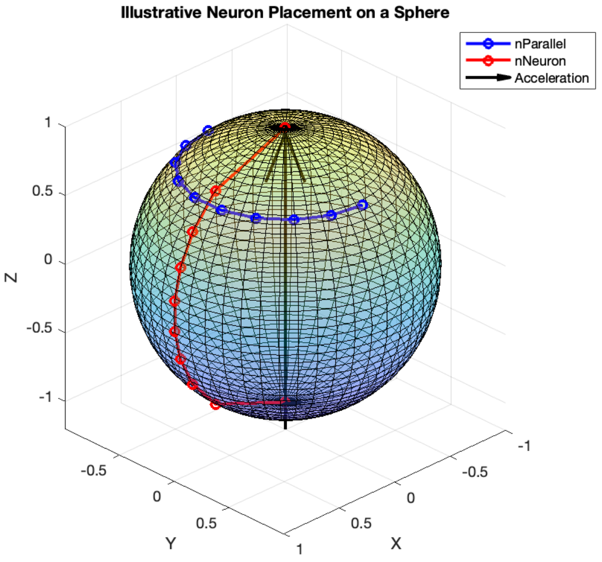

Figure 7.6: Illustration of the direction in which the parameters nParallel and nNeurons act. While the otoliths are not formed like a perfect sphere, the preferred directions of individual afferents can be assumed as such [60]. In our experimental setup we could also consider the shape of the hair cell tuning to be a half cylinder.

7.2. Experiment 2: Analyzing KL Divergence Between Regular and Irregular Afferents.

Purpose:
The main goal of this analysis is to see how the likelihoods of regular and irregular afferents change over a 10-second period when exposed to different types of stimuli. By looking at these differences, we hope to better understand the specific roles that regular and irregular afferents play in processing sensory information. This comparison will help us learn how these two types of afferents affect the overall neural response to different motion conditions, which could be important for improving the model's accuracy and stability. Additionally, this analysis will show how the timing of these likelihoods influences the model's predictions, especially in situations with different frequencies and intensities of stimuli.

Table 7.3: Parameters used for experiment 2.

Parameter	Value	Description
σ_{Regular}	500/FR	Standard deviation regular distribution
$\sigma_{\text{Irregular}}$	1200/FR	Standard deviation irregular distribution

Conclusions:

- The results show a steady increase in KL Divergence as the frequency increases. This trend suggests that the differing dynamics between regular and irregular afferents become more pronounced at higher frequencies. Irregular afferents, being better at tracking high-frequency acceleration, exhibit likelihoods that diverge more from those of regular afferents as frequency rises.
- When the amplitude of the motion is varied, the distributions do not show a significant increase in distance. This indicates that changes in amplitude have minimal impact on the differences between the likelihoods of regular and irregular afferents.
- After analyzing the average KL Divergence between regular and irregular afferents across various experiments, we observe that this trend is consistently present in the model. This confirms that frequency plays an important role in how these afferents behave differently.

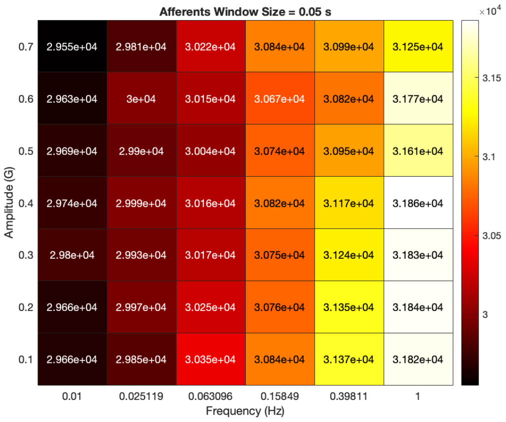

Amplitude (G)	0.01	0.025119	0.063096	0.15849	0.39811	1
0.7	2.955e+04	2.981e+04	3.022e+04	3.084e+04	3.099e+04	3.125e+04
0.6	2.963e+04	3e+04	3.015e+04	3.067e+04	3.082e+04	3.177e+04
0.5	2.969e+04	2.99e+04	3.004e+04	3.074e+04	3.095e+04	3.161e+04
0.4	2.974e+04	2.999e+04	3.016e+04	3.082e+04	3.117e+04	3.186e+04
0.3	2.98e+04	2.993e+04	3.017e+04	3.075e+04	3.124e+04	3.183e+04
0.2	2.966e+04	2.997e+04	3.025e+04	3.076e+04	3.135e+04	3.184e+04
0.1	2.966e+04	2.985e+04	3.035e+04	3.084e+04	3.137e+04	3.182e+04

Figure 7.7: Experiment 2: Average KL Divergence over 10 seconds between regular and irregular afferents.

7.3. Experiment 3: No Acceleration (Static 1G).

Purpose:
The goal of this experiment is to visually examine how the distributions of regular and irregular afferents differ when no motion is applied, specifically under static 1G conditions.

Table 7.4: Parameters used for experiment 3.

Parameter	Value	Description
Frequency	0 Hz	Sinusoidal motion frequency
Amplitude	0 G	Sinusoidal motion amplitude
LIF tuning	3.62 nA, 0.33	I_{Bias} and Sensitivity

Conclusions:

- The distributions at 1G show a "battle," resulting in a bimodal posterior distribution, indicating two competing states in the model's output.
- The model was originally tuned for 0G, making it less accurate at 1G. This mismatch leads to a significant bias in the difference between the expected and actual firing rates.
- Under static 1G conditions, the model's estimation shows an RMS Error of 0.30909 G compared to the original stimulus.
- After retuning the firing rate encoding model, the bias was reduced, and the RMS Error improved to 0.17759 G, showing better alignment with the actual conditions.
- This retuning also resulted in a significant improvement in the accuracy of the model's static estimates under gravity alone, reducing the bias and error in the output.
- After retuning, the responses of regular and irregular afferents became more synchronized, which means the model is now more coherent.
- The irregular afferents continued to show a broader distribution. The inference process assigns less weight to the irregular afferent when estimating under static 1G conditions, reflecting a more accurate model response. This is the behaviour we would expect based on [48].

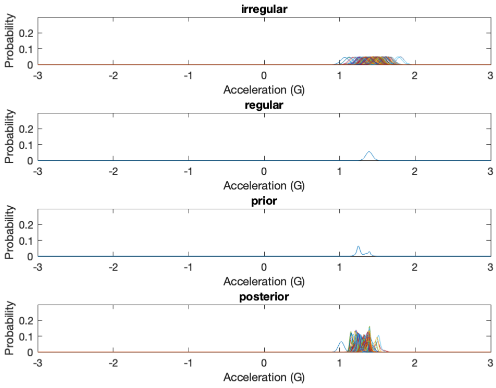

Figure 7.8: Experiment 3: No acceleration input, only gravity. We can see a bimodal posterior distribution appear due to the combined likelihood of the regular and irregular afferents.

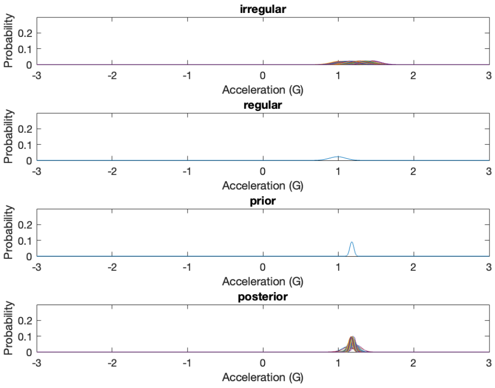

Figure 7.9: Experiment 3: No acceleration input, only gravity. After retuning the model, the estimation under static conditions has significantly improved. The regular and irregular afferents now show better alignment, with the irregular afferent exhibiting a wider distribution.

7.4. Experiment 4: Evaluating acceleration and MS performance.

Purpose:
Following the adjustments made to the Leaky Integrate-and-Fire model, it is important to reassess the model's performance in estimating acceleration and predicting motion sickness. This experiment aims to validate the model's accuracy across a range of frequencies and amplitudes, particularly focusing on the RMS error and average KL divergence.

Conclusions:

- The model performs acceleration estimation reliably and accurately at low frequencies, at high frequencies the RMS error goes up. This is in line with what is known about human perception, since perception to accelerations seems to be insensitive at high frequencies [87].
- The average KL Divergence reaches its peak at a frequency of 2.5 Hz and continues to increase as the amplitude of the motion grows. This suggests that the model becomes less confident or more varied in its estimations as the motion's intensity increases, particularly around this frequency.
- The findings reinforce the model's alignment with known human perceptual characteristics, confirming that it can replicate the decrease in sensitivity to high-frequency stimuli observed in human subjects.
- The increasing KL Divergence with amplitude highlights the importance of considering both frequency and amplitude when assessing motion sickness risk. The model's ability to capture these dynamics suggests it could be useful in practical applications, such as designing systems to minimize motion sickness.
- The frequency where the average KL Divergence peaks is not completely in line with current data on vertical motion sickness, which suggests a peak around 0.17 Hz [49].
- As can be seen in Figure 7.15, looking at the figure in the middle, when increasing the measuring resolution the results are similar to 7.13. This indicates low variability between trials for this experiment.
- To validate our results, we need to explore a wider range of parameter combinations to determine the factors that influence the sensitivity of KL Divergence to frequency and amplitude. To achieve this, we plan to run additional simulations on a computer with greater computational capacity.

Table 7.5: Parameters used for experiment 4.

Parameter	Value	Description
Frequency	0:100 Hz	Sinusoidal motion frequency
Amplitude	0:0.7 G	Sinusoidal motion amplitude

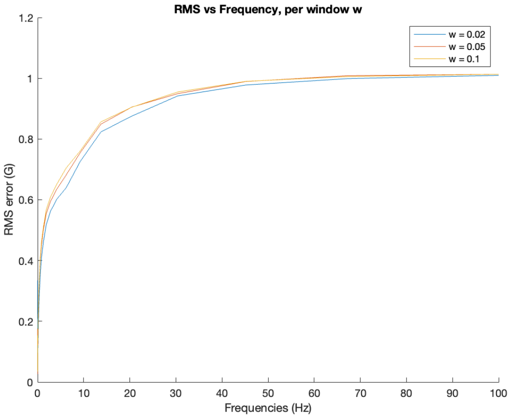

Figure 7.10: Experiment 4: Validating RMS performance for every frequency at an amplitude of 0.4G. At low frequencies the perception performance is accurate, while at high frequencies it is not.

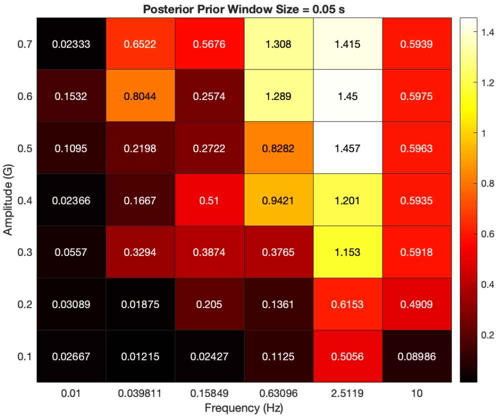

Amplitude (G) \ Frequency (Hz)	0.01	0.039811	0.15849	0.63096	2.5119	10
0.7	0.02333	0.6522	0.5676	1.308	1.415	0.5939
0.6	0.1532	0.8044	0.2574	1.289	1.45	0.5975
0.5	0.1095	0.2198	0.2722	0.8282	1.457	0.5963
0.4	0.02366	0.1667	0.51	0.9421	1.201	0.5935
0.3	0.0557	0.3294	0.3874	0.3765	1.153	0.5918
0.2	0.03089	0.01875	0.205	0.1361	0.6153	0.4909
0.1	0.02667	0.01215	0.02427	0.1125	0.5056	0.08986

Figure 7.11: Experiment 4: Average KL Divergence for sinusoids at different amplitudes and frequencies.

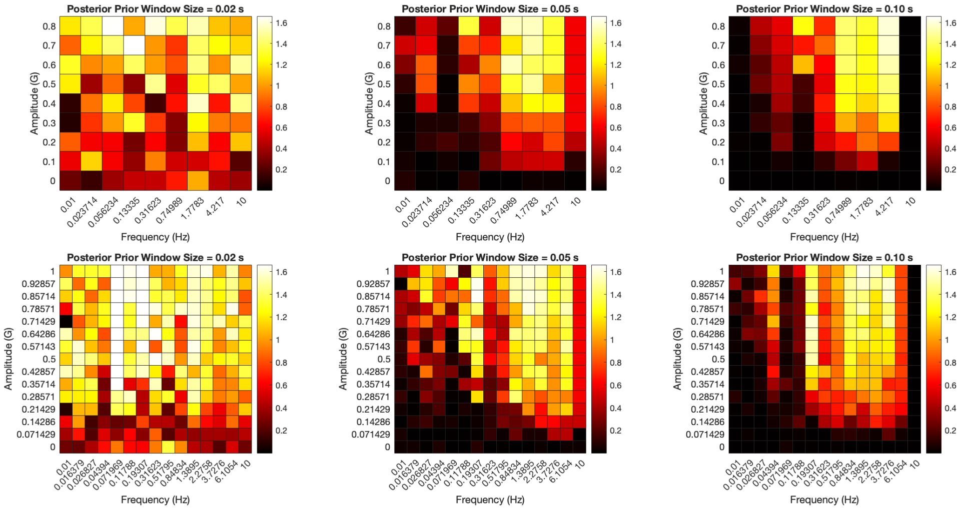

Figure 7.12: Experiment 4: Average KL Divergence for sinusoids at different amplitudes, frequencies and time windows w. Measured with a different ranges and parameter resolutions to verify variability between trials.

7.5. Experiment 5: Evaluating Perception Sensitivity.

Purpose:
The goal of this experiment is to evaluate whether the model's sensitivity to motion aligns with empirical perception data reported by Soyka et al.[87]. To achieve this, we will generate a Gain vs. Frequency plot, where the gain is calculated as the difference between the maximum and minimum estimated acceleration, normalized by the stimulus amplitude. This method allows us to assess the model's accuracy in replicating human perceptual responses across different frequencies and provides a comparison with established empirical data.

Table 7.6: Parameters used for experiment 5.

Parameter	Value	Description
Amplitude	0.4 G	Sinusoidal motion amplitude

Conclusions:

- The model's frequency sensitivity response closely matches empirical perceptual data, even without any specific tuning. This suggests that the model inherently captures the key dynamics of human motion perception.
- A time window of 0.10 s for w produces results that align well with the data reported by Soyka et al. [87], while a shorter window of 0.02 s aligns more closely with the findings from Young et al.[97] and Telban et al.[91].
- The sensitivity of the model decreases as the frequency increases, which is consistent with the results of multiple studies [87, 39, 91]. This reflects a common characteristic of human motion perception, where higher frequencies are associated with reduced sensitivity.
- The perception results obtained from the model follow the expected trend, where sensitivity diminishes with increasing frequency. This trend has been well-documented in the literature and is supported by the data from various studies.
- The generated otolith transfer function (Equation 1) illustrates how the sensitivity of otoliths decreases with frequency, aligning well with both the model's output and empirical data. This supports the validity of the model in simulating real-world perceptual dynamics.
- Interestingly, previous research has indicated that thresholds for detecting motion are higher for upright vertical movements compared to horizontal movement [5, 50]. It would be valuable to further explore how these differences influence the frequency response in future experiments, potentially refining the model to account for these variations.
- Some unexpected anomalies were observed in the measurements at high frequencies for $w = 0.02$ s and $w = 0.05$ s. The cause is not yet known.

The perception result shows a decrease in sensitivity as frequency increases, in line with the findings from Soyka et al. (2011) and others [87, 39, 91]. The parameters from each study were used to create a transfer function of the form [69]:

$$H_{\text{oto}}(s) = K_{\text{oto}} \times \frac{(1 + T_{\text{oto1}} s)}{(1 + T_{\text{oto2}} s)(1 + T_{\text{oto3}} s)} \tag{7.1}$$

As shown in Figure 7.14, the sensitivity of otoliths decreases as frequency increases. This outcome is based on human perception experiments and aligns well with our model's data. This agreement reinforces the model's accuracy in simulating the dynamics of human motion perception. Considering the higher thresholds for vertical movements, as identified in previous research [5, 50], further investigation into how these differences affect frequency response would be beneficial.

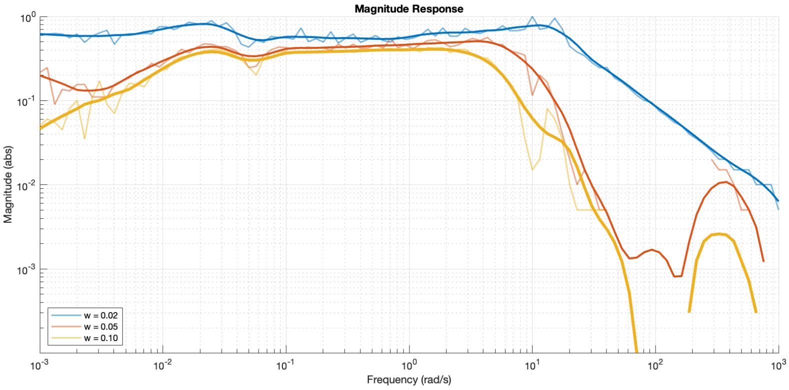

Figure 7.13: Experiment 5: Normalized gain vs frequency for a 0.4G sinusoid. Different window sizes w are shown. Please note that the x-axis in all experiments is in radians per second; to convert to Hertz (Hz), multiply by 0.1592.

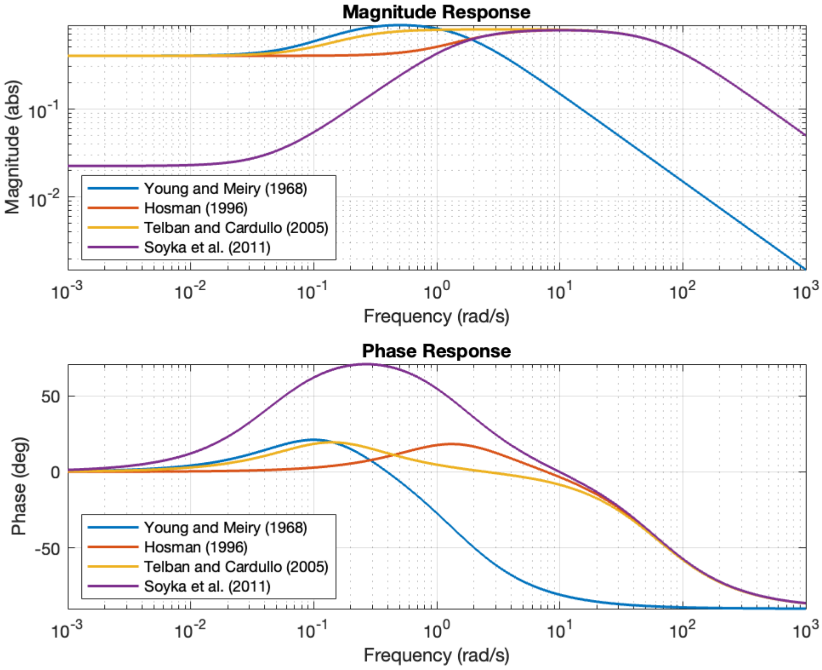

Figure 7.14: Bode plot illustrating the otolith transfer function using parameters derived from various studies, with acceleration as the input. Functions are based on empirical studies measuring human perception for horizontal accelerations.

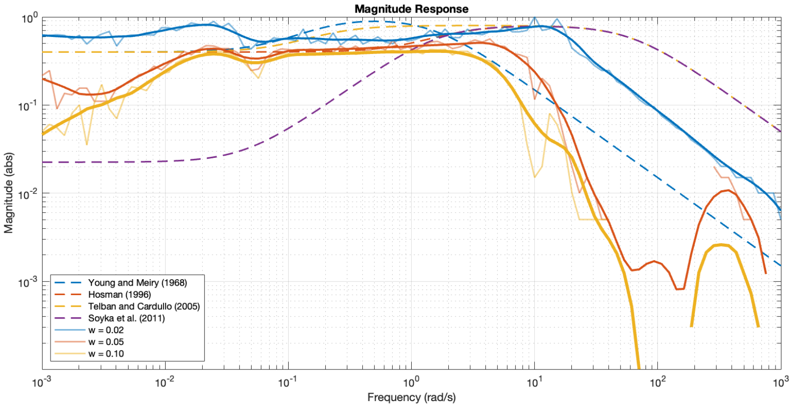

Figure 7.15: Experiment 5: Normalized gain vs frequency for 0.4G sinusoid, compared with empirical results from [87][39][91][97]

7.6. Result discussion

The results of our experiments revealed several limitations and challenges that need to be addressed. One significant constraint is the limited computational resources available, which restrict the distribution of afferents and the simulated time length to 10 seconds. Expanding computational capacity could allow for more detailed simulations and potentially more accurate results. We can then increase the parameter search range and the resolution between parameters. Also, simply more time spend with using the model will provide insights into what parameters optimize neural realism. If more relevant neural data becomes available it should be straightforward to make changes to the model due to its modular structure.

Attempts to obtain actual neural data, particularly from the Cullen lab, have unfortunately been unsuccessful. Both Jamali and Schneider have shifted their research focus and were unable to provide the data underlying their earlier studies. Actual neural data in combination with the stimuli applied could be a strong validator for the model.

The model also struggles with the low firing rate of regular neurons, leading to a higher likelihood of no spikes being recorded within a given time window w. This reduction in available data hampers the model's ability to make accurate predictions, particularly at low frequencies. To address this issue, one proposed solution is to use a moving average approach instead of a sliding window. In a sliding window approach, the model looks at spikes within a fixed window of time that moves step-by-step. If no spikes are recorded within any given window, the model has no data to work with. In contrast, a moving average approach would smooth out the data over time, combining information from overlapping windows. This would help retain more information about the neuron's activity, reducing the chance of "vanishing" distributions, situations where the model has no data to work with, while still preserving enough temporal resolution to make accurate predictions.

The RMS error between the model's acceleration estimates and the actual stimuli is often high (e.g., greater than 0.2G). This problem likely comes from differences between the expected firing rate, predicted by the LNL model, and the results from the spike encoding model. The spike encoding model introduces errors in the firing rate, which then spread through the rest of the model, lowering overall accuracy. Since the model depends on accurate firing rate estimates, resolving these issues in the spike encoding model should be a priority for future research.

We identified potential benefits of incorporating a resampling approach, similar to those used in particle filters. By maintaining a high exploratory weight, the model could remain robust to new acceleration inputs. However, due to the saturation of sensory data from neurons, the model may still struggle to accurately infer high accelerations.

In summary, these discussions highlight both the strengths and weaknesses of the current model. By addressing the identified limitations and exploring the proposed modifications, the model can be further optimized for more accurate and reliable predictions.

8

Conclusion

This thesis introduces a new approach to modeling vertical motion sickness by closely replicating the neural dynamics and statistical behavior of the otolith pathway. By adding elements like noise, nonlinearities, and realistic sensory data to the model, we have likely improved the realism and accuracy of motion sickness predictions. The results suggest that the Leaky-Integrate-and-Fire model is particularly effective at capturing the complex dynamics of otolith afferents, including their timing characteristics. The model functions as a vertical motion perception model, as demonstrated by its ability to track acceleration and its sensitivity to frequency, which matches findings from human perceptual experiments. Additionally, the model's use of the average KL Divergence as a proxy for Motion Sickness Incidence (MSI) shows dependencies on frequency and amplitude that align well with current understanding of motion sickness.

However, there are still areas for improvement. The relatively high RMS error in acceleration estimations suggests that the spike encoding model needs further refinement. Also, the biological basis for using Bayesian inference in the otoliths is not yet fully established. While this framework is a useful tool for studying afferents under the assumption of optimal sensory processing, it's not proven that this is the actual process in otolith signal processing. Expanding the model to three dimensions and incorporating predictive coding could make it more realistic and applicable.

In conclusion, this thesis lays the groundwork for a more biologically plausible model of vertical motion sickness, with potential applications in various fields, including virtual reality, autonomous vehicles, and spaceflight. Future research should focus on refining the model's accuracy, expanding its applicability to other types of motion sickness, and exploring its potential integration into broader motion perception or motion sickness frameworks. By continuing to build on this model, we can move closer to a comprehensive understanding of motion sickness and the development of effective interventions.

9

Discussion

9.1. Introduction

This chapter reviews the study's findings, considering their broader implications, limitations, and possible future directions. While the model provides valuable insights into how the vestibular system processes motion, it's important to understand these results within the context of the model's limitations and underlying assumptions.

9.2. Limitations

While Bayesian inference is a powerful tool for modeling sensory processing, the assumption that the brain operates according to these principles, particularly in the context of otolith afferents, is primarily supported by theoretical frameworks and lacks direct empirical evidence. It's important to recognize that Bayesian models, while insightful, are approximations of brain function rather than definitive representations. Future research should aim to gather empirical data that either supports or refines these assumptions. This could include studies using targeted stimulation [94] or antagonist that specifically target the irregular afferents[76] to measure otolith activity, cerebellum activity, human motion perception, and motion sickness incidence. Using the framework provided in this thesis and altering otolith signaling could provide new insights.

Although the current model has provided interesting insights, it is essential to acknowledge its limitations. One significant limitation is that the model only simulates one-dimensional motion. This simplification restricts the model's applicability to real-world scenarios where forces and accelerations act in three dimensions. This limitation simplifies the implementation, but in the future should be extended to 3 dimensions to be able to simulate more motion paradigms.

Another limitation is the absence of a predictive coding mechanism. The current model updates the prior probability statically, based solely on new sensory information, without incorporating the brain's ability to make predictions about future states. This static approach may limit the model's ability to accurately reflect the dynamic, predictive nature of sensory processing in the vestibular system, where expectations about future states influence current perceptions. Incorporating predictive coding could potentially enhance the model's realism and its ability to simulate real-world vestibular processing.

The model also assumes a uniform static firing rate of 79 spikes per second for all afferents, based on averages from the superior nerve. This assumption, while simplifying the model, overlooks the natural variability in firing rates across different neurons and conditions, which could lead to less accurate simulations of real neural behavior. Implementing individual variability in firing rates, perhaps drawn from empirical distributions, would likely result in a more representative model of actual neural activity.

Additionally, while there is limited data on the variance of otolith afferent firing rates during stimulation, more extensive variability data is available for the semicircular canals [26], and some trial-to-trial variability data exists for otoliths [85]. However, well-researched variability in firing rates during stimulation specific to otoliths should be a focus of future publications, as this data is critical for refining model accuracy.

Te model incorporates known motion frequency data, a decision supported by findings from Curthoys et al. [19], which suggest that irregular neurons encode frequencies in line with Volley theory. Assuming that the neural pathway can decode this information, the model applies frequency assumptions to the internal otolith model, which comprises the otolith transfer functions. While this approach underpins the model's ability to predict motion frequency, it may require further validation against experimental data.

Furthermore, the model treats afferents as belonging to one of two types, regular or irregular, without accounting for the spectrum of firing regularity and the complex interactions between afferents and hair cells. This simplification ignores the nuanced differences between individual afferents, potentially affecting the accuracy of the neural response predictions. Future models should incorporate a continuum of regularity and other biophysical differences, such as surface area and synaptic connections, to improve the biological realism of the simulations.

Finally, the model assumes a one-to-one connection between hair cells and afferents, which is not accurate for many regular and intermediate firing afferents. In reality, multiple afferents synapse onto a single hair cell and vice versa. This simplification could skew the simulation of neural responses, particularly under conditions where the complexity of synaptic relationships plays a critical role. Incorporating more accurate synaptic relationships will enhance the model's fidelity and allow for more precise predictions of neural behavior under various conditions.

9.3. Implications and Future Research Directions

Building on the identified limitations, several future research directions emerge. The most immediate direction involves expanding the model to simulate the vestibular system in three dimensions. By incorporating the complex anatomy and function of the otolith organs, a 3D model would more accurately replicate how the vestibular system processes real-world forces. This would enable the prediction of neural responses to various types of motion stimuli, including those encountered in everyday activities and experimental settings. The modular architecture of the current model is well-suited for such an extension, and initial steps toward implementing this 3D capability have already been undertaken. This foundation will facilitate the seamless integration of additional dimensions, leading to a more comprehensive and realistic simulation of vestibular function.

Another important future direction is the incorporation of predictive coding mechanisms within the model. Predictive coding is a fundamental aspect of sensory processing, and its inclusion would allow the model to simulate the brain's anticipatory processing of motion. This could lead to more accurate predictions of neural responses, particularly in dynamic environments where motion is continuous and predictable.

Currently, the model uses Poisson and Gaussian maximum likelihood estimation steps; however, as discussed with Paulin [78], an Exwald distribution should fit the otolith afferents better. This should be a straightforward implementation, since the code for the probability density function is already included in the model.

In addition, integrating additional empirical spiking data from primate studies and motion sickness data from humans would provide valuable validation and refinement for the model. Empirical data are essential for calibrating the model and testing its predictions against real-world observations, thus enhancing its reliability and applicability.

Given that the current model incorporates synaptic transmission and neurotransmitter characteristics, it presents a strong foundation for further expansion to simulate conditions such as vertical otolith stimulation and hypergravity. Incorporating these elements would significantly improve the applicability of the model in simulating diverse and extreme physical conditions. Such extensions would allow the model to test the robustness of vestibular system's responses and adaptations to these environments, offering valuable insights into its functional plasticity and resilience. It would provide an alternative to the existing distributed MSOM models for hypergravity [57].

Furthermore, integrating non-quantal transmission mechanisms could refine the model's predictions of neural behavior, particularly in the case of irregular neurons where such forms of synaptic transmission are particularly influential. By including these mechanisms, the model would gain a more nuanced understanding of how synaptic variability contributes to overall vestibular processing, potentially leading to more accurate and comprehensive predictions of neural dynamics under various physiological conditions. The mechanism for this is already developed by Steinhardt et al. [89].

9.4. Broader Impact and Clinical Relevance

The findings of this study have broader implications beyond the immediate scope of vestibular modeling. Clinically, the insights gained from this model could inform the development of vestibular prosthetics and treatments for motion sickness. A more accurate understanding of vestibular processing, as provided by an expanded and refined model, could lead to better-designed prosthetic devices or novel therapeutic approaches for conditions such as vestibular dysfunction or motion sickness.

In the field of robotics, the principles discovered through modeling vestibular afferents could inspire the design of artificial systems that need to interpret and respond to complex motion in a manner similar to biological systems. Such applications could improve the robustness and adaptability of robots in dynamic environments, making them more effective in tasks that require balance and spatial orientation.

9.5. Conclusion

This discussion has highlighted the significance of the study's findings while acknowledging the limitations of the current model. The two main areas of improvement are the refinement of the model through more analyses and stepwise improvements and the gathering of actual neural data to validate the model's performance. By addressing the limitations and following the suggested future research directions, it will be possible to build on this work, leading to a more comprehensive and accurate understanding of vestibular processing. Such advancements will have important implications for both clinical applications and broader research fields, particularly in the development of motion sickness mitigating algorithms and prosthetic systems.

References

[1] Dora E Angelaki and J David Dickman. “Spatiotemporal processing of linear acceleration: primary afferent and central vestibular neuron responses”. In: Journal of Neurophysiology 84.4 (2000), pp. 2113–2132. DOI: `10.1152/jn.2000.84.4.2113`.

[2] Dora E Angelaki and J David Dickman. “Vestibular mechanisms of three-dimensional motion perception”. In: Annual Review of Neuroscience 27 (2004), pp. 793–819.

[3] Hassan Anwar et al. “Stochastic calcium mechanisms cause dendritic calcium spike variability”. In: Journal of Neuroscience 33.40 (Oct. 2013), pp. 15848–15867. DOI: `10.1523/JNEUROSCI.1722-13.2013`. URL: `https://doi.org/10.1523/JNEUROSCI.1722-13.2013`.

[4] Curtis C Bell and Leonard Maler. Sensory Processing in Aquatic Environments. Springer, 2005.

[5] A. J. Benson, M. B. Spencer, and J. R. Stott. “Thresholds for the detection of the direction of whole-body, linear movement in the horizontal plane”. In: Aviation, Space, and Environmental Medicine 57.11 (1986), pp. 1088–1096.

[6] B. Bergström. “Morphology of the vestibular nerve. II. The number of myelinated vestibular nerve fibers in man at various ages”. In: Acta Oto-Laryngologica 76 (1973), pp. 173–179. DOI: `10.3109/00016487309121496`.

[7] J. E. Bos and W. Bles. “Modelling motion sickness and subjective vertical mismatch detailed for vertical motions”. In: Brain Research Bulletin 47.5 (Nov. 1998), pp. 537–542. ISSN: 03619230. DOI: `10.1016/S0361-9230(98)00088-4`.

[8] Robert C. Cannon, Clare O’Donnell, and Matthew F. Nolan. “Stochastic ion channel gating in dendritic neurons: morphology dependence and probabilistic synaptic activation of dendritic spikes”. In: PLOS Computational Biology 6.8 (Aug. 2010), e1000886. DOI: `10.1371/journal.pcbi.1000886`. eprint: 20711353. URL: `https://doi.org/10.1371/journal.pcbi.1000886`.

[9] Catherine E Carr and Leonard Maler. “Electrosensory systems in weakly electric fish: modifiability and learning”. In: Brain, Behavior and Evolution 28.1-3 (1986), pp. 51–71.

[10] J Carriot et al. “Statistics of the vestibular input experienced during natural self-motion: implications for neural processing”. In: Journal of Neuroscience 34 (2014), pp. 8347–8357. DOI: `10.1523/JNEUROSCI.0692-14.2014`.

[11] Jérome Carriot et al. “Statistics of the Vestibular Input Experienced during Natural Self-Motion: Implications for Neural Processing”. In: Journal of Neuroscience 34.24 (June 2014), pp. 8347–8357. DOI: `10.1523/JNEUROSCI.0692-14.2014`.

[12] EJ Chichilnisky. “A simple white noise analysis of neuronal light responses”. In: Network: Computation in Neural Systems 12.2 (2001), pp. 199–213. DOI: `10.1080/net.12.2.199.213`.

[13] B. W. Connors, M. A. Paradiso, and M. F. Bear. Neuroscience: Exploring the Brain. 3rd. Baltimore, MD: Lippincott, Williams & Wilkins, 2006. ISBN: 978-0781760034.

[14] M.J. Correia and J.P. Landolt. “A point process analysis of the spontaneous activity of anterior semicircular canal units in the anesthetized pigeon”. In: Biological Cybernetics 27 (1977). PubMed, pp. 123–130.

[15] Kathleen E. Cullen. “Vestibular processing during natural self-motion: implications for perception and action”. In: Nature Reviews Neuroscience 20.6 (June 2019), pp. 346–363. ISSN: 14710048. DOI: `10.1038/S41583-019-0153-1`.

[16] Kathleen E. Cullen et al. “Internal models of self-motion: computations that suppress vestibular reafference in early vestibular processing”. In: Experimental brain research 210.3-4 (May 2011), pp. 377–388. ISSN: 1432-1106. DOI: `10.1007/S00221-011-2555-9`. URL: `https://pubmed.ncbi.nlm.nih.gov/21286693/`.

[17] I. S. Curthoys, Ann M. Burgess, and Samanthi C. Goonetilleke. “Phase-locking of irregular guinea pig primary vestibular afferents to high frequency (>250 Hz) sound and vibration”. In: Hearing research 373 (Mar. 2019), pp. 59–70. ISSN: 1878-5891. DOI: `10.1016/J.HEARES.2018.12.009`. URL: `https://pubmed.ncbi.nlm.nih.gov/30599427/`.

[18] I. S. Curthoys and J. W. Grant. “How does high-frequency sound or vibration activate vestibular receptors?” In: Experimental Brain Research 233.3 (2015), pp. 691–699. DOI: `10.1007/s00221-014-4192-6`. URL: `https://doi.org/10.1007/s00221-014-4192-6`.

[19] Ian S. Curthoys et al. “A review of mechanical and synaptic processes in otolith transduction of sound and vibration for clinical VEMP testing”. In: Journal of Neurophysiology (July 2019). DOI: `10.1152/jn.00031.2019`. URL: `https://doi.org/10.1152/jn.00031.2019`.

[20] Ian S. Curthoys et al. Sustained and transient vestibular systems: A physiological basis for interpreting vestibular function. Mar. 2017. DOI: `10.3389/fneur.2017.00117`.

[21] Ruth A. Eatock. “Vertebrate Hair Cells: Modern and Historic Perspectives”. In: Vertebrate Hair Cells. Ed. by Ruth A. Eatock, Richard R. Fay, and Arthur N. Popper. Vol. 27. Springer Handbook of Auditory Research. New York, NY: Springer, 2006, pp. 1–16. DOI: `10.1007/0-387-31706-6_1`. URL: `https://doi.org/10.1007/0-387-31706-6_1`.

[22] Ruth A. Eatock, Jing Xue, and Radha Kalluri. “Ion channels in mammalian vestibular afferents may set regularity of firing”. In: Journal of Experimental Biology 211.Pt 11 (June 2008), pp. 1764–1774. DOI: `10.1242/jeb.017350`.

[23] A. Aldo Faisal, Luc P.J. Selen, and Daniel M. Wolpert. “Noise in the nervous system”. In: Nature Reviews Neuroscience 2008 9:4 9.4 (Apr. 2008), pp. 292–303. ISSN: 1471-0048. DOI: `10.1038/nrn2258`. URL: `https://www.nature.com/articles/nrn2258`.

[24] C. Fernandez and J. M. Goldberg. “Physiology of peripheral neurons innervating otolith organs of the squirrel monkey. I. Response to static tilts and to long-duration centrifugal force”. In: Journal of neurophysiology 39.5 (1976), pp. 970–984. ISSN: 0022-3077. DOI: `10.1152/JN.1976.39.5.970`. URL: `https://pubmed.ncbi.nlm.nih.gov/824412/`.

[25] C. Fernandez and J. M. Goldberg. “Physiology of peripheral neurons innervating semicircular canals of the squirrel monkey. II. Response to sinusoidal stimulation and dynamics of peripheral vestibular system”. In: Journal of neurophysiology 34.4 (1971), pp. 661–675. ISSN: 0022-3077. DOI: `10.1152/JN.1971.34.4.661`. URL: `https://pubmed.ncbi.nlm.nih.gov/5000363/`.

[26] Cesar Fernandez and Jay M Goldberg. “Response dynamics of peripheral vestibular neurons to linear and angular accelerations”. In: Journal of Neurophysiology 35.5 (1972), pp. 798–816.

[27] Cesar Fernandez, Jay M. Goldberg, and Walter K. Abend. “Response to static tilts of peripheral neurons innervating otolith organs of the squirrel monkey”. In: Journal of Neurophysiology 35.6 (1972), pp. 978–987. DOI: `10.1152/jn.1972.35.6.978`.

[28] Karl Friston. “The history of the future of the Bayesian brain”. In: NeuroImage 62.2 (Aug. 2012), pp. 1230–1233. DOI: `10.1016/j.neuroimage.2011.10.004`.

[29] Stanley A Gelfand. Hearing: An Introduction to Psychological and Physiological Acoustics. CRC Press, 2004.

[30] Elisabeth Glowatzki and Paul A. Fuchs. “Transmitter release at the hair cell ribbon synapse”. In: Nature Neuroscience 5.2 (2002), pp. 147–154. DOI: `10.1038/nn796`. URL: `https://doi.org/10.1038/nn796`.

[31] J.M. Goldberg. The Vestibular System: A Sixth Sense. OUP USA, 2012. ISBN: 9780195167085. URL: `https://books.google.se/books?id=dMixjJPwKdQC`.

[32] Jay M Goldberg. “Afferent diversity and the organization of central vestibular pathways”. In: Experimental Brain Research 130.3 (2000), pp. 277–297.

[33] Joshua H. Goldwyn and Eric Shea-Brown. “The what and where of adding channel noise to the Hodgkin-Huxley equations”. In: PLOS Computational Biology 7.11 (Nov. 2011), e1002247. DOI: `10.1371/journal.pcbi.1002247`. eprint: 22125479. URL: `https://doi.org/10.1371/journal.pcbi.1002247`.

[34] L. Grant, E. Yi, and E. Glowatzki. "Two modes of release shape the postsynaptic response at the inner hair cell ribbon synapse". In: Journal of Neuroscience 30 (2010), pp. 4210–4220.

[35] Stephen M. Highstein et al. "Evidence that protons act as neurotransmitters at vestibular hair cell-calyx afferent synapses". In: Proceedings of the National Academy of Sciences 111.15 (2014), pp. 5421–5426. DOI: `10.1073/pnas.1322994111`. URL: `https://www.pnas.org/content/111/15/5421`.

[36] Ariel E Hight and Radha Kalluri. "A biophysical model examining the role of low-voltage-activated potassium currents in shaping the responses of vestibular ganglion neurons". In: Journal of Neurophysiology 116.2 (2016), pp. 503–521. DOI: `10.1152/jn.00107.2016`.

[37] Gay R. Holstein, Giorgio P. Martinelli, and Bernard Cohen. "Vestibular nuclei neurons: functional classification and their role in generating eye movements". In: Annals of the New York Academy of Sciences 1233.1 (2011), pp. 22–32.

[38] J. R. Holt and A. Lysakowski. "Postsynaptic mechanisms of vestibular signal processing in the central nervous system". In: Journal of Vestibular Research 16.4-5 (2006), pp. 195–202.

[39] R.J. Hosman. "Pilot's perception and control of aircraft motions". Ph.D. Thesis. Delft University of Technology, 1996.

[40] A J Hudspeth. "How the ear's works work". In: Nature 341.6241 (1989), pp. 397–404.

[41] Tugrul Irmak et al. "Motion Sickness, Motivation, Workload and Task Performance in Automated Vehicles". In: Comfort Congress 2021. Conference Paper presented at the Comfort Congress. Sept. 2021. URL: `https://publications.ergonomics.org.uk/uploads/01_Tugrul-Irmak.pdf`.

[42] Akira Ishiyama et al. "Hair cell pathology in a case of Waardenburg's syndrome type I". In: International Journal of Audiology 42.1 (2003), pp. 43–48.

[43] Marta M. Iversen and Richard D. Rabbitt. "Wave Mechanics of the Vestibular Semicircular Canals". In: Biophysical Journal 113.5 (Sept. 2017), pp. 1133–1149. ISSN: 0006-3495. DOI: `10.1016/J.BPJ.2017.08.001`.

[44] E.M. Izhikevich. "Simple model of spiking neurons". In: IEEE Transactions on Neural Networks 14.6 (2003), pp. 1569–1572. DOI: `10.1109/TNN.2003.820440`.

[45] M Jamali et al. "Strong correlations between sensitivity and variability give rise to constant discrimination thresholds across the otolith afferent population". In: Journal of Neuroscience 33 (2013), pp. 11302–11313. DOI: `10.1523/JNEUROSCI.0459-13.2013`.

[46] Mohsen Jamali, Maurice J. Chacron, and Kathleen E. Cullen. "Self-motion evokes precise spike timing in the primate vestibular system". In: Nature Communications 7 (Oct. 2016). Open access, p. 13229. DOI: `10.1038/ncomms13229`. URL: `https://www.nature.com/articles/ncomms13229`.

[47] Mohsen Jamali, Soroush G Sadeghi, and Kathleen E Cullen. "Response of Vestibular Nerve Afferents Innervating Utricle and Saccule During Passive and Active Translations". In: J Neurophysiol 101 (2009), pp. 141–149. DOI: `10.1152/jn.91066.2008`. URL: `www.jn.org`.

[48] Mohsen Jamali et al. "Coding strategies in the otolith system differ for translational head motion vs. static orientation relative to gravity". In: eLife 8 (June 2019). ISSN: 2050084X. DOI: `10.7554/ELIFE.45573`.

[49] James O'Hanlon and Michael E McCauley. "Motion Sickness Incidence as a Function of Vertical Sinusoidal Motion". In: Aerospace Medicine 45.4 (1974), pp. 366–9. URL: `https://www.researchgate.net/publication/18346380_Motion_Sickness_Incidence_as_a_Function_of_Vertical_Sinusoidal_Motion`.

[50] G. M. Jones and L. R. Young. "Subjective detection of vertical acceleration: a velocity-dependent response?" In: Acta Otolaryngologica 85.1-2 (1978), pp. 45–53. DOI: `10.3109/00016487809121422`.

[51] Radha Kalluri, Jingbing Xue, and Ruth Anne Eatock. "Ion Channels Set Spike Timing Regularity of Mammalian Vestibular Afferent Neurons". In: Journal of Neurophysiology 104.4 (Oct. 2010). Published online 2010 Jul 21, pp. 2034–2051. DOI: `10.1152/jn.00396.2010`.

[52] Masashi Kawasaki. “Sensory information processing in electric fish”. In: Journal of Experimental Biology 208.7 (2005), pp. 1387–1402.

[53] Sarah Khan and Richard Chang. “Anatomy of the vestibular system: A review”. In: NeuroRehabilitation 32 (2013), pp. 437–443. DOI: `10.3233/NRE-130866`.

[54] G. Kim and K.S. Kim. “Hypergravity-induced malfunction was moderated by the regulation of NMDA receptors in the vestibular nucleus”. In: Scientific Reports 11 (2021), p. 17420. DOI: `10.1038/s41598-021-97050-8`. URL: `https://doi.org/10.1038/s41598-021-97050-8`.

[55] Megan J. Kobel, Andrew R. Wagner, and Daniel M. Merfeld. “Impact of gravity on the perception of linear motion”. In: Journal of Neurophysiology 126.3 (2021), pp. 875–887. DOI: `10.1152/jn.00274.2021`.

[56] Varun Kotian et al. “The role of vision in sensory integration models for predicting motion perception and sickness”. In: Experimental Brain Research 242.3 (Mar. 2024). Epub 2024 Jan 23, pp. 685–725. DOI: `10.1007/s00221-023-06747-x`.

[57] Victoria G Kravets et al. A Rao-Blackwellized Particle Filter for Modeling Neurovestibular Adaptation to Altered Gravity. Tech. rep. 2022.

[58] Arthur D. Kuo. “An optimal state estimation model of sensory integration in human postural balance”. In: Journal of Neural Engineering 2.3 (Sept. 2005). Epub 2005 Aug 31, S235–S249. DOI: `10.1088/1741-2560/2/3/S07`. URL: `https://doi.org/10.1088/1741-2560/2/3/S07`.

[59] Jean Laurens and Dora E. Angelaki. “A unified internal model theory to resolve the paradox of active versus passive self-motion sensation”. In: eLife 6 (Oct. 2017). ISSN: 2050084X. DOI: `10.7554/ELIFE.28074`.

[60] Jean Laurens et al. “Transformation of spatiotemporal dynamics in the macaque vestibular system from otolith afferents to cortex”. In: eLife 6 (2017). Published online 2017 Jan 11, e20787. DOI: `10.7554/eLife.20787`.

[61] Margaret S Livingstone and David H Hubel. “Segregation of form, color, movement, and depth: anatomy, physiology, and perception”. In: Science 240.4853 (1987), pp. 740–749.

[62] Paul R. MacNeilage et al. “Vestibular heading discrimination and sensitivity to linear acceleration in head and world coordinates”. In: Journal of Neuroscience 30.27 (2010), pp. 9084–9094. DOI: `10.1523/JNEUROSCI.1304-10.2010`.

[63] David Marr. Vision: A Computational Investigation into the Human Representation and Processing of Visual Information. Henry Holt and Co., Inc., 1982.

[64] Akira Matsubara et al. “Organization of AMPA receptor subunits at a glutamate synapse: A quantitative immunogold analysis of hair cell synapses in the rat organ of Corti”. In: Journal of Neuroscience 16.14 (1996), pp. 4457–4467.

[65] Saumil N. Merchant et al. “Temporal bone studies of the human peripheral vestibular system. Normative vestibular hair cell data”. In: Annals of Otology, Rhinology & Laryngology Supplement 181 (2000), pp. 3–13. DOI: `10.1177/00034894001090s502`.

[66] William H Merigan and John HR Maunsell. “Parallel pathways for vision in the cerebral cortex”. In: Annual Review of Neuroscience 16.1 (1993), pp. 369–402.

[67] Paul Miller and Jonathan Cannon. “Combined mechanisms of neural firing rate homeostasis”. In: Biological Cybernetics 113.1 (2019). Published online 2018 Jun 28, pp. 47–59. DOI: `10.1007/s00422-018-0768-8`.

[68] Amir R Naseri and Peter R Grant. “Human discrimination of translational accelerations”. In: Experimental Brain Research 218.3 (2012), pp. 455–464. DOI: `10.1007/s00221-012-3035-6`.

[69] Christopher J. Nash, David J. Cole, and Robert S. Bigler. “A review of human sensory dynamics for application to models of driver steering and speed control”. In: Biological Cybernetics 110 (2016), pp. 91–116. DOI: `10.1007/s00422-016-0714-0`. URL: `https://doi.org/10.1007/s00422-016-0714-0`.

[70] Alessandro Nesti et al. “Human sensitivity to vertical self-motion”. In: Experimental Brain Research 232.1 (2014), pp. 303–314. DOI: `10.1007/s00221-013-3741-8`.

[71] Michael C Newman and Charles M Oman. A MULTISENSORY OBSERVER MODEL FOR HUMAN SPATIAL ORIENTATION PERCEPTION. Tech. rep. 2009.

[72] Donata Oertel. “The role of timing in the brain stem auditory nuclei of vertebrates”. In: Annual Review of Physiology 61.1 (1999), pp. 497–519.

[73] Charles M. Oman. “Sensory Motor Conflict Theory for Motion Sickness: Oman letter to Reason”. In: (1978).

[74] T.S. Otis, M.P. Kavanaugh, and C.E. Jahr. “Postsynaptic glutamate transport at the climbing fiber–Purkinje cell synapse”. In: Science 277.5331 (1996), pp. 1515–1518.

[75] Andrew J. Oxenham. “Revisiting place and temporal theories of pitch”. In: Acoustical Science and Technology 34.6 (2013). Author manuscript; available in PMC 2014 Oct 31, pp. 388–396. DOI: `10.1250/ast.34.388`.

[76] Christopher J. Pastras et al. “Evidence That Ultrafast Nonquantal Transmission Underlies Synchronized Vestibular Action Potential Generation”. In: Journal of Neuroscience 43.43 (2023), pp. 7149–7157. DOI: `10.1523/JNEUROSCI.1417-23.2023`. URL: `https://doi.org/10.1523/JNEUROSCI.1417-23.2023`.

[77] M. Paulin. “A Kalman Filter Theory of the Cerebellum”. In: Dynamic Interactions in Neural Networks: Models and Data. Ed. by M.A. Arbib and Si. Amari. Vol. 1. Research Notes in Neural Computing. Springer, New York, NY, 1989, pp. 238–256. ISBN: 978-0-387-96893-3. DOI: `10.1007/978-1-4612-4536-0_15`. URL: `https://doi.org/10.1007/978-1-4612-4536-0_15`.

[78] Michael G Paulin and Larry F Hoffman. “Models of vestibular semicircular canal afferent neuron firing activity”. In: J Neurophysiol 122 (2019), pp. 2548–2567. DOI: `10.1152/jn.00087.2019.-Semicircular`. URL: `www.jn.org`.

[79] Michael G. Paulin and Andre van Schaik. “Bayesian Inference with Spiking Neurons”. In: Encyclopedia of Computational Neuroscience (June 2014), pp. 1–4. DOI: `10.48550/arxiv.1406.5115`. URL: `https://arxiv.org/abs/1406.5115v1`.

[80] Mike Paulin, Larry Hoffman, and Kiri Pullar. “A Bayesian Generative Model of Vestibular Afferent Neuron Spiking”. In: bioRxiv (Feb. 2020). University of Otago, University of California, Los Angeles, Universitätsklinikum Hamburg-Eppendorf (UKE). DOI: `10.1101/2020.02.03.933150`. URL: `https://www.biorxiv.org/content/10.1101/2020.02.03.933150v1`.

[81] Rajesh PN Rao. “Bayesian computation in recurrent neural circuits”. In: Neural Computation 16.1 (2004), pp. 1–38. DOI: `10.1162/08997660460733976`. URL: `https://doi.org/10.1162/08997660460733976`.

[82] Jason S. Rothman and Paul B. Manis. “The roles potassium currents play in regulating the electrical activity of ventral cochlear nucleus neurons”. In: Journal of Neurophysiology 89.6 (2003), pp. 3097–3113. DOI: `10.1152/jn.00127.2002`. URL: `https://journals.physiology.org/doi/full/10.1152/jn.00127.2002`.

[83] S. G. Sadeghi et al. “Glutamatergic signaling at the vestibular hair cell calyx synapse”. In: Journal of Neuroscience 34.45 (2014), pp. 14536–14550.

[84] SG Sadeghi, LB Minor, and KE Cullen. “Response of vestibular-nerve afferents to active and passive rotations under normal conditions and after unilateral labyrinthectomy”. In: Journal of Neurophysiology 97 (2007), pp. 1503–1514. DOI: `10.1152/jn.00829.2006`.

[85] Adam D. Schneider et al. “The Increased Sensitivity of Irregular Peripheral Canal and Otolith Vestibular Afferents Optimizes their Encoding of Natural Stimuli”. In: Journal of Neuroscience 35.14 (Apr. 2015), pp. 5522–5536. DOI: `10.1523/JNEUROSCI.3841-14.2015`.

[86] Jocelyn E. Songer and Ruth Anne Eatock. “Tuning and timing in mammalian type I hair cells and calyceal synapses”. In: Journal of Neuroscience 33.9 (2013), pp. 3706–3724.

[87] Florian Soyka et al. “Predicting direction detection thresholds for arbitrary translational acceleration profiles in the horizontal plane”. In: Experimental Brain Research 209.1 (2011). CC BY-NC, pp. 95–107. DOI: `10.1007/s00221-010-2523-9`. URL: `https://doi.org/10.1007/s00221-010-2523-9`.

[88] Nelson Spruston. “Pyramidal neurons: dendritic structure and synaptic integration”. In: Nature Reviews Neuroscience 9.3 (2008), pp. 206–221.

[89] Cynthia R. Steinhardt and Gene Y. Fridman. “Direct current effects on afferent and hair cell to elicit natural firing patterns”. In: iScience 24.3 (2021), p. 102205. ISSN: 2589-0042. DOI: `10.1016/j.isci.2021.102205`. URL: `https://www.sciencedirect.com/science/article/pii/S2589004221001735`.

[90] Terry T Takahashi and Masakazu Konishi. “The representation of auditory space in the owl’s inferior colliculus”. In: Journal of Neuroscience 4.3 (1984), pp. 849–865.

[91] Robert J Telban and Frank M Cardullo. “Motion Cueing Algorithm Development: Human-Centered Linear and Nonlinear Approaches”. In: (2005). URL: `http://www.sti.nasa.gov`.

[92] Alessandro Urciuoli et al. “The Evolution of the Vestibular Apparatus in Apes and Humans”. In: eLife 9 (2020), e51261. DOI: `10.7554/eLife.51261`. URL: `https://doi.org/10.7554/eLife.51261`.

[93] LE Walther et al. “Neuronal network-based mathematical modeling of perceived verticality in acute unilateral vestibular lesions: from nerve to thalamus and cortex”. In: Journal of Neurology 265.5 (2018), pp. 1074–1085. DOI: `10.1007/s00415-018-8909-5`.

[94] Séamas Weech, Travis Wall, and Michael Barnett-Cowan. “Reduction of cybersickness during and immediately following noisy galvanic vestibular stimulation”. In: Experimental Brain Research 238.2 (Feb. 2020), pp. 427–437. ISSN: 14321106. DOI: `10.1007/S00221-019-05718-5/FIGURES/4`. URL: `https://link.springer.com/article/10.1007/s00221-019-05718-5`.

[95] J. M. Wolfe et al., eds. Sensation & Perception. 6th. Oxford University Press, 2017.

[96] M. Yamashita, H. Ohmori, and J. Fukuda. “Non-quantal transmitter release at an excitatory synapse in the rat vestibular system”. In: Brain Research 507.2 (1990), pp. 315–322.

[97] Laurence R. Young and J. L. Meiry. “A revised dynamic otolith model”. In: Acta Otolaryngol 39.6 (1968), pp. 606–608.

[98] Wen-Hao Zhang et al. “Sampling-based Bayesian inference in recurrent circuits of stochastic spiking neurons”. In: Nature Communications 14.7074 (2023). DOI: `10.1038/s41467-023-70847-4`. URL: `https://www.nature.com/articles/s41467-023-70847-4`.